UNIVERSITÀ DI PISA

FACOLTÀ DI SCIENZE MATEMATICHE, FISICHE E NATURALI

CORSO DI LAUREA MAGISTRALE IN FISICA

TESI DI LAUREA MAGISTRALE

First measurement of vector boson polarization at LHC

CANDIDATO:

Marco Peruzzi

RELATORE:

Prof. Luigi Rolandi

ANNO ACCADEMICO 2010/2011

Introduction

The production of W and Z vector bosons in hadronic collisions probes the nature of both perturbative quantum chromodynamics (QCD) and electroweak interaction. While the momentum and rapidity distribution of W/Z are determined by the details of QCD production mechanism, the topological and kinematic properties of the final state - i.e. of the leptons observed as decay products - are largely sensitive to the electroweak process of vector boson production and decay.

Generally speaking, W and Z are source of missing transverse energy, one of the most important signatures in the search for new physics. It is therefore important to study their production and validate the MC models used for their detailed simulation.

The production of vector bosons at LHC displays new characteristics, due to the proton-proton nature of the collision, that were not present at the proton-antiproton colliders; peculiar asymmetries in charge and momentum for vector bosons and their decay leptons emerge, and a large left-handed polarization is expected in the transverse plane at high p_T. Precise measurements of these properties can be performed; the detailed information acquired on the vector bosons produced in SM processes can be used in searches for Beyond the Standard Model physics to increase the signal to background ratio.

In this thesis, the first measurement of vector boson polarization at a proton-proton collider is reported. Polarization information is extracted from angular distributions of decay leptons by means of a fit with templates obtained by a MC simulation. Results are obtained from data samples collected by the Compact Muon Solenoid (CMS) experiment at $\sqrt{s} = 7$ TeV, and compared to expectations from theoretical Standard Model calculations. They are found to be consistent with each other within the present sensitivity.

Chapter 1

Theory of vector boson polarization at hadron colliders

1.1 General remarks

Events characterized by the production of a vector boson in association with jets at LHC can be generated by a great variety of physics processes. Together with the dominating QCD W/Z (+ jets) production and the top quark production and semileptonic decay, they could be due to cascade decays in the framework of supersymmetric extensions of the Standard Model (or, more generally, to physics beyond the standard model), or Higgs decay into vector bosons.

W bosons produced with low p_T in hadronic collisions, and therefore moving generally along the beam axis, exhibit a left-handed polarization [1], because the W couples, in the dominant production diagram, only to the left handed component of valence quarks, and to the right handed one of sea anti-quarks.

At high p_T , the situation becomes more complex; there has been an intensive theoretical research in the last decades to accurately describe such W/Z+jets events at hadron colliders. At first, leading-order matrix elements have been computed; more recently, parton-shower tecniques have been used to add to the LO matrix element an accurate description of jet substructure, which is required for comparison with data from the experiments [2].

However, the LO nature of these calculations poses problems in terms of overall normalization of cross sections (with an uncertainty growing together with the number of jets involved in the process) and reliability of the predicted angular distributions.

It's therefore important to move to the next-to-leading order in perturbative QCD. It has been shown [2] that such a procedure provides results with smaller dependence on renormalization and factorization scales; in this way, the theoretical uncertainties are reduced to 10-15% level.

Until a few years ago, major difficulties were found in such one-loop calculations. New techniques have recently been used to compute NLO predictions of W + n-jets processes, with n up to 4 [3–5]; these calculations show that the shapes of the angular distributions of decay leptons are not very sensitive to the NLO corrections.

Basically speaking, a spin-1 boson has three different polarization states, corresponding to the values that the azimuthal quantum number m can take in the set $\{-1, 0, 1\}$. Let's choose the z axis as the quantization axis; each polarization gives a contribution to the polar (θ^*) angular distribution of the decay lepton, as follows:

$$\frac{d\sigma_{l^+}}{d\cos\theta^* d\phi^*} = f_L \frac{(1-\cos\theta^*)^2}{4} + f_0 \frac{\sin^2\theta^*}{2} + f_R \frac{(1+\cos\theta^*)^2}{4} \tag{1.1}$$

where the three coefficients f_L, f_R and $f_0 = 1 - f_L - f_R$ determine the amount of left, right and longitudinal polarization respectively. The aim of the analysis is to extract these polarization fractions from the measurement of the angular distributions of decay leptons.

The polarization fractions, moreover, are dependent on the PDF set chosen (Table 1.1). With a large data sample, actually, this measurement could be used to constrain the PDF for partons relevant to this process.

Table 1.1: Angular parameters for positively and negatively charged W respectively, for different PDF sets. Cut on W $p_T > 50$ GeV/c . [6]

MC	$(f_L - f_R)^-$	f_0^-	$(f_L - f_R)^+$	f_0^+
MG LO (CTEQ6L1)	0.242	0.215	0.322	0.225
MSTW2008 NNLO	0.233	0.214	0.318	0.224
NNPDF 2.0	0.247	0.214	0.324	0.223

It was first observed in [4] that both W^+ and W^- bosons produced with high p_T at the LHC have a dominant left-handed polarization along their direction of flight.

As a consequence, when the W decays into leptons, an important asymmetry is observed between the p_T spectra of these leptons for different charges of the W.

In a simple example: when a left-handed W^+ is produced in the transverse plane, it can be seen from angular momentum conservation and from the formula above that its decay left-handed neutrino will be preferentially emitted along the flight direction, whereas the charged anti-lepton will go in the opposite direction. For the left-handed W^- , on the other hand, the charged lepton will fly preferentially in the same direction of the W, and the right-handed anti-neutrino will choose the other direction.

Consequently, events with a W^+ will exhibit on average a charged lepton with smaller p_T ,

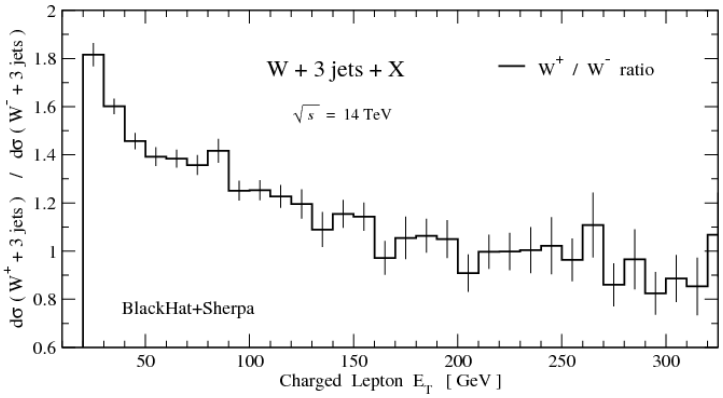

Figure 1.1: Ratio of charged lepton p_T distributions for W^+ and $W^- + 3$ jets production events at the LHC, at NLO [2]. The positive charge contribution decreases at high p_T.

and a larger missing E_T , with respect to events with a W^- (Fig. 1.1).

The coupling of the W to leptons, actually, involves the chirality left-handed projector $\frac{1-\gamma^5}{2}$; it's therefore reasonable that strong polarization effects can be observed in such interactions. In case of the Z boson, on the other hand, a coupling to right-handed leptons is also present, so one should expect a more diluted behaviour.

The angular distributions of decay leptons can be parametrized according to the most general form of the differential cross section for the W/Z + jets production in a pp collision, which will be introduced in section 1.3; before that, however, it's necessary to fix a reference frame with respect to which the measurements have to be performed.

1.2 Reference frames

The most natural choice for the z axis of the reference frame is the flight direction of the vector boson in the laboratory frame. However, different choices can be done for the orientation of both the z and x axes; two interesting ones - for different reasons - are the helicity and the Collins-Soper frames.

1.2.1 Helicity frame

In the helicity frame, the z axis is chosen to be along the flight direction of the vector boson in the laboratory frame. The x axis is chosen (in the plane orthogonal to the z axis) so that, once carried out the boost along the z axis in the W/Z rest frame, the incoming protons lie on the xz plane, and directed towards the "closest" proton (in the sense of angular distance).

In other words, let's define the rapidity to be positive along the flight direction of p_1 in a p_1p_2 collision: if the vector boson is produced with positive rapidity in the lab frame, the closest proton will be p_2; otherwise it will be p_1 (Fig. 1.2).

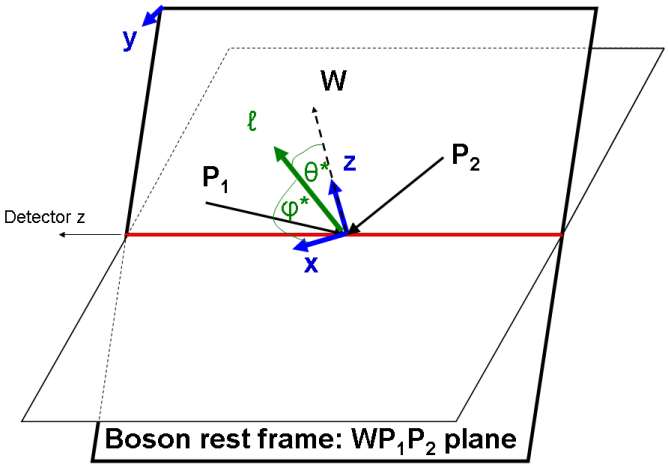

Figure 1.2: Axes choice in the helicity frame. [6]

A very important feature of this frame is that the angular distributions of decay leptons from bosons 100% polarized along their direction of flight do not depend on ϕ^*, because the z axis of the frame and the quantization axis coincide (Eq. 1.1).

Also important is the fact that, apart from the choice of the x axis (i.e. of the $\phi^* = 0$ topology), there will be no dependence on other kinematic variables of the event - for example, the W/Z p_T . Therefore, the $\cos\theta^*$ distribution - for a fixed 100% polarization case - will not depend on (p_T, η) of the vector boson.

In the practice, however, the situation is much more complicated: first of all, limited lepton acceptance introduces a dependence of the angular shapes both on ϕ^* and on the (p_T, η) of the vector boson; secondly, it can be impossible to fully reconstruct the lepton momentum in the helicity frame.

When a W boson is present, for example, it's impossible to determine the boost from the laboratory system to the W center-of-mass system, because one cannot measure the momentum of the decay neutrino along the beam direction; as a consequence, the flight direction of the lepton in the W rest frame is unknown, and other techniques have to be used to recover the polarization information. These considerations motivate the study of reference systems alternative to the helicity frame.

1.2.2 Collins-Soper frame

A very popular frame choice has been proposed by Collins and Soper in 1977 [7], and brings a major advantage in terms of experimental feasibility of the measurement with W bosons.

In this system, the choice of axes is more complicated than in the helicity frame: at first,

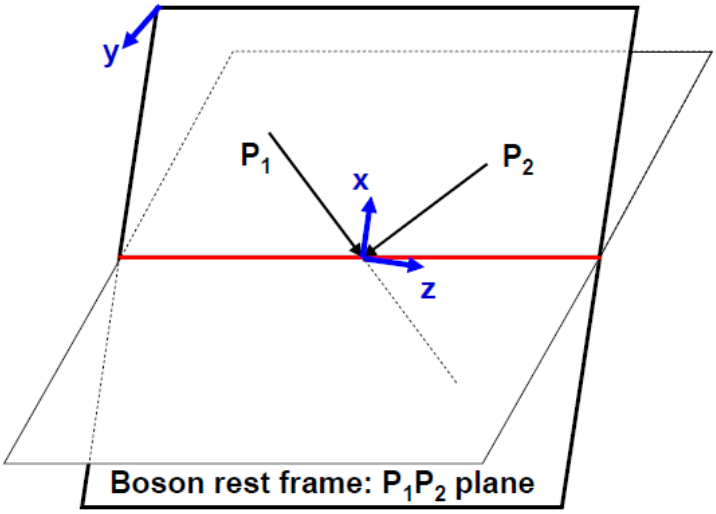

Figure 1.3: Axes choice in the Collins-Soper frame. [6]

one boosts himself in the W/Z rest frame; then, the z axis is chosen in that frame so that it bisects the angle between the momentum p_1 of the first incoming proton, and the opposite $-p_2$ of the incoming second proton (Fig. 1.3).

The protons momenta take the following form in such frame:

$$\vec{p}_1^{cs} = E_1^{cs}\left(-\frac{r}{\sqrt{1+r^2}}, 0, +\frac{1}{\sqrt{1+r^2}}\right)$$

$$\vec{p}_2^{cs} = E_2^{cs}\left(-\frac{r}{\sqrt{1+r^2}}, 0, -\frac{1}{\sqrt{1+r^2}}\right)$$

where $r = p_T^W/M_W$, $E_1^{cs} = \frac{\sqrt{s}}{2}\sqrt{1+r^2}e^{-y}$, $E_2^{cs} = \frac{\sqrt{s}}{2}\sqrt{1+r^2}e^{+y}$, and p_T^W, M_W and y are the transverse momentum, the mass and the rapidity of the W in the lab frame.

It's also possible to derive [8] the following equations for lepton momentum in the CS frame, as a function of its measured components in the laboratory frame:

$$p_{lx}^{cs} = \frac{1}{2}\frac{M_W}{\sqrt{{M_W}^2 + {p_T^W}^2}}(2p_{lx} - p_T^W)$$

$$p_{ly}^{cs} = p_{ly} \tag{1.2}$$

$$p_{lz}^{cs} = \pm\frac{M_W}{2}\sqrt{1 - \frac{p_{lx}^{cs\,2} + p_{ly}^{cs\,2}}{M_W^2/4}}$$

It's crucial to note, in the above relations, that the impossibility to measure the neutrino p_z affects only the sign of the z component of lepton's momentum in the CS frame: both its

absolute value $|p_{lz}^{cs}|$ and the transverse momentum $\vec{p}_{lT}^{cs}$ can be calculated.

Therefore, only the sign of $\cos\theta^*$ is left undetermined when using the Collins-Soper frame. This allows the measurement of the contributions to the cross section that are symmetric under a $\theta^* \leftrightarrow \pi - \theta^*$ transformation.

The main disadvantage of this frame is that the angular distributions corresponding to a boson 100% polarized along its direction of flight have a complicated dependence not only on θ^* and ϕ^*, but also on its p_T and η. Therefore, the f_L, f_R, f_0 parametrization is not natural in this system, and a more general parametrization of the cross section (in terms of the asymmetry coefficients described in the following section) is better suited.

1.3 Angular distributions

In a chosen reference frame, let's now discuss which form the angular distributions of the decay leptons can take.

1.3.1 General form

The most general form of the differential cross section for the process of vector boson production in pp collisions, and subsequent leptonic decay, can be obtained by the convolution of partonic luminosities f_a,f_b with the elementary cross section. In terms of the Mandelstam variables one can write [8]:

$$\frac{d\sigma_{TOT}}{dp_T^2\ dy\ d\Omega^*} = \sum_{ab} \int dx_1 dx_2\ f_a(x_1, q^2) f_b(x_2, q^2) \frac{s\ d\sigma_{ab}}{dt\ du\ d\Omega^*}(x_1 P_1, x_2 P_2, \alpha_s(q^2)) \tag{1.3}$$

The σ_{ab} derives from the contraction of a leptonic tensor $L_{\mu\nu}$, accounting for the leptonic current in the final state, with a hadronic tensor $H_{ab}^{\mu\nu}$, that describes the coupling of the hadronic current to the weak force propagator.

It's useful to note that, in the framework of this analysis, $L_{\mu\nu}$ acts merely as an analyzer of the structure of $H^{\mu\nu}$, which carries the effective information about the polarization of the vector boson produced in the interaction. The exact form of $H_{\mu\nu}$ and $L_{\mu\nu}$ can be found in the literature [8].

From an effective point of view, the elementary cross section can be written [8], in the W/Z rest frame, as a sum of nine contributions, that display very different properties in terms of discrete symmetries:

$$\frac{d\sigma}{dp_T^2\ dy\ d\Omega^*} = \sum_{\lambda} g_\lambda(\theta^*, \phi^*) \frac{3}{16\pi} \frac{d\sigma^\lambda}{dp_T^2\ dy} \tag{1.4}$$

where the sum over lambda runs over the set $\Lambda = \{U, 0, 1, 2, 3, 4, 5, 6, 7\}$, and the angular distributions g_λ take the following form:

$$
\begin{aligned}
g_U(\theta^*, \phi^*) &= 1 + \cos^2\theta^* & \qquad g_3(\theta^*, \phi^*) &= 4\sqrt{2}\sin\theta^*\cos\phi^* \\
g_0(\theta^*, \phi^*) &= 1 - 3\cos^2\theta^* & \qquad g_5(\theta^*, \phi^*) &= 2\sin^2\theta^*\sin 2\phi^* \\
g_2(\theta^*, \phi^*) &= 2\sin^2\theta^*\cos 2\phi^* & \qquad g_6(\theta^*, \phi^*) &= 2\sqrt{2}\sin 2\theta^*\sin\phi^* \\
g_1(\theta^*, \phi^*) &= 2\sqrt{2}\sin 2\theta^*\cos\phi^* & \qquad g_7(\theta^*, \phi^*) &= 4\sqrt{2}\sin\theta^*\sin\phi^* \\
g_4(\theta^*, \phi^*) &= 2\cos\theta^*
\end{aligned}
$$

The terms that contain a ϕ^* dependence will not contribute to the cross section after an integration over ϕ^*.

Discussing now the different terms of Eq. 1.4: g_U corresponds to the production cross section of unpolarized bosons; the other terms modify this distribution with different shapes in the (θ^*, ϕ^*) plane.

The most interesting of them is g_4, that's directly correlated to $f_L - f_R$ as will become clear in the following.

The σ U,0,1,2,7 terms derive from the parity-conserving part of the $H_{\mu\nu}$ tensor; the σ 3,4,5,6 terms are parity-violating. Under a P transformation, however, also the g 3,4,7 change sign; as a consequence, the angular distributions arising from the U,0,1,2,3,4 terms do not change under parity.

Actually, it can be seen that the following relations between the σ and the vector (v) and axial (a) coupling of the boson to the lepton (subscript l) and quark (subscript q) current hold:

$$
\sigma_\lambda \propto \begin{cases} (v_l^2 + a_l^2)(v_q^2 + a_q^2) \text{ if } \lambda \in \{U, 0, 1, 2\} \\ v_l a_l v_q a_q \text{ if } \lambda \in \{3, 4\} \\ (v_l^2 + a_l^2) v_q a_q \text{ if } \lambda \in \{5, 6\} \\ (v_q^2 + a_q^2) v_l a_l \text{ if } \lambda \in \{7\} \end{cases} \tag{1.5}
$$

Therefore, only the 5,6,7 angular distributions do change sign under a change from V-A to V+A coupling in the Lagrangian (i.e. to a change of sign of the axial couplings). Their contribution at the LHC has been studied [2]: all of them are found to be negligible in the Standard Model (Fig. 1.4).

A more common and experimental-friendly version of this parametrization can be obtained with the following procedure: let's factorize out of the sum the unpolarized cross-section, and introduce the following coefficients:

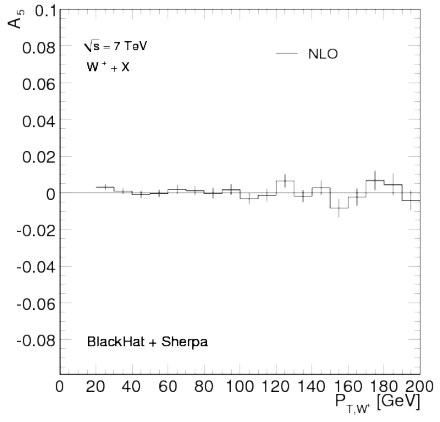

Figure 1.4: A_5 asymmetry coefficient evaluated at NLO for LHC conditions, as a function of p_T . A_5 (like A_6 and A_7) is consistent with 0 within the statistical uncertainty. [2]

$$A_0 = \frac{2d\sigma^L}{d\sigma^U} \qquad A_1 = \frac{2\sqrt{2}d\sigma^I}{d\sigma^U} \qquad A_2 = \frac{4d\sigma^T}{d\sigma^U} \tag{1.6}$$

$$A_3 = \frac{4\sqrt{2}d\sigma^A}{d\sigma^U} \qquad A_4 = \frac{2d\sigma^P}{d\sigma^U} \tag{1.7}$$

$$\tag{1.8}$$

so that eq. 1.4 becomes:

$$\begin{aligned}\frac{d\sigma}{dp_T^2\ dy\ d\cos\theta^* d\phi^*} = \frac{3}{16\pi}\frac{d\sigma^U}{dp_T^2\ dy}[&(1+\cos^2\theta^*)\\ &+ \frac{1}{2}A_0(1-3\cos^2\theta^*)\\ &+ A_1\sin 2\theta^*\cos\phi^*\\ &+ \frac{1}{2}A_2\sin^2\theta^*\cos 2\phi^*\\ &+ A_3\sin\theta^*\cos\phi^*\\ &+ A_4\cos\theta^*]\end{aligned}$$

1.3.2 Integrated distributions

From the experimental point of view, it can be useful (especially in the first period of data taking, when the statistics are limited) to integrate out one of the two variables, and carry out a one-dimensional angular distribution measurement.

If one integrates away the ϕ^*, the following terms remain:

$$\frac{d\sigma}{dp_T^2\ dy\ d\cos\theta^*} = C(1 + \alpha_1 \cos\theta^* + \alpha_2 \cos^2\theta^*) \tag{1.9}$$

where:

$$C = \frac{3}{8}\frac{d\sigma^U}{dp_T^2\ dy}\left(1 + \frac{A_0}{2}\right) \qquad \alpha_1 = \frac{2A_4}{2 + A_0} \qquad \alpha_2 = \frac{2 - 3A_0}{2 + A_0} \tag{1.10}$$

It's possible to identify:

$$f_L = \frac{1}{4}(2 - A_0 \mp A_4) \qquad f_R = \frac{1}{4}(2 - A_0 \pm A_4) \qquad f_0 = \frac{1}{2}A_0 \tag{1.11}$$

and it will be important in the following that $f_L - f_R = \mp A_4/2$.

Similarly, if θ^* is integrated instead:

$$\frac{d\sigma}{dp_T^2\ dy\ d\phi^*} = D(1 + \beta_1 \cos\phi^* + \beta_2 \cos 2\phi^* + \beta_3 \sin\phi^* + \beta_4 \sin 2\phi^*) \tag{1.12}$$

where:

$$D = \frac{1}{2\pi}\frac{d\sigma^U}{dp_T^2\ dy} \qquad \beta_1 = \frac{3}{4}A_3 \qquad \beta_2 = \frac{1}{4}A_2 \tag{1.13}$$

$$\beta_3 = \frac{3}{4}A_7 \qquad \beta_4 = \frac{1}{2}A_5 \tag{1.14}$$

It can also be useful to notice that:

$$f_L = -\frac{1}{2}\mp < \cos\theta^* > + \frac{5}{2} < \cos^2\theta^* > \qquad f_R = -\frac{1}{2}\pm < \cos\theta^* > + \frac{5}{2} < \cos^2\theta^* > \tag{1.15}$$

$$A_0 = 4 - 10 < \cos^2\theta^* > \qquad A_1 = 5 < \sin 2\theta^* \cos\phi^* > \qquad A_2 = 10 < \sin^2\theta^* \cos 2\phi^* > \tag{1.16}$$

$$A_3 = 4 < \sin\theta^* \cos\phi^* > \qquad A_4 = 4 < \cos\theta^* > \qquad A_5 = 4 < \sin\theta^* \sin\phi^* > \tag{1.17}$$

$$A_6 = 5 < \sin 2\theta^* \sin\phi^* > \qquad A_7 = 5 < \sin^2\theta^* \sin 2\phi^* > \tag{1.18}$$

where the brackets indicate the expectation value on the (θ^*, ϕ^*) plane according to the $d\cos\theta^* d\phi^*$ measure.

	W^+ NLO	W^+ ME+PS	W^+ LO	W^- NLO	W^- ME+PS	W^- LO
f_L	0.554	0.545	0.556	0.528	0.516	0.523
f_R	0.246	0.267	0.246	0.279	0.303	0.287
f_0	0.200	0.188	0.198	0.193	0.181	0.190

Table 1.2: Theoretical predictions for polarization fractions for W production with $p_T^W > 50$ GeV and no restrictions on either the W rapidity or the number of associated jets at the LHC. [2]

1.4 Theoretical predictions

The Blackhat Collaboration has recently published [2] accurate Standard-Model predictions for polarization fractions of W bosons produced in association with jets at the LHC.

They have used the Blackhat software [9], in conjunction with Sherpa [10], to obtain NLO results for W + 4-jets and Z, γ^* + 3-jets processes [11].

The Blackhat software is able to take advantage of analytical results, when available (for example in events with less than 2 jets), falling back to numerical calculation in all other situations. In every case, the full Breit-Wigner shape of resonances is always taken into account, and - crucial aspect for this analysis - all spin correlations are conserved in leptonic decays.

The predictions for polarization fractions of W bosons are given in Table 1.2, with a cut on W $p_T > 50$ GeV/c and no restriction on W rapidity and number of jets. All the predictions for NLO, ME+PS and LO calculations are reported.

The uncertainty arising from factorization and renormalization scales affect these results by a very small amount (under 2%), because polarization fractions are given instead of absolute-scale cross-sections. The total theoretical uncertainty can be estimated from the difference between the NLO and ME+PS values [2].

The dependence of f_L, f_R, f_0 on W p_T is plotted in Fig. 1.5, 1.6, 1.7. The simulation shows f_0 falling down at high p_T and f_L rising up to an asymptotic value.

Interestingly, Fig. 1.8 shows, at low W p_T , an enhancement of the left-handed component at large rapidities. At high transverse momenta, instead, the large polarization comes from central rapidities. Such features will be qualitatively justified in the following section.

It has also been shown [2] that, while the polarization fractions are heavily dependent on the global p_T scale (i.e. the W p_T), they're very little dependent on the number of recoiling jets (also at NLO, Fig. 1.9), and to the details of how jets are defined (for example, the p_T cut applied to them, Fig. 1.10).

In a similar way, predictions for asymmetry coefficients A_i are presented in Table 1.3 and

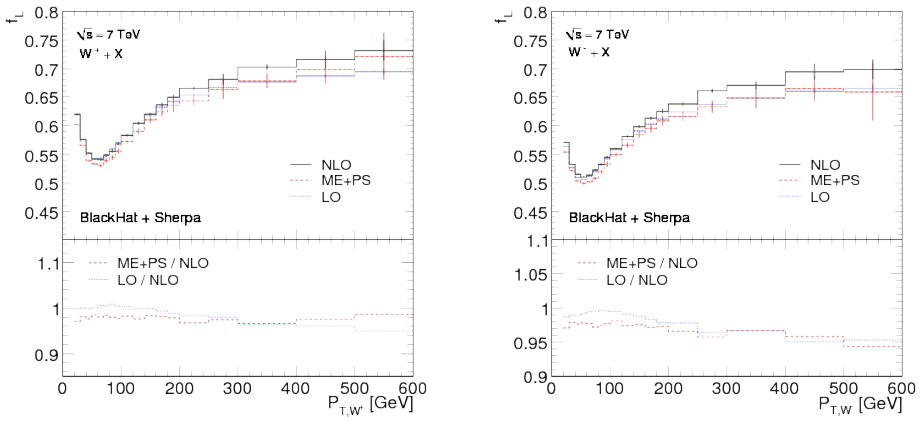

(a) (b)

Figure 1.5: Theoretical prediction for left-handed polarization fraction f_L as a function of a) W^+ b) W^- p_T at the LHC. [2]

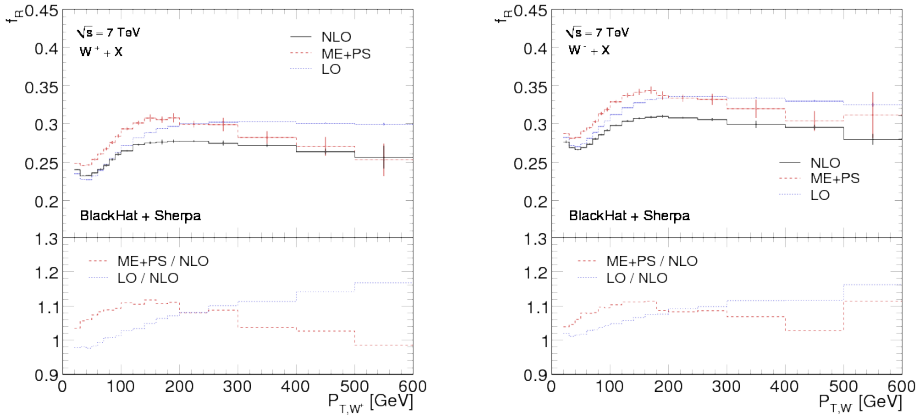

(a) (b)

Figure 1.6: Theoretical prediction for right-handed polarization fraction f_R as a function of a) W^+ b) W^- p_T at the LHC. [2]

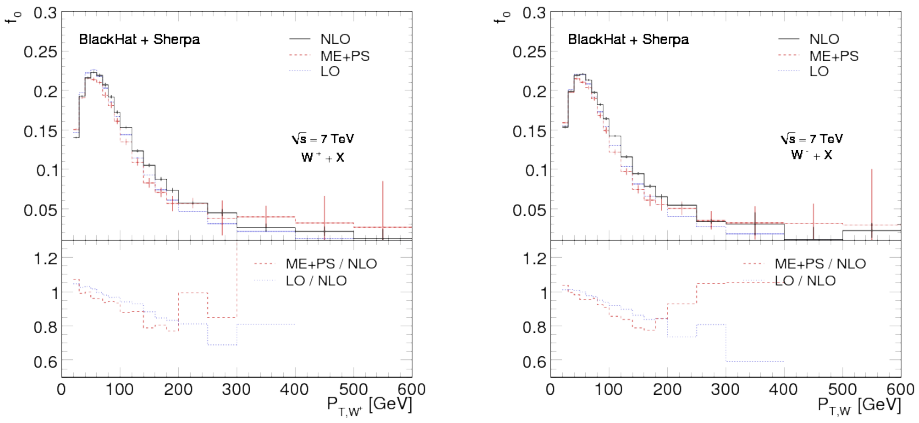

(a) (b)

Figure 1.7: Theoretical prediction for longitudinal polarization fraction f_0 as a function of a) W^+ b) W^- p_T at the LHC. [2]

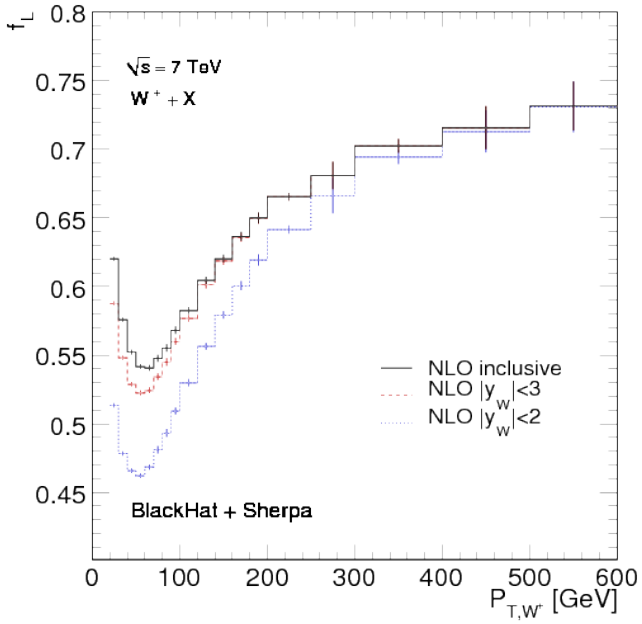

Figure 1.8: f_L polarization fraction as a function of W^+ p_T , with different rapidity acceptance cuts. At low p_T , left-handed polarization is enhanced if events with W^+ flying along the beam axis are included; at large p_T , polarization comes from effects in the transverse plane. [2]

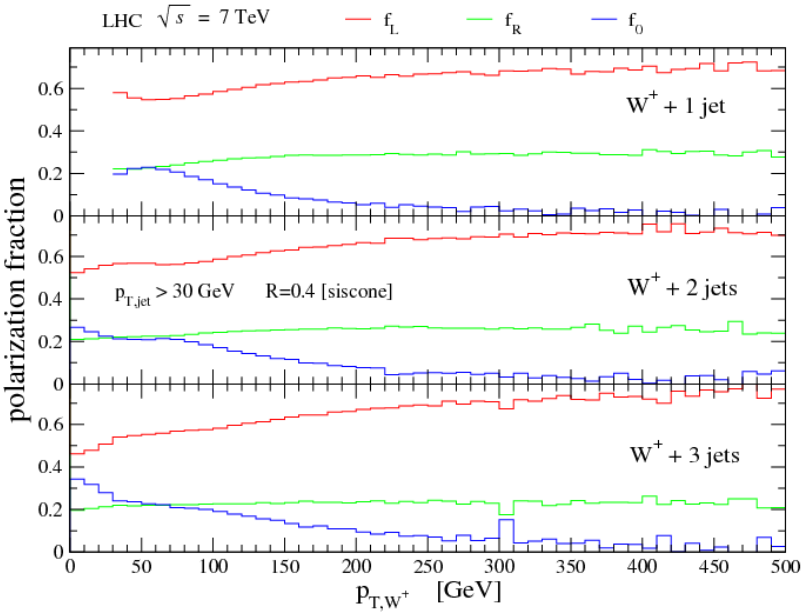

(a) W+n-jets

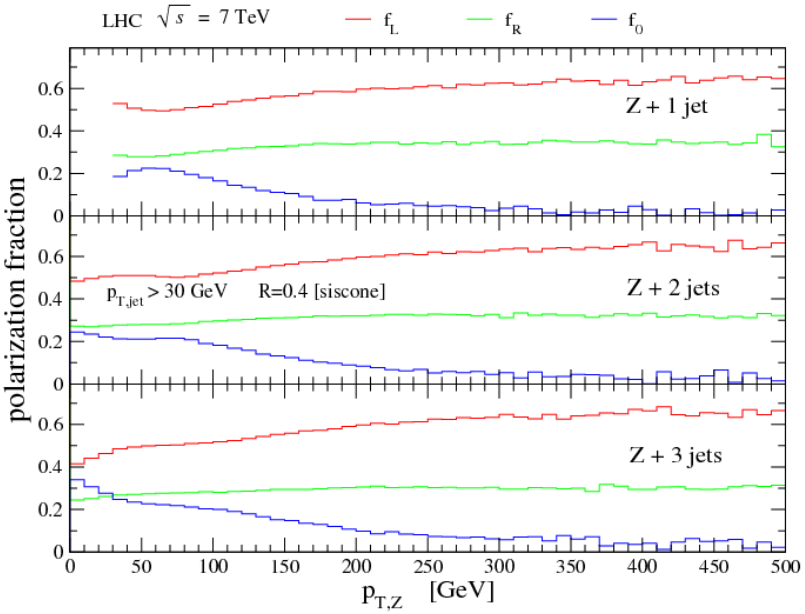

(b) Z+n-jets

Figure 1.9: LO polarization fractions for W/Z+n-jets production at the LHC, integrated in y. The results are very little sensitive to the number of jets in the event. [2]

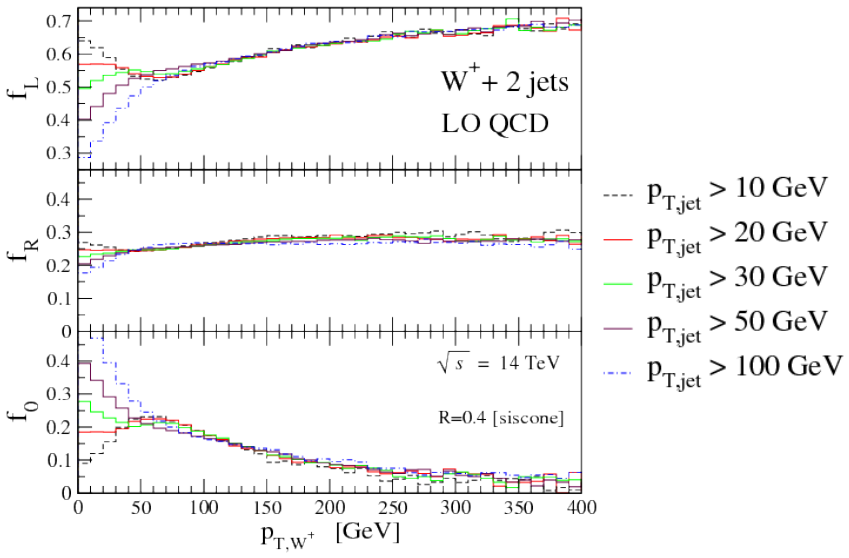

Figure 1.10: LO polarization fractions for W + 2 jets production at the LHC, integrated in y, for different p_T cuts used for jet definition, as a function of W p_T . Except that for low W p_T , there is negligible dependence on the details of jet definition. [2]

in Fig. 1.11. The uncertainty is about 15% for A_1 and A_4, larger for the other components.

In the analysis, we choose a cut on W $p_T > 50$ GeV/c because, at the experiments, it's necessary to make a compromise between polarization enhancement at high p_T , and finite statistics; another important element to take into account is limited lepton acceptance, which requires corrections to be introduced at the analysis level.

	W^+ NLO	W^+ ME+PS	W^+ LO	W^- NLO	W^- ME+PS	W^- LO
A_0	0.399	0.376	0.395	0.386	0.362	0.380
A_1	−0.116	−0.097	−0.134	−0.109	−0.095	−0.130
A_2	0.318	0.384	0.395	0.310	0.376	0.379
A_3	−0.013	−0.057	−0.014	−0.001	0.033	−0.001
A_4	−0.616	−0.557	−0.619	0.497	0.427	0.471

Table 1.3: Theoretical predictions for A_i coefficients for W production with $p_T^W > 50$ GeV and no restrictions on either the W rapidity or the number of associated jets at the LHC. [2]

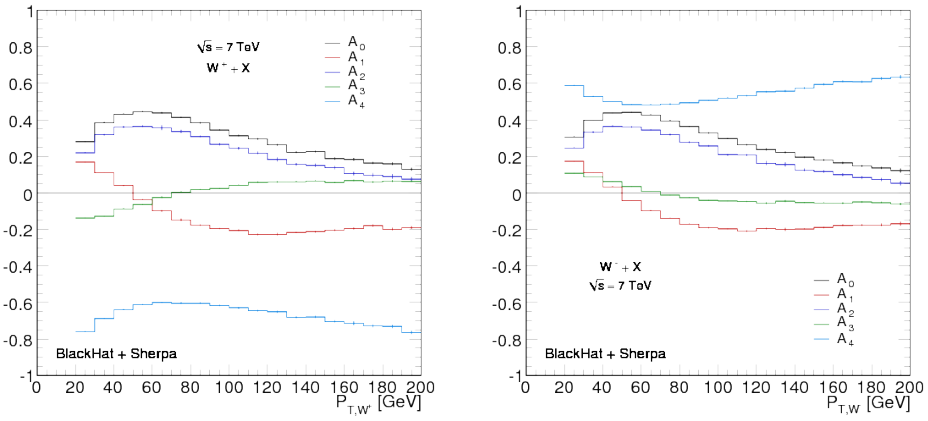

(a) (b)

Figure 1.11: Theoretical prediction for A_i asymmetry coefficients as a function of a)W^+ b)W^- p_T at the LHC. [2]

1.5 Mechanism of vector boson polarization at LHC

As discussed in the previous sections, quantifying the dominant left-handed polarization of vector bosons at LHC requires numerical calculations that can be found in the literature [12].

However, it's possible to predict the qualitative behaviour of the polarization using the angular momentum conservation [2].

In this section, the case of the W boson production will be explicitly treated; afterwards, the differences in the case of the Z will be briefly discussed.

1.5.1 W production at low p_T

Before studying the case of W polarization at high p_T , let's consider the simpler case of a W produced along the beam axis (i.e., with negligible p_T) in a collision of hadrons. At the leading order, the only way to produce a W is through a quark-antiquark pair in the initial state: $u\bar{d}$ for the W^+ , $\bar{u}d$ for the W^- .

At the LHC, the parton distribution functions for protons will favour the production of the W in the same direction of the quark (opposed to the anti-quark) taking part in the process; this is due to the fact that, in order to produce a W at high rapidity, one of the two partons has to carry a large fraction x of the proton's momentum (Fig. 1.12a), and, in the $x \to 1$ region, the parton distribution functions favour quarks instead of anti-quarks and gluons (Fig. 1.12b).

Taking into account the pure V-A coupling of the W to fermions in the Standard Model, it can be seen immediately from angular momentum conservation that the spin of the W has to be directed along the flight direction of the anti-quark; therefore, the W is left-handed, and

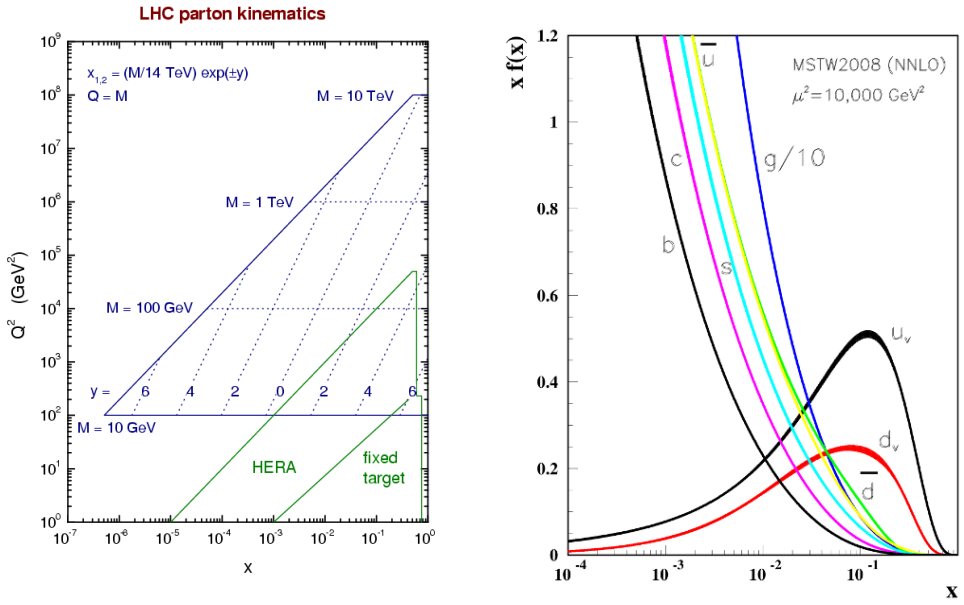

(a) (b)

Figure 1.12: a) Kinematically accessible region of the (x, q^2) plane at LHC [14]. b) Unpolarized parton distribution functions, using the NNLO MSTW2008 parametrization [15].

this argument is valid for both W^+ and W^- production in this kinematic regime (Fig. 1.13). The charge asymmetry in W production has been measured in [13].

1.5.2 W production at large p_T

The case of a W boson produced with significant p_T and recoiling from jets is more complex.

For W^+ production (for W^- the argument holds without significant changes), three processes can come into play already at the leading order: $ug \to W^+d$, $u\bar{d} \to W^+g$, and $g\bar{d} \to W^+\bar{u}$.

The ratios between their contributions, at large W p_T , are dominated by the parton luminosities at large x. At large x, actually, the following inequality holds for parton distribution

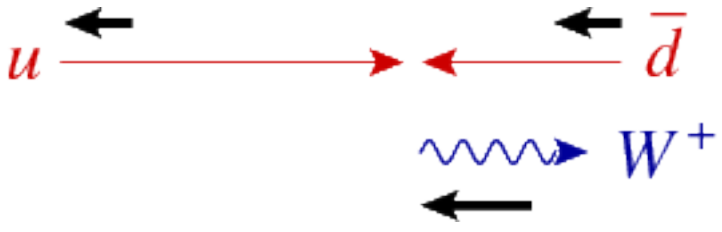

Figure 1.13: Production of W bosons at low p_T. The pure coupling to left-handed fermions determines an enhanced left-handed polarization in this kinematic regime [2].

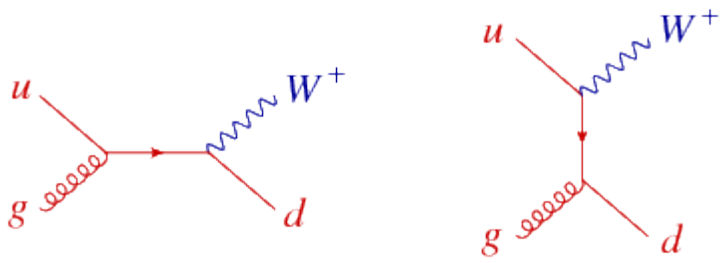

Figure 1.14: The two leading-order Feynman diagrams for W production through the ug subprocess.

functions: $q(x) \gg g(x) \gg \bar{q}(x)$ (Fig. 1.12b) and, as a consequence:

$$\sigma(ug \to W^+ d) \gg \sigma(u\bar{d} \to W^+ g) \gg \sigma(g\bar{d} \to W^+ \bar{u})$$

Let's consider the dominant contribution from the quark + gluon initial state. Two Feynman graphs (Fig. 1.14) define this subprocess at the leading order; the s-channel one is the most interesting for left-handed polarization at high p_T .

In that graph, actually, an off-shell u quark decays to an on-shell right-handed d quark and a W^+ ; the u quark has spin 1/2, so considering the angular momentum along the axis spanned by the W^+ and the d quark it is easily seen that the W^+ cannot be right-handed, because this would make the total angular momentum 3/2.

The longitudinal mode is also suppressed for large tranverse momenta of the W^+ from other theoretical arguments [2, 16]. Therefore, the W^+ will be 100% left-handed at large p_T .

However, also the t-channel graph has to be considered. To see that its contribution is a minor one at high p_T , a more refined argument dealing with gluon polarization comes into play.

Writing down the amplitude for the t-channel, actually, the term $\epsilon^{\pm}_{\mu}(k_g, q)\gamma^{\mu}|k_d^+ >$ is derived for the gluon - d quark interaction vertex, where $\epsilon^{\pm}_{\mu}(k_g, q)$ is the polarization vector of the gluon, and $|k_d^+ >$ the Weyl spinor for the outgoing d-quark.

It's useful to introduce a spinor-helicity representation for ϵ_{μ} in terms of the reference momentum q. Rewriting the contraction of the $\epsilon^{\pm}_{\mu}$ with γ^{μ} one obtains:

$$\epsilon^+_{\mu}(k_g, q) = \frac{\sqrt{2}|k_g^- >< q^-|}{(q, k_g)}$$

$$\epsilon^-_{\mu}(k_g, q) = -\frac{\sqrt{2}|q^- >< k_g^-|}{(q, k_g)}$$

If the gluon is left handed, the ϵ^+_{μ} term appears in the amplitude, which means that it's proportional to $< q^-|k_d^+ >= (q, k_d)$; therefore, it's possible to choose q so that $(q, k_d) = 0$ and

the amplitude vanishes.

On the other hand, if the incoming gluon is right-handed, the ϵ_μ^- has to be used. In this case, there is no way of directly cancelling the amplitude; actually, there is no definite polarization of the W in the final state.

The amplitudes for W production and leptonic decay are found [2] to depend (at LO) on the quadrimomenta of particles involved in the following way:

$$|M_L|^2 = \frac{(k_d, k_\nu)^2}{(k_u, k_g)(k_g, k_d)} \tag{1.19}$$

$$|M_R|^2 = \frac{(k_u, k_e)^2}{(k_u, k_g)(k_g, k_d)} \tag{1.20}$$

where L,R refer to left, right handed polarization of the gluon, and are shared by all the qg, $q\bar{q}$ and $g\bar{q}$ processes, because they are related by crossing symmetry.

Let's define θ^* the polar angle between the z-axis and the charged lepton.

It's important to note the $(k_d, k_\nu)^2$ factor in the numerator of Eq. 1.19; once evaluated in the W rest frame (i.e. the frame obtained by the partonic center-of-mass frame by boosting along the W flight direction), this results in the $(1 - \cos\theta^*)^2$ distribution, i.e. to 100% left-handed polarization component, as already discussed for the s-channel ug graph.

On the other hand, for the Eq. 1.20, the product $(k_u, k_e)^2$ cannot be directly related to a definite polarization of the W.

However, let's suppose that the W is produced with very high p_T in the transverse plane. By considering the quadrimomentum conservation equality $k_u + k_g = k_W + k_d$ in the W rest frame, and assuming the u quark and the gluon to have similar momentum, it is easily seen that $k_u \approx k_d/2$. Therefore, the $(k_u, k_e)^2$ factor becomes $\frac{1}{4}(-k_d, k_e)^2$, which yields a $\frac{1}{4}(1 + \cos\theta^*)^2$ distribution for the decay lepton, i.e. a right handed polarization for the W.

In the end, the dominant left-handedness of the W boson produced is due to the fact that the squared matrix element for the s-channel graph is about four times larger than the one for the t-channel at high W p_T (Fig. 1.15a). As a consequence, a reasonable estimate for asymptotic W polarization is $f_L \approx 80\%$ (events initiated by a left-handed gluon), $f_R \approx 20\%$ (right-handed gluon). The longitudinal component is suppressed [2, 16].

The subleading contribution from the $u\bar{d} \to W^+ g$ process can be analyzed in a similar way. Also in this case, the first graph leads preferentially to left-handed W bosons, while the second leads to right-handed ones (Fig. 1.15b). In this case, however, a cancellation takes

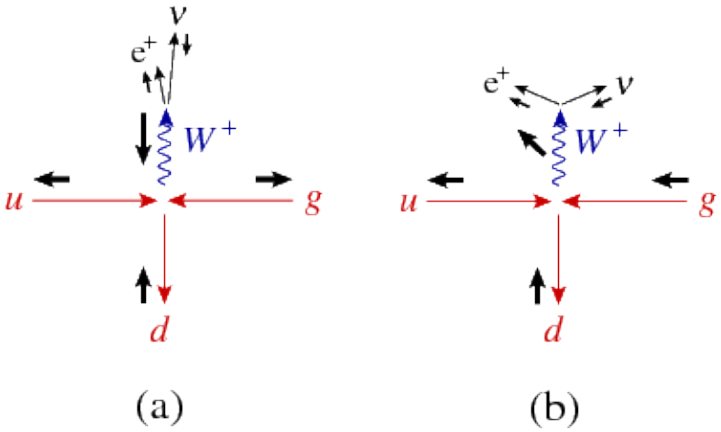

(a) ug subprocess

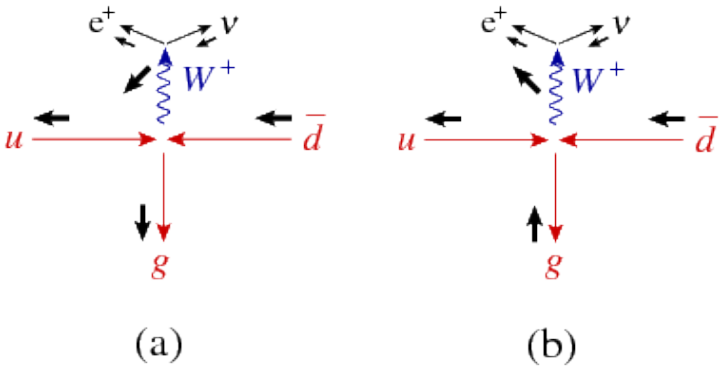

(b) $u\bar{d}$ subprocess

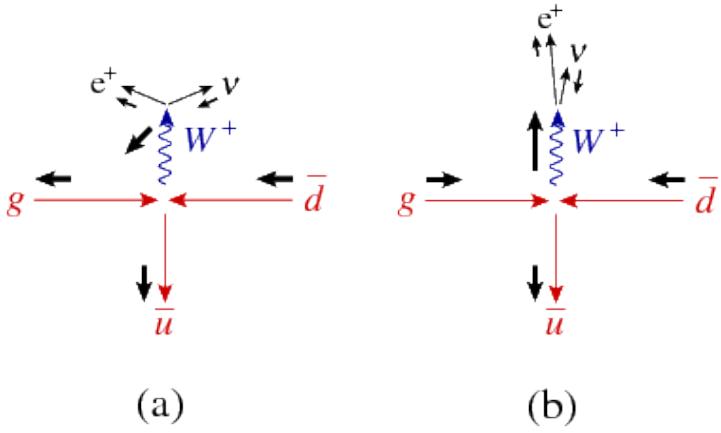

(c) $g\bar{d}$ subprocess

Figure 1.15: Subprocesses for W production at the LHC. The additional arrows indicate dominant polarization, for (a) left-handed (b) right-handed incoming gluon. [2]

place between amplitudes for transverse plane scattering, so there is no contribution to overall left-handed polarization in the final state.

The minor contribution from $g\bar{d} \rightarrow W^+\bar{u}$ leads to dominant right-handedness (Fig. 1.15c), but - as already shown - is suppressed by the PDFs at large x.

In conclusion, the expected polarization for W bosons produced in pp collisions should tend to 80% left-handed, 20% right-handed in the limit of high p_T .

Away from the asintotic behaviour in terms of p_T , the expectation for the left-handed component will be smaller for several reasons: in the first place, the t-channel contribution will have a greater impact with respect to the s-channel; secondly, the subleading processes initiated by $q\bar{q}$ and $g\bar{q}$ won't be negligible anymore as x moves away from 1 (Fig. 1.12).

This argument also suggests that f_L for W^+ is predicted to be larger, at fixed W p_T , than f_L for W^- : actually, in the proton the u quark tends to have larger x than the d quark; therefore, it's reasonable to think that the $ug \rightarrow W^+d$ process will become dominant more easily (i.e. at lower W p_T) than its $dg \rightarrow W^-u$ charge counterpart.

Moreover, if the p_T of the W is finite it will be important to consider that its direction of flight in the laboratory frame will be different from the one seen from the center-of-mass frame of the two initial state partons, that's the one all of the former arguments refer to.

1.5.3 Z polarization

Very similar arguments hold also for the case of Z boson production.

However, the different characteristics of coupling have to be considered: the coupling of the Z to quarks (that comes into play for the production of the Z) does not involve the chirality projector $\frac{1-\gamma^5}{2}$, but is still quite asymmetric between left and right handedness; therefore, polarization fractions predicted for the Z do not differ significantly from those for the W, and also the qualitative arguments still hold the same.

On the contrary, the polarization analyzing power of Z leptonic decay - i.e. the ability to distinguish between different polarization states from final-state angular distributions - is severely affected by the coupling to right-handed leptons, which is similar to the coupling to left-handed leptons (Table 1.4).

As a consequence, the angular coefficients f_L, f_R, f_0 can no longer be interpreted as polarization fractions of the Z boson; the following matrix transformation relates them to the polarization fractions V_i:

Table 1.4: Z boson couplings to fermions.

	c_L	c_R	$\left(\frac{c_L^2}{c_R^2}\right)$
ν	$\frac{1}{2}$	0	-
$\ell^{\pm}$	$\pm\frac{1}{2} \mp \sin^2(\theta_W)$	$\mp\sin^2(\theta_W)$	1.36
$q_1(+\frac{2}{3})$	$\frac{1}{2} - \frac{2}{3}\sin^2(\theta_W)$	$-\frac{2}{3}\sin^2(\theta_W)$	5.05
$q_2(-\frac{1}{3})$	$-\frac{1}{2} + \frac{1}{3}\sin^2(\theta_W)$	$\frac{1}{3}\sin^2(\theta_W)$	30.2

$$\begin{pmatrix} V_L \\ V_R \\ V_0 \end{pmatrix} = \frac{c_L^2 + c_R^2}{c_L^4 - c_R^4} \begin{pmatrix} c_L^2 & -c_R^2 & 0 \\ -c_R^2 & c_L^2 & 0 \\ 0 & 0 & \frac{c_L^4 - c_R^4}{c_L^2 + c_R^2} \end{pmatrix} \begin{pmatrix} f_L \\ f_R \\ f_0 \end{pmatrix} \tag{1.21}$$

For example, $f_L = 0.408$, $f_R = 0.375$, $f_0 = 0.216$ correspond to a 50% left, 28% right and 22% longitudinal polarization.

This fact, together with lower cross sections than for W production, will limit significantly the precision of polarization measurements in Z+jets events with respect to W+jets events, at a given integrated luminosity.

1.5.4 Differences at a $p\bar{p}$ collider

It's useful to note that at the Tevatron, which is a $p\bar{p}$ collider, these arguments have to be changed.

For the case of low-p_T W, if the W^+ continue to be preferentially produced in the same direction of the incoming u quark - therefore being left-handed -, the W^- are now preferentially produced along the flight direction of the $\bar{u}$ quark (that tends to carry a larger fraction of the anti-proton's momentum compared to the d quark in the proton), and so are right-handed.

In both cases, charged decay leptons (l^+ for W^+, l^- for W^-) tend to be produced in the central region of the detector. This dilution of the charge asymmetry measured in terms of the charged lepton rapidity has been observed experimentally [17].

For high-p_T bosons, instead, the $q\bar{q}$ initial state becomes dominant in the $p\bar{p}$ case (because of the presence of valence anti-quarks in the $\bar{p}$), and does not provide a preferential polarization for the W; therefore, for both W^+ and W^- , f_L and f_R assume similar values. The other sub-dominant processes (qg, $g\bar{q}$) provide a mild left-handed polarization for W^+ produced in the p flight direction [2].

Chapter 2

Physics objects at CMS

The vector boson polarization analysis uses a variety of physics objects; the most important ones are muons and electrons, whose distributions are measured in the final state, and the missing transverse energy, that has an important role in W+jets events, where it's used for both event selection and W p_T reconstruction.

The main properties of the CMS detector and the physics objects relevant for the analysis, with respect to their reconstruction, selection and identification, will be discussed in the following, and their use in the event trigger of the experiment will be briefly described.

2.1 LHC and CMS

The Large Hadron Collider (LHC) is a proton-proton collider operated by CERN in the 27 km - long tunnel that used to host the LEP electron-positron collider.

Two counter-rotating proton beams are circulated in extreme vacuum conditions thanks to the dipole magnetic field generated by the superconducting magnets. The design bunch spacing time is 25 ns.

Other accelerators existing at CERN for previous experiments (LINAC, BOOSTER, PS, SPS) work as an injection chain for the LHC, where protons can be finally accelerated from 450 GeV up to 3.5 TeV (it is expected that in 2014 the beam energy will reach a value close to the design value of 7 TeV).

The peak design luminosity to be delivered to the experiments is 10^{34} cm^{-2}s^{-1}; an instantaneous luminosity in excess of 10^{33} cm^{-2}s^{-1} has already been reached.

During 2010, LHC has provided experiments with an integrated luminosity of approximately 45 pb^{-1} at $\sqrt{s} = 7$ TeV; in the higher luminosity 2011 run, more than 1 fb^{-1} has already been accumulated.

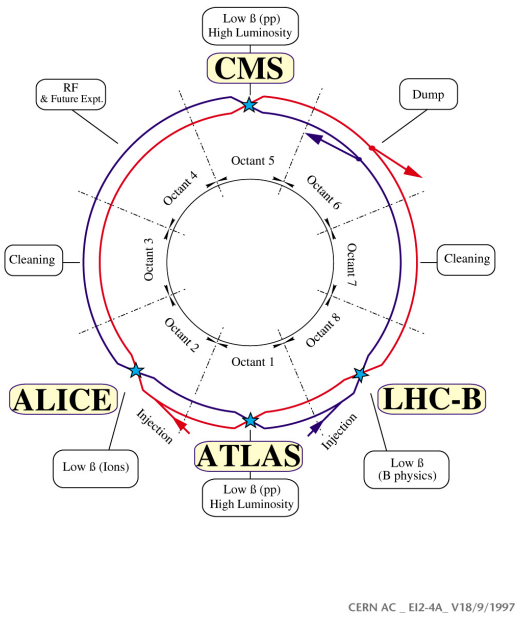

Figure 2.1: Schematic view of the LHC accelerator with experiments.

LHC features (Fig. 2.1) two general-purpose large experiments, ATLAS and CMS, together with LHCb (designed for studying B-physics) and ALICE (aiming at heavy ions collision studies).

The Compact Muon Solenoid (CMS) detector has been designed to face the very high rate of interactions expected to take place at the very high LHC design luminosity.

This requires a very efficient online event selection (Trigger), a high-granularity design, and radiation-hard materials and electronics.

The combined use of a variety of subdetectors yields a very good muon and electron identification and resolution over a wide range of p_T and a highly-efficient track reconstruction, together with a good performance in measurement of electromagnetic energy and of missing transverse energy, thanks to the hermetic coverage of a large acceptance region.

CMS features a powerful superconducting coil, generating a solenoidal magnetic field of $\sim$ 3.8 T in a large volume, which hosts different subdetectors. The magnetic field lines close, in the outer region, through a steel joke (Fig. 2.2).

At the core of the experiment, the inner silicon tracking system records the trajectories of charged particles that are bent by the magnetic field.

The CMS tracker consists of a pixel detector, surrounded by silicon strip layers, with an acceptance extending up to $|\eta| = 2.5$.

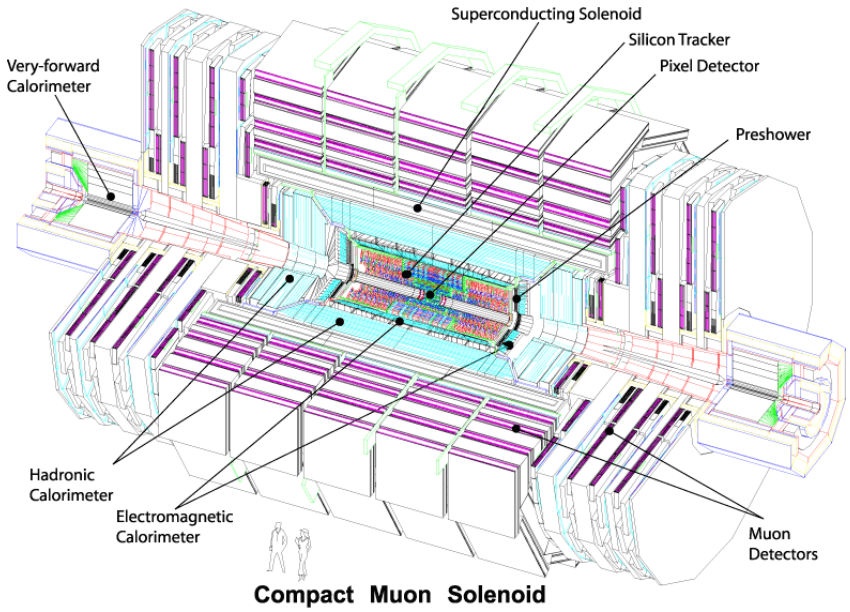

Figure 2.2: Schematic view of the CMS apparatus.

At a larger distance from the beam pipe, the electromagnetic calorimeter (ECAL) is made of high-density and high-granularity lead tungstate crystals, that feature a short radiation length and a good energy and position resolution. They are complemented by a preshower detector in the endcap region, and cover the region $|\eta| < 3$.

Behind the ECAL, there is the hadron calorimeter (HCAL), which is divided in different subdetectors as a function of η, and covers the region up to $|\eta| < 5$.

The bulk of the subdetectors mentioned above are contained within the superconducting coil; at a larger distance from the beam pipe, the steel return joke for the magnetic field works as an additional hadron absorber, and is used as a support for the gaseous multi-layer detectors that form the muon system: the drift tubes (DT), the cathode strip chambers (CSC) and the resistive plate chambers (RPC).

A much more detailed description of the CMS experiment can be found elsewhere [18, 19].

2.2 Muons

2.2.1 Reconstruction

Muons are reconstructed in CMS [18–20] thanks to different sub-detectors: the silicon tracker, which is the core of the experiment, and different types of muon chambers installed outside the solenoid, on the steel return yoke of the magnet.

The acceptance (Fig. 2.3) of the whole muon system extends up to 2.4 in $|\eta|$: the $|\eta| < 1.2$ region is covered by the Drift Tube (DT) chambers; the Cathode Strip Chambers (CSC) are between 0.9 and 2.4; additionally, the Resistive Plate Chamber (RPC) system is present for $|\eta| < 1.6$.

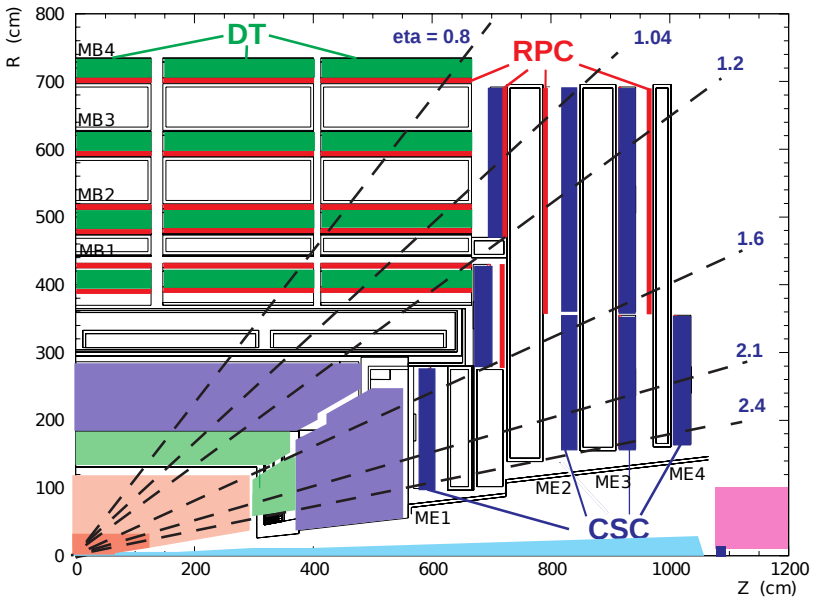

Figure 2.3: Schematic representation of a quadrant of CMS. The muon system, comprising the Drift Tubes, the Cathode Strip Chambers and the Resistive Plate Chambers, are highlighted.

The muon reconstruction algorithm at CMS takes advantage of this redundancy of detection methods. The first step is track reconstruction, done independently in the tracker ("tracker track") and in the muon system ("standalone-muon track"). Then, one tries to match the two types of tracks.

Two different approaches can be used here:

- *outside-in*: starting from a standalone-muon track, a matching tracker-track is found; then, the fit of the track is repeated using the hits both in the tracker and in the muon system. The resulting object is called a "global muon", and its resolution gets improved, at high p_T , with respect to the tracker-only fit.

- *inside-out*: each tracker track is extrapolated to the muon system region; this is a delicate step, because it's necessary to take into account the energy loss and the uncertainty due to the multiple scattering in a large amount of material (calorimetry and coil). If a muon segment (i.e. a subset of a real track in the muon system) is found to match the extrapolation, this object is called a "tracker muon". This algorithm is useful for low-p_T muons, that are not expected to fully penetrate the muon system, and therefore do not generate a full standalone-muon track, but only a few hits.

If no match is found when extrapolating outside in, the standalone-muon track is stored as a "standalone muon". This happens only for less than 1% of the muons produced in a collision.

2.2.2 Selection and identification

Several variables can be used to improve muon quality selection and identification, at the level of the analysis.

In order to understand better these different characteristics, it's useful to distinguish muons, according to their source, into the following categories:

- Prompt muons: those generated by W,Z, promptly produced quarkonia, Drell-Yan processes and top production.
- Muons from heavy flavour: muons result of the decay of a beauty or charmed hadron, or a tau lepton.
- Muons from light flavour: muons from the in-flight decay of a light hadron (π or K).
- Hadron punch-through: signals in the muon system produced by a particle other than a muon, not contained by the calorimeters.

Muons from b-hadrons have a major role for p_T up to about 30 GeV/c. At higher p_T , W and Z production are the main sources of (prompt) muons (Fig. 2.4).

Different standard muon selections are available for analyses at CMS:

- Soft muon: a tracker muon, with an additional quality check on the matching muon segment, that must not be a better match for another track. This selection is optimized for low-p_T muons, and used mainly in the B-physics analyses.
- Tight muon: a global muon, with an additional goodness-of-fit requirement (normalized $\chi^2 < 10$), at least a muon chamber hit, muon segments in at least two muon stations, at least 10 hits in the tracker (including one in the inner pixel detector), and an impact parameter on the transverse plane not exceeding 2 mm with respect to the primary vertex. This selection rejects muons from in-flight decays, and is therefore used in the electroweak analyses, like this one on vector boson polarization. The loss in efficiency for prompt muons is of a few percent.

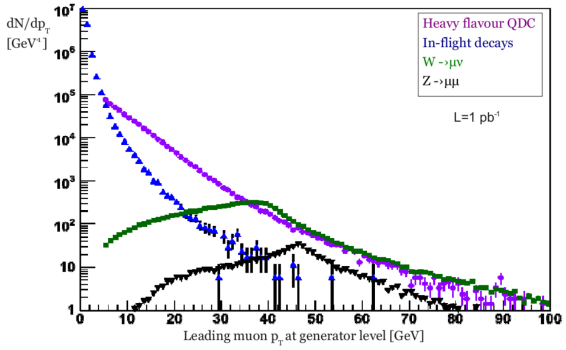

Figure 2.4: Muon spectrum for different production processes.

The number of muon stations with a segment matched to a tracker track is useful to reject muons from hadron punch-through, that are typically contained before the second station (Fig. 2.5). Also the impact parameter (and its significance) can be used to distinguish between prompt and heavy flavour muons (Fig. 2.6ab). The χ^2 of the track fit in the tracker looks different for muons from in-flight decay of light hadrons, being significantly higher than for prompt muons (Fig. 2.6c).

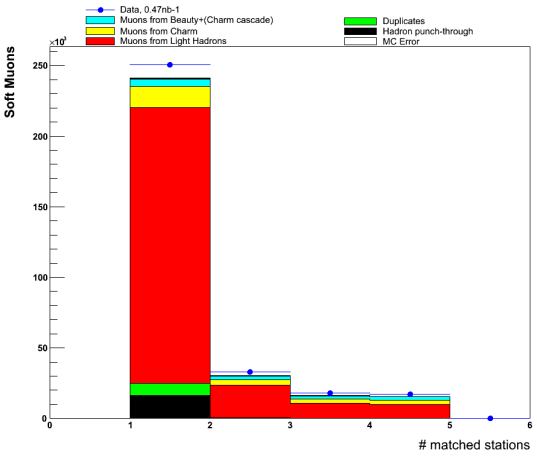

Figure 2.5: Comparison of data and simulation for distributions of Soft Muons in Zero-Bias events: number of muon stations with matched segments. [20]

The use of isolation variables deserves a more detailed discussion.

In principle, requiring that a muon is an isolated particle in the event selects those from decay of vector bosons, and rejects those from QCD processes, which tend to have a larger energy flow around them (Fig. 2.6d).

Two different concepts of isolation for muons are available at CMS:

- Tracker relative isolation (I^{rel}_{trk}): all tracks reconstructed in the silicon tracker within a 0.3

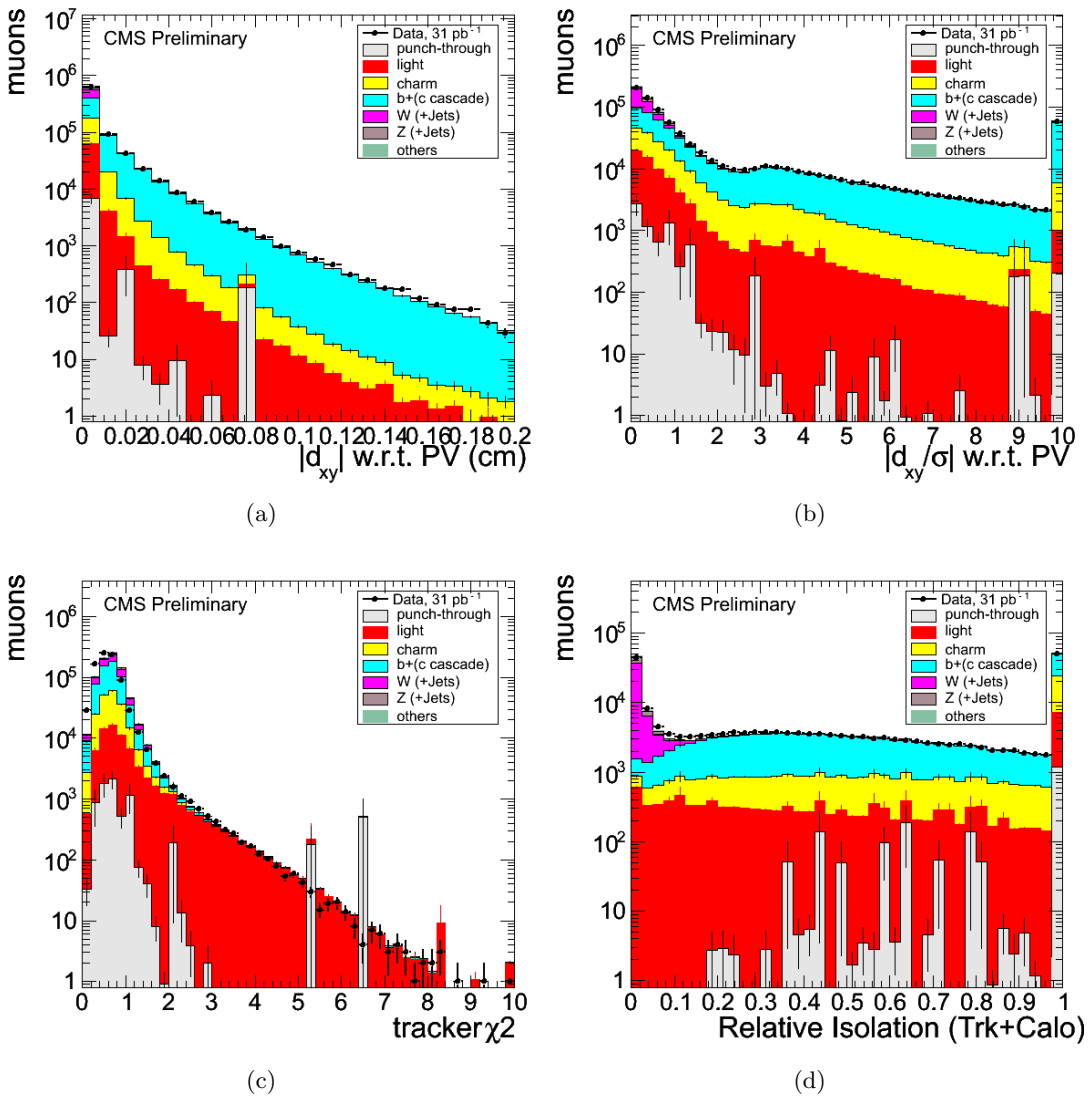

(a) (b)

(c) (d)

Figure 2.6: Identification variables for tight muons with $p_T > 20$ GeV/c : (a) transverse impact parameter; (b) significance of the transverse impact parameter; (c) normalized χ^2 of the fit of the track in the silicon tracker; (d) relative combined isolation (tracker+calorimeters), with a cone size $\Delta R = 0.3$. [20]

distance in the η-ϕ plane ($\Delta R = \sqrt{(\Delta\eta)^2 + (\Delta\phi)^2} < 0.3$), except that the muon track itself, are considered. The ratio of the scalar sum of their p_T and the muon track p_T has to be less than a certain threshold, typically set around 0.15.

- Tracker + Calorimetry combined relative isolation (I^{rel}_{comb}): the method is similar to the previous one, but the energy measured in the ECAL and HCAL calorimeters in the $\Delta R < 0.3$ cone is also added to the numerator of the discriminant ratio. Particular attention must be payed to correctly consider the energy radiated by high-energy muons themselves into the calorimeter in this case.

Each method fits better to specific situations. For EWK (muons from vector bosons) analyses the most common choice is the combined isolation.

The efficiency of these methods has been measured from data using the tag-and-probe method. The "tag" is required to be a tightly-identified muon with $I^{rel}_{comb} < 0.15$. The "probe" muons have to building up - together with the tag muon - an invariant mass comprised in a 40 GeV-wide window centered on the mass of the Z. In this way, it's possible to measure the isolation selections efficiency for muons from Z decay, with little contamination from the background [20].

The Lepton Kinematic Template (LKT) method is also used for the same purpose: the kinematic distribution of the muons is assumed to be unrelated to the underlying event activity, that determines the energy flow around the muon; therefore, the isolation cuts are tested around directions traced in space according to the angular distribution of the signal, in events with a similar underlying event activity (for instance, $Z \rightarrow \mu\mu$ events after subtraction of the reconstructed muons). Further information on this procedure can be found in the literature [20].

The efficiency of the isolation algorithms is shown in Fig. 2.7 for $20 < p_T < 50$ GeV muons, for different thresholds, and in Fig. 2.8, 2.9 as a function of the muon p_T . For typical values (threshold between 0.1 and 0.3), both methods and the MC simulation agree within 1%.

A QCD-enriched sample has been selected to study the rejection power of these selections. It has been required that only one tight muon between 20 and 50 GeV was reconstructed in the event, together with at least one Particle Flow (PF) [21] jet with $p_T > 30$ GeV, and a PF MET smaller than 20 GeV and at an angle smaller than 1.5 rad from the muon (to reject W+jets events).

The efficiency of isolation on Z muons is plotted versus the one for QCD muons in Fig. 2.10, and is found to be consistent with the MC simulation at the level of 1%.

The sensitivity of these algorithms to different pile-up conditions has also been studied. Pile-up introduces a non-negligible η dependence of the isolation efficiency (Fig. 2.11), as shown by the MC simulation.

Efficiency of muon selection

The efficiency of muon selections has been measured from data using the tag-and-probe method on muons from J/ψ and Z. The probes are tracks reconstructed in the inner silicon tracker, so the efficiencies are to be considered relative to the track efficiency, that is found to be at least 99% in the whole tracker acceptance, in agreement with the simulations. This also allows to avoid any bias due to the muon stations behaviour in the selection of the sample.

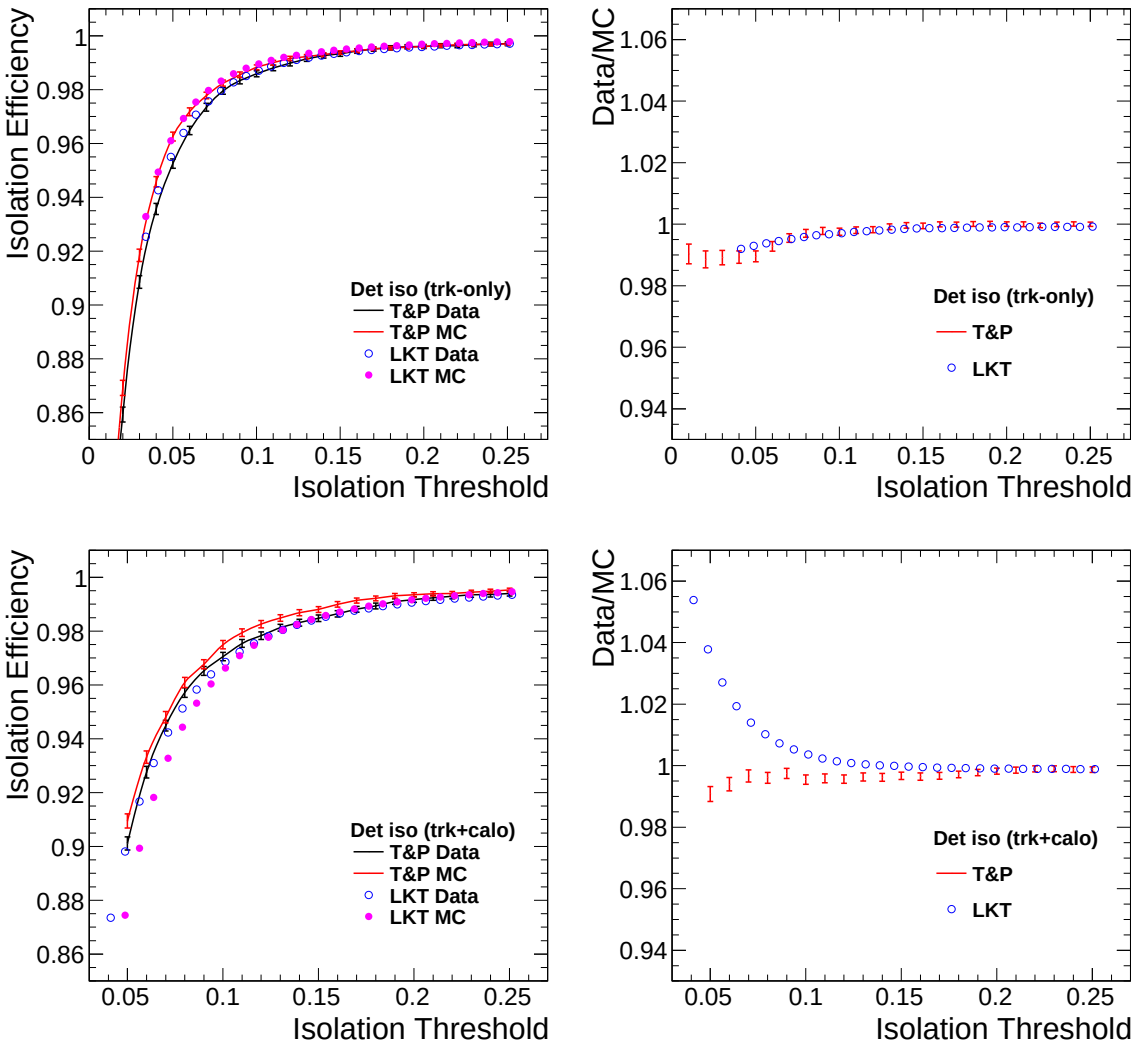

Figure 2.7: Efficiency of the isolation algorithms on muons from Z^0 decay, with $20 < p_T < 50$ GeV/c , as a function of the isolation variable threshold. Results are shown for both data and MC (with realistic pile-up conditions), using the tag-and-probe and the Lepton Kinematic Template (LKT) method [22]. Tracker relative I^{rel}_{trk} (top) and tracker plus calorimeters relative I^{rel}_{comb} (bottom) isolation are analyzed. [20]

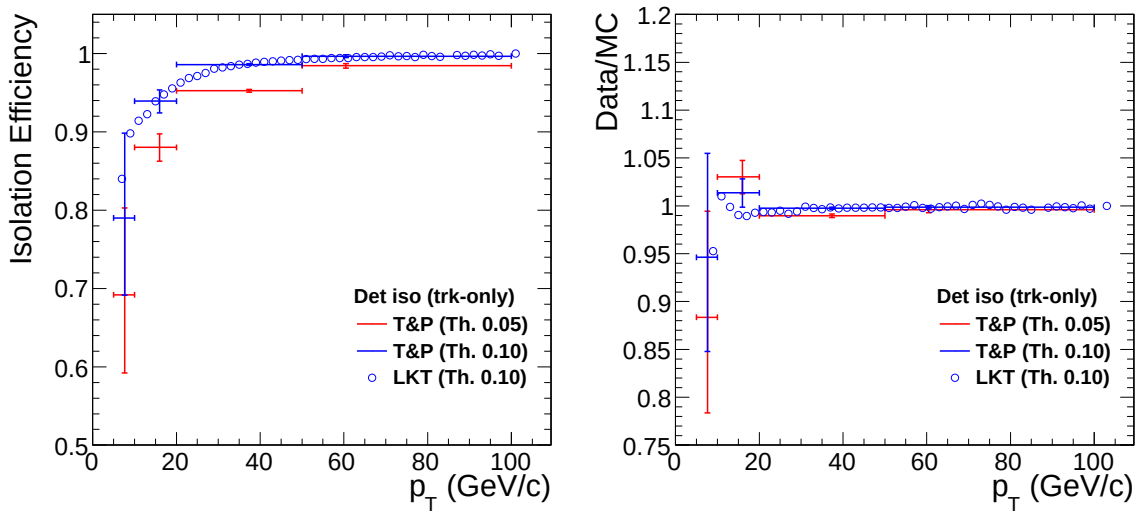

Figure 2.8: Tracker relative isolation I^{rel}_{trk}: efficiency measured on data (and compared to MC with realistic pile-up conditions) for selecting muons from Z^0 decay as a function of p_T, using the tag-and-probe and the LKT method, for different choices of the threshold value. [20]

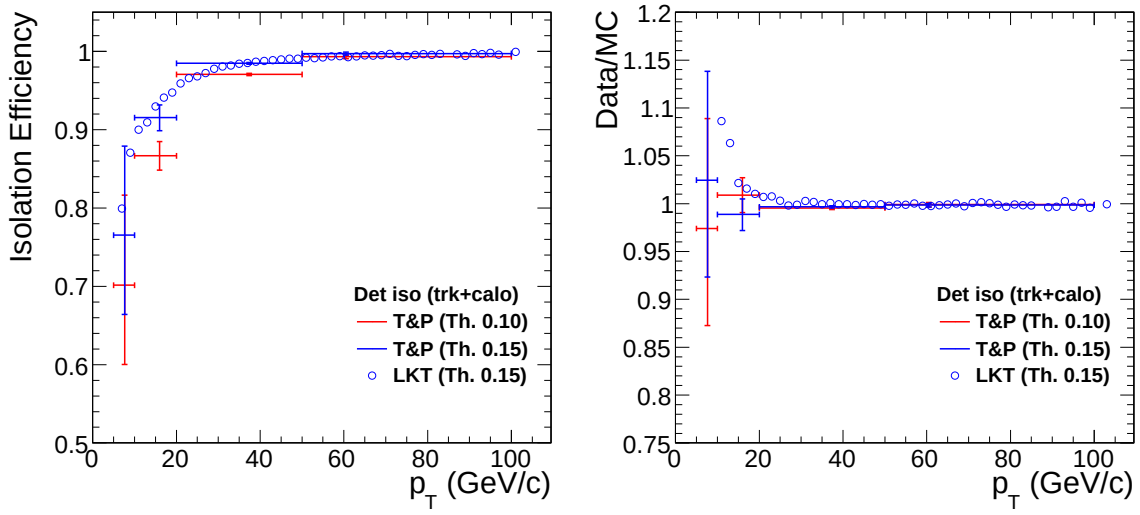

Figure 2.9: Tracker plus calorimeters relative isolation I^{rel}_{comb}: efficiency measured on data (and compared to MC with realistic pile-up conditions) for selecting muons from Z^0 decay as a function of p_T, using the tag-and-probe and the LKT method, for different choices of the threshold value. [20]

Fits of the invariant mass spectra of the tag and the probe muons allow to control the normalization of the combinatorial background from probe muons generated by charged hadrons, obtaining the true efficiency for resonance muons. This is important for the low-p_T J/ψ region, whereas for the Z the use of high-p_T single-muon triggers rejects the backgrounds effectively.

Fig. 2.12 and 2.13 show the results of this procedure. The agreement between data and

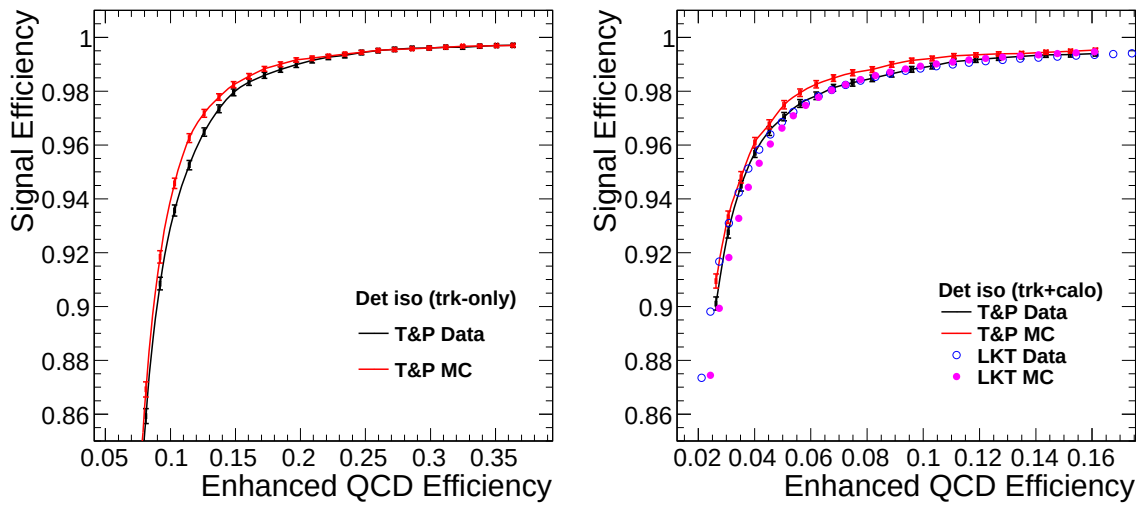

Figure 2.10: Isolation efficiency for muons from Z^0 decays versus the one for muons from the QCD enhanced dataset, with $20 < p_T < 50$ GeV/c , for the different algorithms. [20]

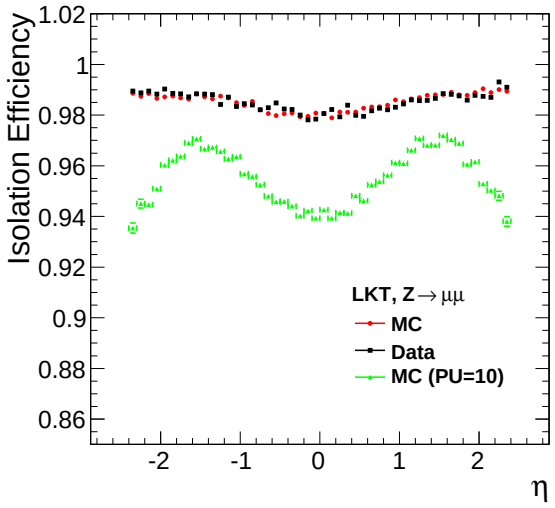

Figure 2.11: Isolation efficiency, obtained on data and MC for muons from Z^0 decays with $20 < p_T < 50$ GeV/c , versus η. Results from a MC simulation of events with 10 reconstructed primary vertices are also shown. [20]

simulation (see Table 2.1) is remarkable in the plateau region, which extends from approximately 10 GeV/c onwards for tight muons.

The impact of pile-up has been studied up to 6 vertices, and no loss in efficiency has been observed. The probability of identifying other particles as muons has also been studied, and is found to be consistent with the simulation (Fig. 2.14).

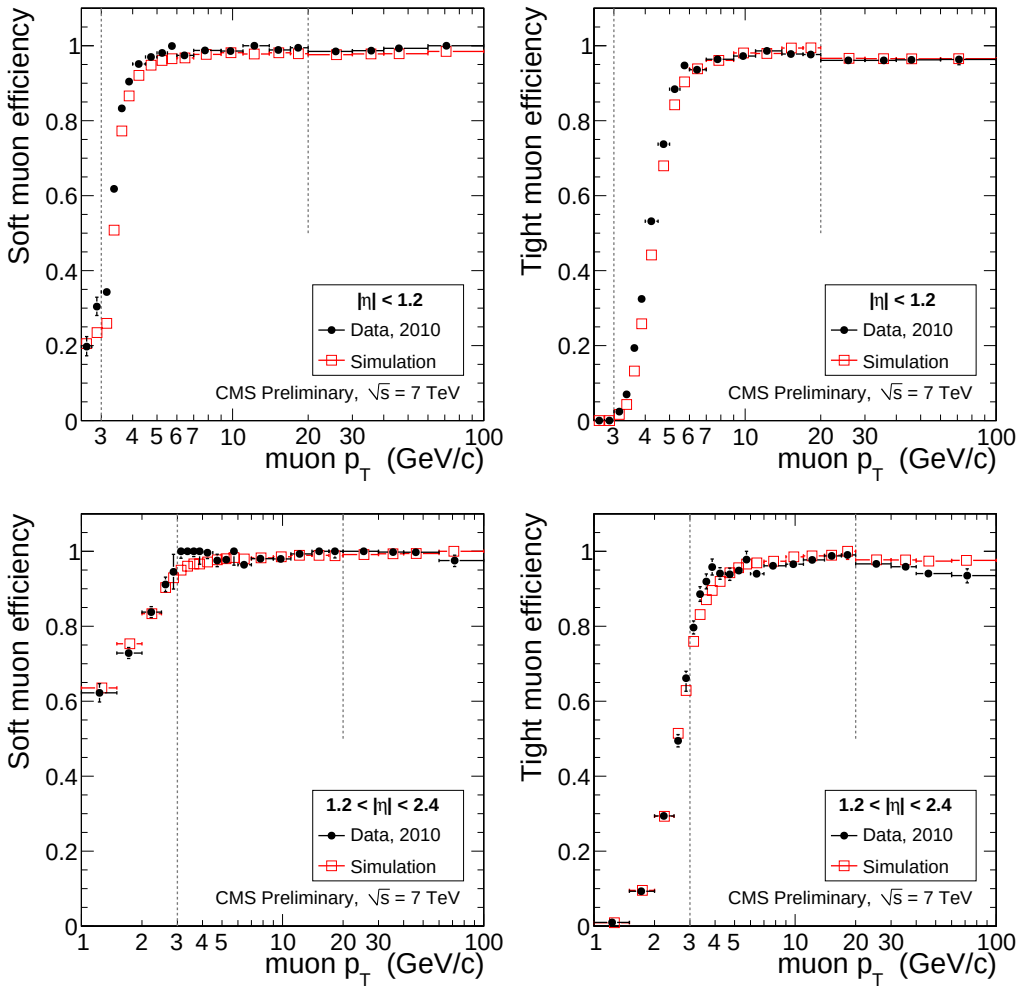

Figure 2.12: Tag-and-probe results for the muon selection efficiency in data compared to simulation, for Soft and Tight muons in different η regions. [20]

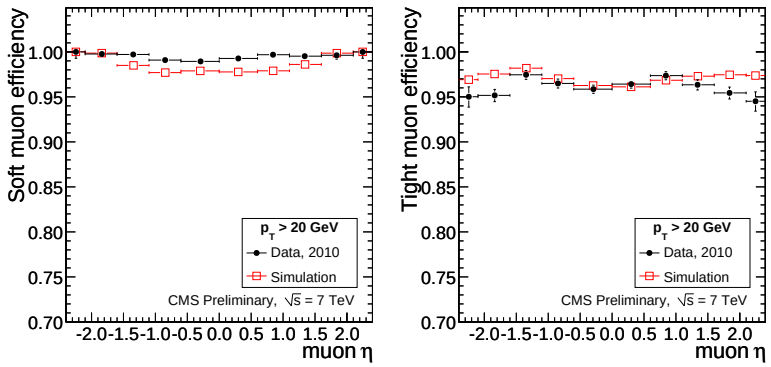

Figure 2.13: Tag-and-probe results for the muon selection efficiency in data, compared to simulation, for Z events as a function of η. [20]

Muon selection		J/ψ		Z	
	Region	Eff. [%]	Data/Sim. ratio	Eff. [%]	Data/Sim. ratio
Soft	$0.0 < \|\eta\| < 1.2$	$98.4^{+0.3}_{-0.3}$	$1.010 \pm 0.003 \pm 0.010$	$99.2^{+0.1}_{-0.1}$	$1.014 \pm 0.001 \pm 0.002$
	$1.2 < \|\eta\| < 2.4$	$98.0^{+0.7}_{-0.7}$	$1.002 \pm 0.007 \pm 0.014$	$99.9^{+0.1}_{-0.2}$	$1.005 \pm 0.002 \pm 0.004$
Tight	$0.0 < \|\eta\| < 1.2$	$98.4^{+0.3}_{-0.3}$	$0.998 \pm 0.004 \pm 0.010$	$96.4^{+0.2}_{-0.2}$	$0.999 \pm 0.002 \pm 0.002$
	$1.2 < \|\eta\| < 2.4$	$96.8^{+0.7}_{-0.7}$	$0.979 \pm 0.007 \pm 0.014$	$96.0^{+0.3}_{-0.3}$	$0.983 \pm 0.003 \pm 0.004$

Table 2.1: Muon selection efficiencies (in the plateau region): result of measurement on data and ratio between it and the expected value from simulation (± stat. ± syst.). [20]

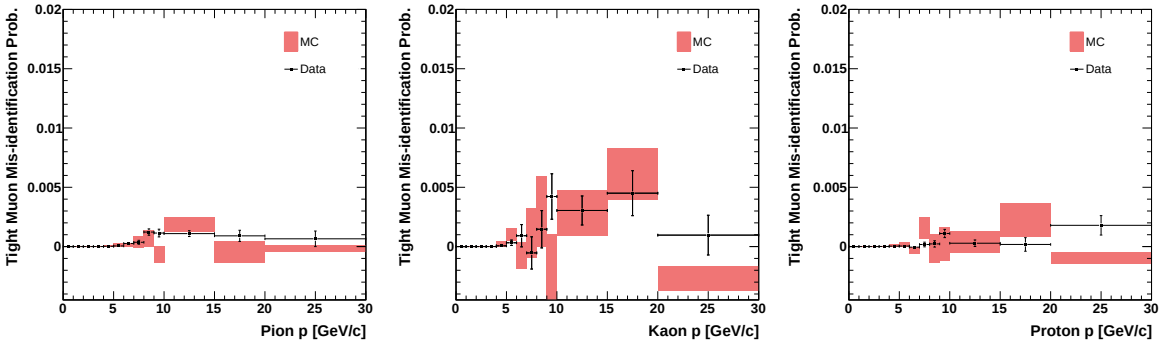

Figure 2.14: Fraction of π, K, and protons that are mis-identified as a Tight muons as a function of p, compared to the simulation. [20]

2.2.3 Muon triggers

The Level-1 muon trigger combines the information of the muon systems (DT, CSC and RPC) and, by applying a first selection based on track quality and p_T estimate, reduces the rate of candidates to a few kHz. Afterwards, the High Level Trigger (HLT) uses the L1 objects to seed the reconstruction of standalone muons, and improves the measurement of p_T . At this stage, different thresholds in p_T can be applied (leading to Level-2 muons), before using the standalone muon information to seed a track reconstruction in the inner silicon detector. If a match is found, the object qualifies as a Level-3 muon and a final p_T cut is applied. The final rate of recorded muon events is of order tens of Hz [18].

The efficiency of muon triggers, relative to the efficiency of reconstructing a soft/tight muon, has been measured with the tag-and-probe technique on di-muon resonances (Table 2.2). All results are close to the MC simulation. Tight muons from Z exhibit a very high L1+HLT efficiency, especially in the barrel region (Fig. 2.15 and 2.16).

It's also possible to introduce isolation criteria already at the HLT level. Using once again the tag-and-probe with the Z, their efficiency (with respect to the non-isolated muon trigger) has been measured. Typical choices for the isolation thresholds are 3 GeV for absolute quantities,

Trigger Level		Tag-and-Probe J/ψ	
	Region	Eff. [%]	Data/MC
L1	Overall	97.1 ± 0.2	0.990 ± 0.002
	Barrel	99.2 ± 0.1	0.995 ± 0.001
	Endcap	94.5 ± 0.3	0.978 ± 0.004
HLT	Overall	99.1 ± 0.2	0.995 ± 0.002
	Barrel	99.2 ± 0.2	0.993 ± 0.002
	Endcap	99.0 ± 0.3	0.997 ± 0.004
L1*HLT	Overall	96.2 ± 0.2	0.985 ± 0.003
	Barrel	98.5 ± 0.2	0.989 ± 0.002
	Endcap	93.6 ± 0.5	0.975 ± 0.005

Table 2.2: Average trigger efficiency for Soft muons in the p_T range $(9-20)$GeV/c for different pseudorapidity regions. [20]

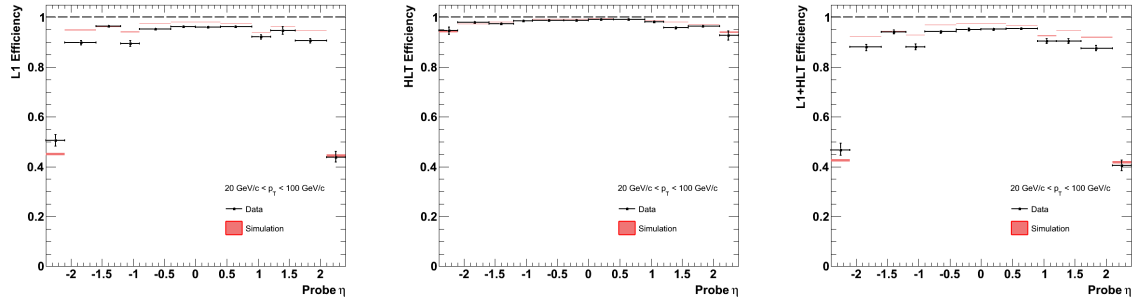

(a) (b) (c)

Figure 2.15: Single-muon trigger efficiencies for Tight muons, as a function of η: a) L1 with $p_T > 7$ GeV/c , b) HLT with L3 $p_T > 15$ GeV/c , c) L1+HLT. [20]

and 0.15 for relative ones. The agreement between data and simulation is very good (Fig. 2.17).

Measuring trigger efficiency for single muons reconstructed offline, in samples collected with non-muon triggers, allows to extend the p_T region far away from the resonances that are needed by tag-and-probe, and to avoid potential effects due to correlations between the two muons. The results are in Table 2.3 and Fig. 2.18, and are consistent with the previous ones.

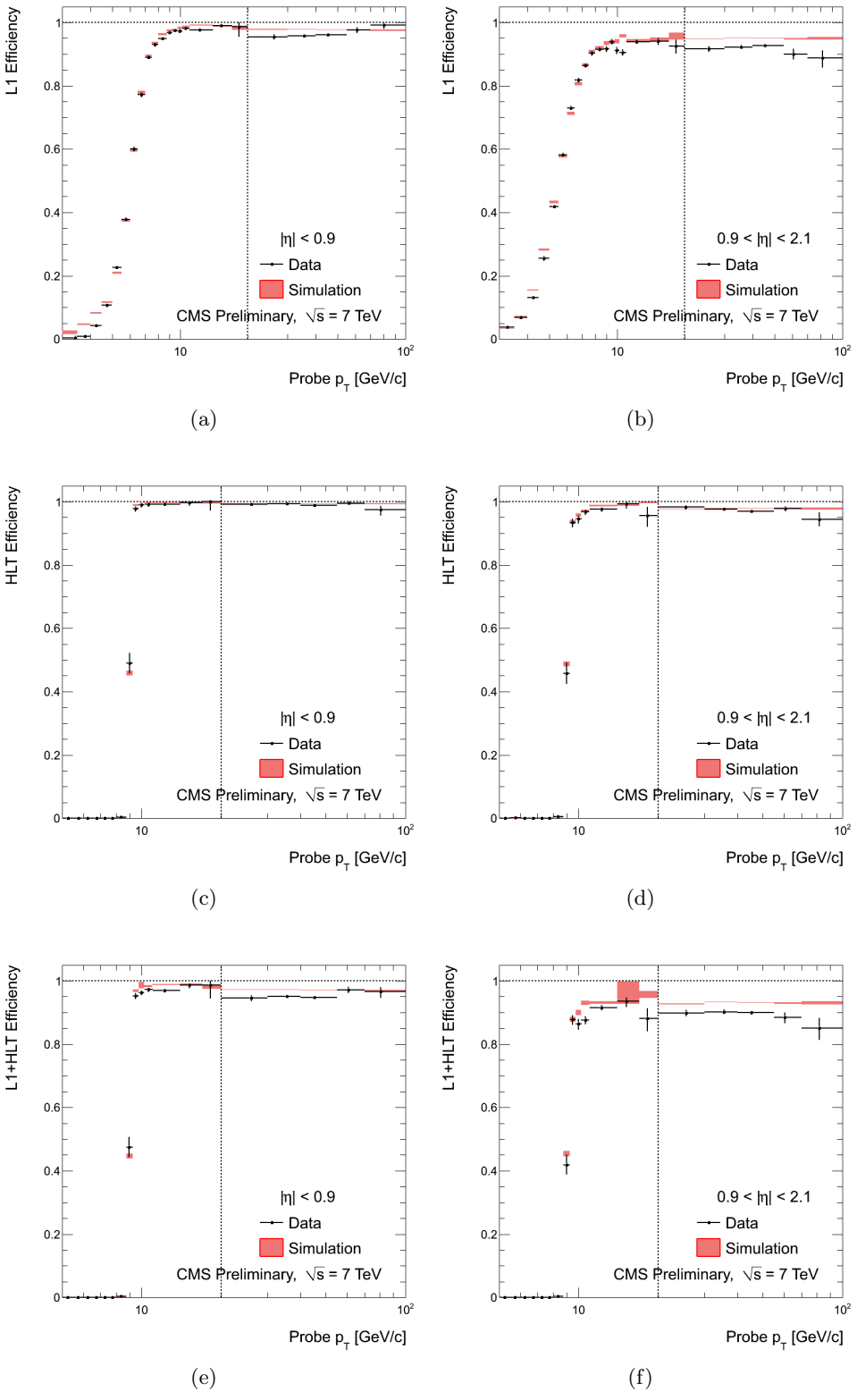

Figure 2.16: Single-muon trigger efficiencies for Tight muons, as a function of p_T in the barrel and overlap-endcap regions: a) L1 with $p_T > 7$ GeV/c , b) HLT with L3 $p_T > 9$ GeV/c , c) L1+HLT. [20]

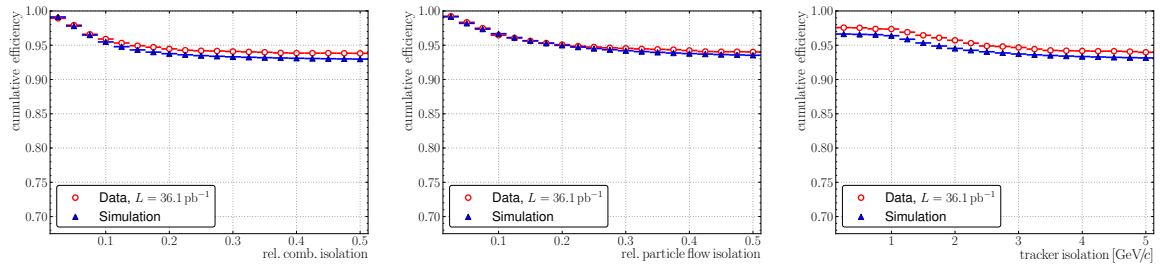

(a) (b) (c)

Figure 2.17: Single-muon isolated trigger efficiencies (trigger thresholds are 3 GeV for absolute, 0.15 for relative quantities), for offline Tight muons, as a function of the isolation threshold applied to the offline reconstruction. [20]

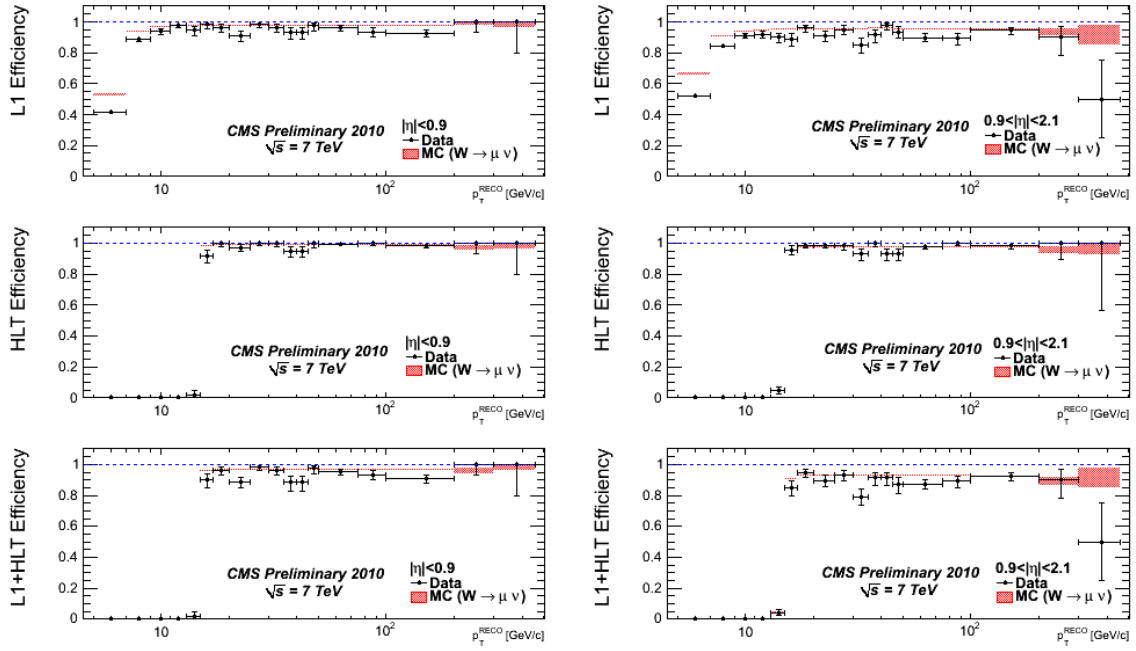

Figure 2.18: Single-muon trigger efficiencies for Tight muons passing the isolation cut, as a function of p_T : a) L1 with $p_T > 7$ GeV/c , b) HLT with L3 $p_T > 9$ GeV/c , c) L1+HLT. [20]

Trigger Level	Tag & Probe Z		single Isolated μ	
Region	Eff. [%]	Data/MC	Eff. [%]	Data/MC
L1				
Overall	94.1 ± 0.2	0.976 ± 0.002	92.9 ± 0.8	0.962 ± 0.008
Barrel	95.9 ± 0.2	0.981 ± 0.002	94.7 ± 1.0	0.971 ± 0.010
Endcap	92.3 ± 0.3	0.971 ± 0.004	91.1 ± 1.2	0.952 ± 0.013
HLT				
Overall	98.2 ± 0.1	0.995 ± 0.001	97.8 ± 0.5	0.995 ± 0.005
Barrel	99.0 ± 0.1	0.996 ± 0.001	98.6 ± 0.5	0.992 ± 0.005
Endcap	97.4 ± 0.2	0.995 ± 0.002	97.1 ± 0.8	0.997 ± 0.008
L1*HLT				
Overall	92.4 ± 0.3	0.971 ± 0.003	90.8 ± 0.9	0.958 ± 0.009
Barrel	95.0 ± 0.3	0.977 ± 0.003	93.3 ± 1.1	0.963 ± 0.011
Endcap	89.9 ± 0.4	0.965 ± 0.004	88.5 ± 1.4	0.949 ± 0.015

Table 2.3: Summary of trigger efficiencies for Tight Muons in different η region, averaged over the $(20 - 100)$ GeV/c p_T range. [20]

2.2.4 Study of muon momentum scale

The measurement of the transverse momentum of muons is very sensitive to the precise alignment of the elements of the silicon tracker, of the muon chambers, and to the description of the magnetic field and the material distribution in the detector volume used by the reconstruction algorithm.

These effects introduce biases with that depend differently on the muon momentum:

- an incorrect description of $\vec{B}$ yields a constant $\frac{dp}{p}$;
- material effects (energy loss) give a $\frac{dp}{p} \propto \frac{1}{p}$ contribution;
- misalignment introduces a $\frac{dp}{p} \propto p$ bias.

Therefore, the muon p_T scale is studied with different tecniques in different kinematic regimes.

At low p_T , the mass constraint of the J/ψ resonance can be used for calibration; alignment effects are not very important here, and imprecisions in the material model and the magnetic field description dominate. The data show that the overall bias due to tracker measurement of muons in the 1-10 GeV/c range is of order 0.1%, and the p_T resolution lies between 0.8% and 3%, in agreement with the simulation [20].

At very high p_T , on the other hand, a variety of methods using cosmic muons have been used [20].

At intermediate p_T (in the range 10-100 GeV/c), which is the most interesting region for this analysis, the resolution is still good (a few percent), but the alignment effects can bias the muon p_T scale significantly. In this regime, the Z invariant mass is the most important handle to correct for these effects.

The study of single track fitting performance does not help to correct the so-called "weak modes" or "χ^2 invariant modes", that are peculiar modes of distorsion of the tracker elements that do not affect the χ^2 of the fitted track.

Typical examples of such modes are twists over ϕ or over z, that change the sagitta without scattering the tracker hits away from a possible trajectory (Fig. 2.19), or displacements of tracking layers in the transverse plane, that introduce biases sinusoidally dependent on ϕ [23].

Two methods of correction have been studied in the Collaboration (see [20] for a more detailed description):

- MuScleFit method: the mass distribution of the Z is studied as a function of muon kinematics (for instance, in bins of ϕ). A voigtian (lorentzian convoluted with a gaussian

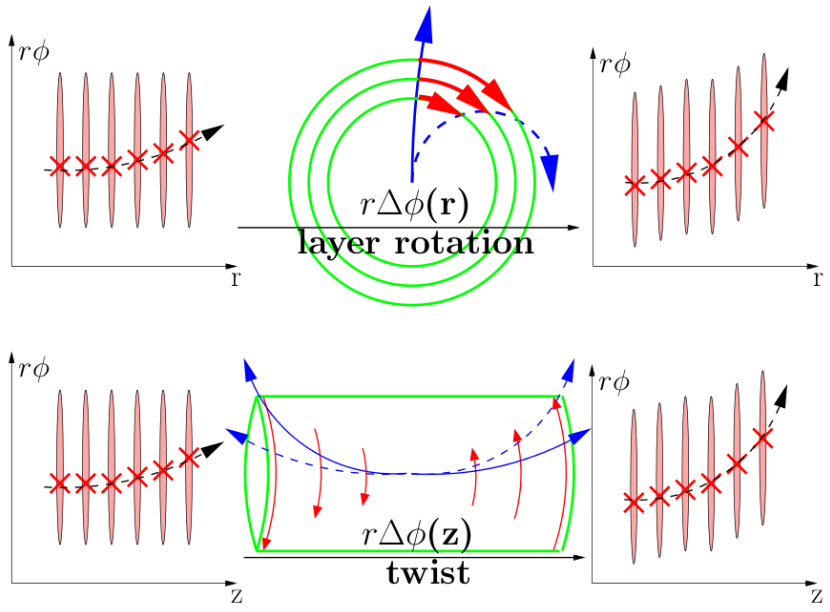

Figure 2.19: Examples of tracker weak modes of misalignment. [24]

to account for detector resolution) fit is done in each bin, and the dependence of the peak value[1] is studied to determine an ansatz function for muon p_T correction.

For example, the shape observed in Fig. 2.20 suggests a simple correction of the following form:

$$p_T^{'} = p_T(1 + a \cdot q_\mu \cdot p_T \cdot \sin(\phi + b))$$

The parameters appearing in the correction function (amplitude a and phase b in this case) are found with a likelihood fit with a reference model where no dependence of the reconstructed Z mass on the muon kinematics exists.

The complexity of the ansatz - and, consequently, the number of parameters to fit for - can be adjusted as long as the statistics accumulated are enough for fits with several degrees of freedom.

- SIDRA method: the Z mass resonance shape that should be observed in data if no misalignment effects were present is first obtained from simulation; then, parameters that appear in a correction function (similarly to the MuScleFit case) are determined through a fit to the resonance shape.

For the W/Z polarization measurement, misalignment can have an important effect on the final results. It's therefore important to correct both the data and the MC simulation (that

[1]Note that the expected mean value for the Z mass peak is *not* expected to be the PDG value of the Z mass. This happens because the Z resonance is not symmetric with respect to the peak: it exhibits, already at the generator level, a larger tail for lower values due to radiation. If detector resolution is now introduced, the peak moves to lower mass. The expected value is approximately 90.8 GeV.

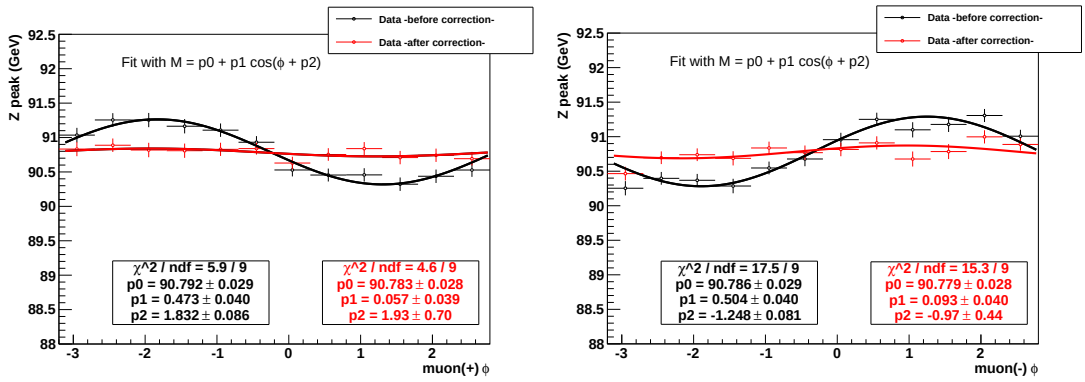

(a) (b)

Figure 2.20: Z peak as a function of μ^+ and μ^- in data, before and after MuScleFit correction. [20]

includes a realistic misalignment scenario as well, but in general different from the one observed in data).

A simple version of the MuScleFit method (that by default includes many parameters) has been used in this analysis for calibrating the momentum scale, that for the Z measurement is a source of systematic uncertainty.

It should be noted that such effects can change dramatically with the version of the reconstruction program used for the analysis, since a new version may include an "improved" configuration of the alignment. The following plots refer to a specific version, but similar results apply to all versions used for the analysis.

First of all, $Z \to \mu\mu$ events have been separated in two samples, according to the charge of the muon with larger p_T ; then, the reconstructed Z mass has been fitted with a voigtian function in bins of ϕ and η of the leading muon.

The results show (Fig. 2.21) an important sinusoidal bias in ϕ, and also a strong dependence on η. In both cases, the effect is charge asymmetric, and affects the muon p_T by approximately 1% at 100 GeV/c .

In order to derive the correct form of the correction function for muon p_T , let's consider how the reconstructed invariant mass is changed - at the leading order - by a correction on the muon p_T scale:

$$M_{\mu\mu} = \sqrt{(p_1 + p_2)^2 - (\vec{p}_1 + \vec{p}_2)^2} = \sqrt{2p_1p_2(1 - \hat{p}_1 \cdot \hat{p}_2)} \tag{2.1}$$

$$\frac{\partial M_{\mu\mu}}{\partial p_i} = \frac{1}{2\sqrt{2p_1p_2(1 - \hat{p}_1 \cdot \hat{p}_2)}} \frac{2p_1p_2(1 - \hat{p}_1 \cdot \hat{p}_2)}{p_i} = \frac{M_{\mu\mu}}{2p_i} \tag{2.2}$$

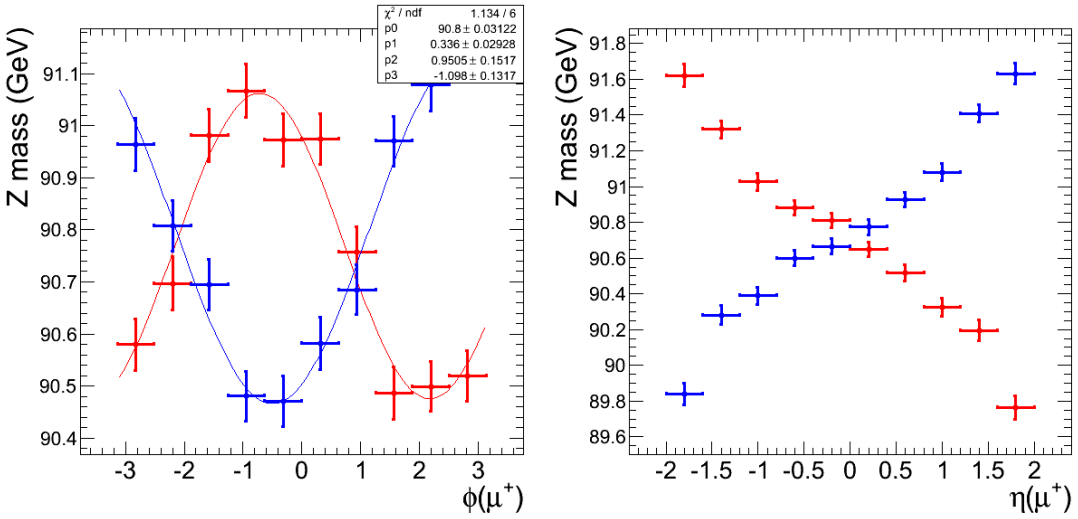

(a) (b)

Figure 2.21: Z peak as a function of μ^+ (red) and μ^- (blue) ϕ and η in data.

$$\Delta M_{\mu\mu} \approx \frac{M}{2}\left(\frac{\Delta p_1}{p_1} + \frac{\Delta p_2}{p_2}\right) \tag{2.3}$$

The form of correction applied to the muon p_T translates into the reconstructed Z mass; therefore, the following ansatz has been chosen as a compromise between accurate description of the shapes observed and limited number of parameters:

$$\frac{\Delta p_T}{p_T} = q_\mu \cdot p_T \cdot (\alpha + \beta \sin(\phi + \gamma) + \delta_{1,2} \cdot \eta) \tag{2.4}$$

where the parameters are α, β, γ, δ_1 (that applies for $|\eta| < 1$) and δ_2 (for $|\eta| > 1$).

The parameters have been estimated through a maximum likelihood fit, and the procedure repeated to verify that the bias is removed within the statistical uncertainty. The method proves to be very effective (Fig. 2.22).

The misalignment programmed in the detector simulation can be corrected in the same way. Once again, the dependence of Z mass on muon (η, ϕ) is cancelled within the statistical uncertainty (Fig. 2.23).

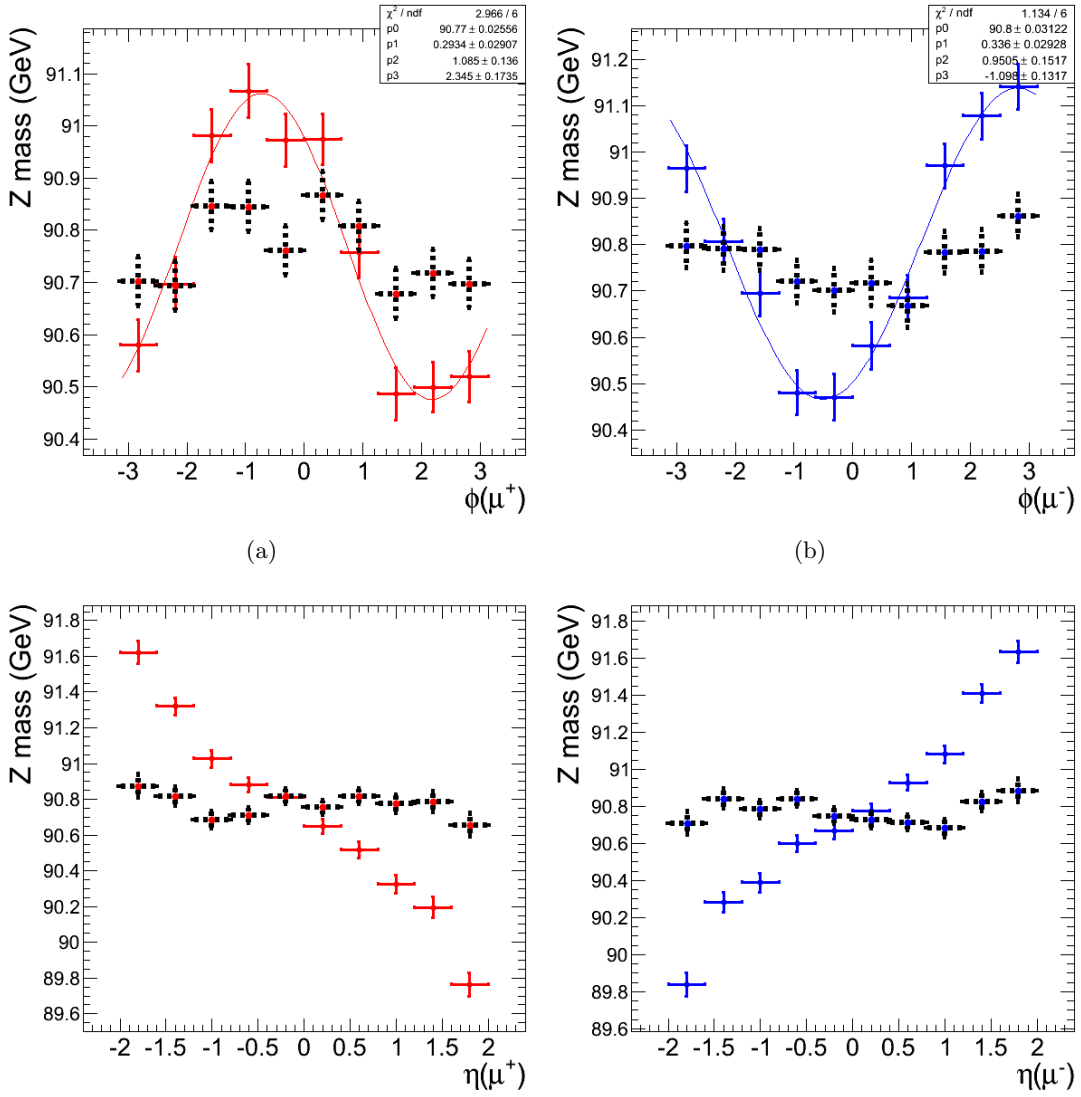

Figure 2.22: Z peak as a function of μ^+ (red) and μ^- (blue) ϕ and η in data, before and after (black) correction.

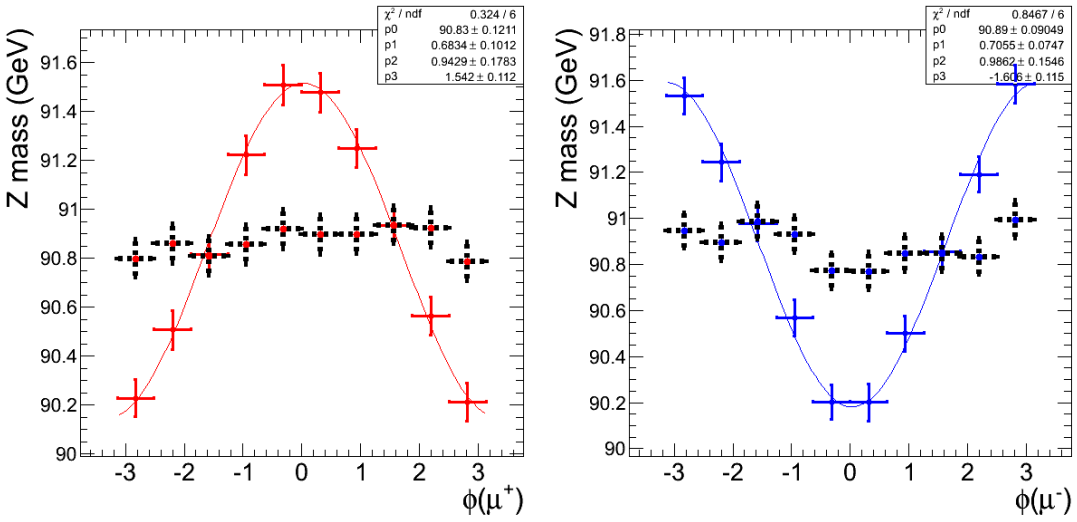

(a) (b)

Figure 2.23: Z peak as a function of μ^+ (red) and μ^- (blue) ϕ in the MC simulation, before and after (black) correction.

2.3 Electrons

Electrons have a much less distinguishable signature than muons in the detector; in the analysis, the rejection power of electron cuts is not as good as in the muon channel, and this causes a significant contamination of angular distributions from the QCD background.

Therefore, it's important to fully understand the issues in electron reconstruction and selection, and validate such contributions in the MC simulation.

2.3.1 Reconstruction

The relevant subdetectors for electron reconstruction [18, 19, 25] are the inner silicon tracker and the electromagnetic crystal calorimeter (ECAL). Both of them provide a very good energy resolution and a high granularity.

Similarly to the case of muons, there are two different approaches to build up a reconstruction algorithm for electrons:

- Tracker seeding: the track is fitted starting from the tracker hits, and afterwards the calorimeter information is added; this method gives the best results for low-p_T electrons inside jets. Afterwards, some quality checks based on a multivariate analysis [21] are introduced to have a first selection of candidates.
- ECAL-driven seeding: first of all, one reconstructs an ECAL SuperCluster (SC), that is a group of clusters of energy deposits in the calorimeter [18]. At this stage, the information of the characteristic width in η and ϕ (the second one, dependent also on the bending of the track due to the magnetic field) of the electron cluster is taken into account. Then, the supercluster position is used to make a match to tracker seeds, and at the end the global fit is performed, using an appropriate modelling of energy loss in the tracker material (not negligible for electrons). This method is the recommended one for electrons in a higher p_T range, like those coming from W or Z decays.

The efficiency of electron reconstruction has been measured from $Z \to ee$ data with the tag-and-probe technique. The "tag" electron is required to pass a tight identification procedure and to come from an isolated supercluster with $E_T > 20$ GeV; the probes are all superclusters with $E_T > 20$ GeV that build up, together with the tag, an invariant mass close to the Z mass. A first measurement gives a $(99.3 \pm 1.4)\%$ efficiency in the barrel, and $(96.8 \pm 3.4)\%$ in the endcaps, close to the MC expectation (resp. 98.5% and 96.1%).

Moreover, a method based on W transverse mass fit [25] has been used to determine electron reconstruction efficiency from data. A W-enriched sample has been selected requiring a supercluster with $E_T > 20$ GeV in the barrel, with isolation and shower shape cuts, no jets with $E_T > 25$ GeV, and $\not{E}_T / E_T^{SC} > 0.3$. A fit to the transverse mass spectrum gives the signal and background yields, from which the efficiencies can be calculated (Fig. 2.24).

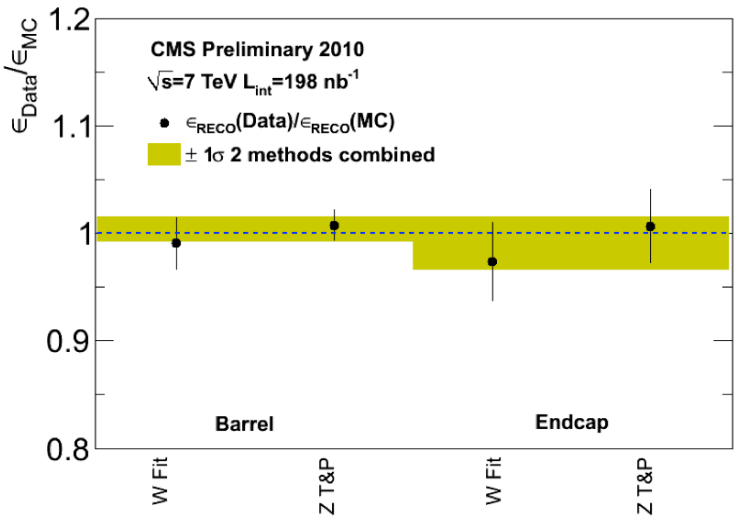

Figure 2.24: Ratio of the measured electron reconstruction efficiency over the expected efficiency from simulation, for both tag-and-probe with $Z \rightarrow ee$ events and transverse mass fit on W events, for barrel and endcap. [25]

2.3.2 Identification and selection

Electron selection is based on three cathegories of variables:

- Identification variables: these are characteristic quantities of tracks and superclusters from electrons. They include the ratio between the SC energy and the track momentum, the spatial distance between the SC and the track ($\Delta\eta_{in}$, $\Delta\phi_{in}$), the SC η width $\sigma_{i\eta i\eta}$ (not dependent on the curvature due to the magnetic field, that affects particle's trajectories only on the transverse plane), the H/E ratio (fraction of energy that leaks into the hadronic calorimeter, typically very small for isolated electrons due to the large amount of interaction lenghts of the calorimeter).

- Isolation variables: several sums of transverse energies in a $\Delta R < 0.3$ cone are considered, using information from the tracker, ECAL and HCAL.

- Conversion variables: dedicated algorithms exists at CMS to identify electrons that come from conversions in the tracker material. For example, such electrons are expected to have a large impact parameter with respect to the interaction point, to exhibit tracks with missing hits in the first tracker layers, and to have a partner with opposite charge and intersecting tracks.

Examples of distributions of these variables, in a sample of minimum bias events, are in Fig. 2.25 and 2.26.

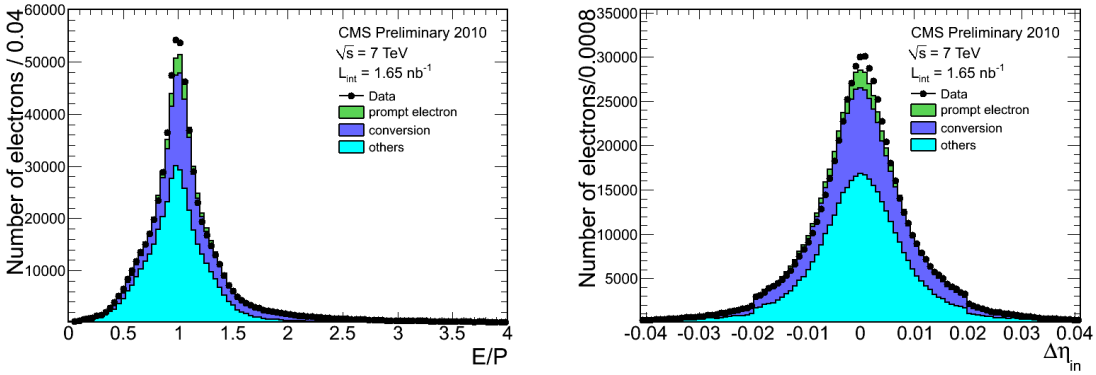

(a) (b)

Figure 2.25: Distributions of electron candidate track-cluster matching variables in minimum bias events: (a) ratio E/p between the supercluster energy and the track momentum; (b) difference $\Delta\eta_{in}$ between the supercluster position and the track extrapolation from the innermost measurement. [25]

	ECAL barrel			ECAL endcaps		
Selection	Efficiency data	Error (stat.+syst.)	Efficiency MC	Efficiency data	Error (stat.+syst.)	Efficiency MC
WP95%	92.5%	3.2%	95.4%	86.4%	6.7%	92.9%
WP80%	77.5%	4.7%	85.1%	75.1%	8.6%	76.2%
Cic Loose	96.4%	2.1%	97.0%	94.1%	4.7%	95.3%
Cic SuperTight	89.3%	3.4%	89.3%	85.5%	6.5%	79.4%

Table 2.4: Electron selection efficiency from tag-and-probe and W transverse mass fit methods. [25]

Several standard cut-based selections have been prepared, with different nominal efficiency for prompt electrons with $E_T > 20$ GeV (these are called "WP95", "WP80",etc.). Moreover, another approach ("category-based") exists based on the amount of brehmsstrahlung measured in the tracker between its innermost and outermost layers, and the ratio between the SC energy and the track momentum. All thresholds are optimized separately in the barrel and in the endcaps.

These efficiencies have been measured in data with the same tag-and-probe method on Z events and W MT fit described above. The results agree with the MC simulation (Fig. 2.27 and Table 2.4).

A sample highly enriched in QCD electron candidates has been analyzed requiring a jet with $E_T > 20$ GeV in the event, with low H/E ratio, and a MET not greater than 30 GeV, to reject W events (Fig. 2.29).

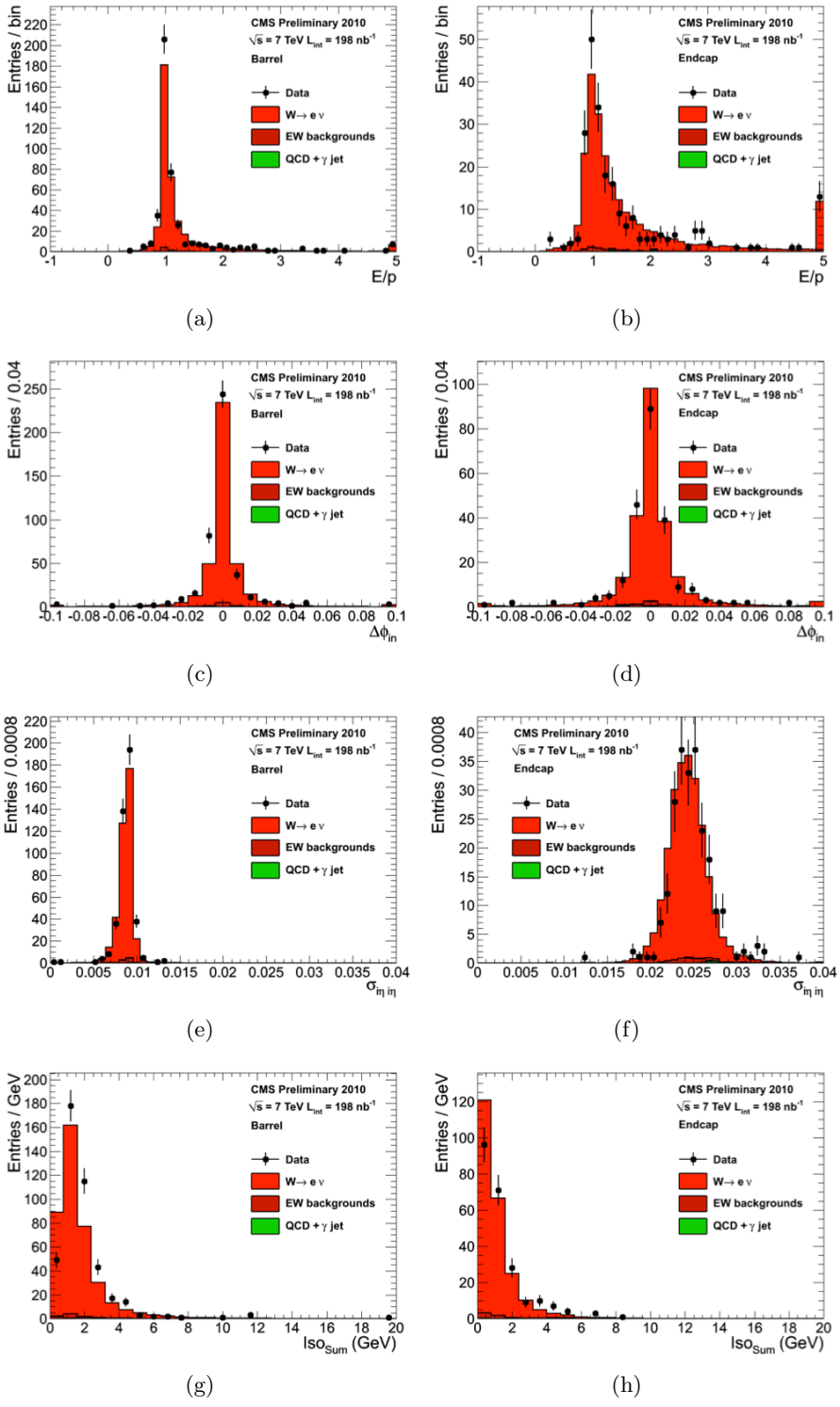

Figure 2.26: Distribution of electron ID variables for electron candidates from W events: (a,b) E/p_{in}, (c,d) $\Delta\phi_{in}$, (e,f) $\sigma_{i\eta i\eta}$, and (g,h) isolation sum, separately for barrel and endcap. [25]

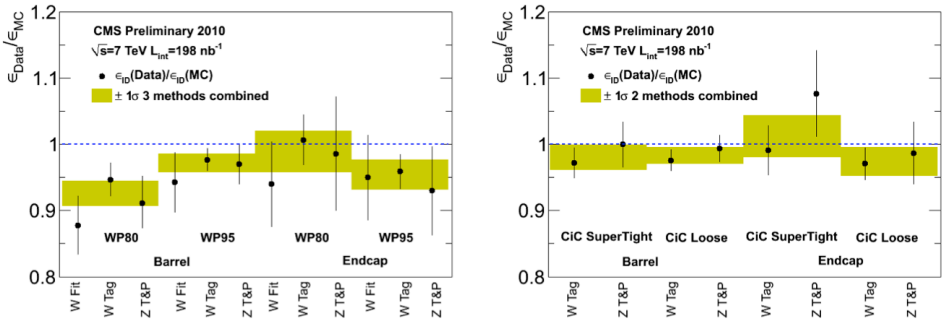

(a) (b)

Figure 2.27: Ratio of the measured electron selection efficiency over the expected efficiency from simulation for (a) the cut-based selections; (b) the category based selections. The values are shown, separately for barrel and endcap, for both the tag-and-probe and the transverse mass fit methods. [25]

The distribution of isolation and cluster-shape variables look strikingly different with respect to the case of isolated electrons.

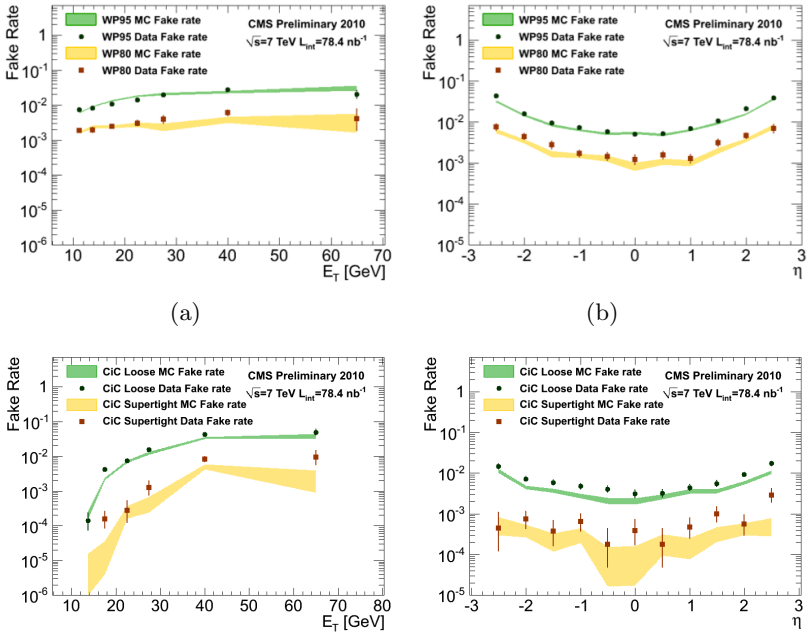

(a) (b)

(c) (d)

Figure 2.28: Electron fake rate per reconstructed electron candidate as a function of (a) E_T and (b) η for the WP95 and WP80 electron selections (resp. "Cic Loose" and "Cic SuperTight") in data and simulation. [25]

The fake rate (i.e., the fraction of background electrons passing a given ID selection) is reported in Fig. 2.28.

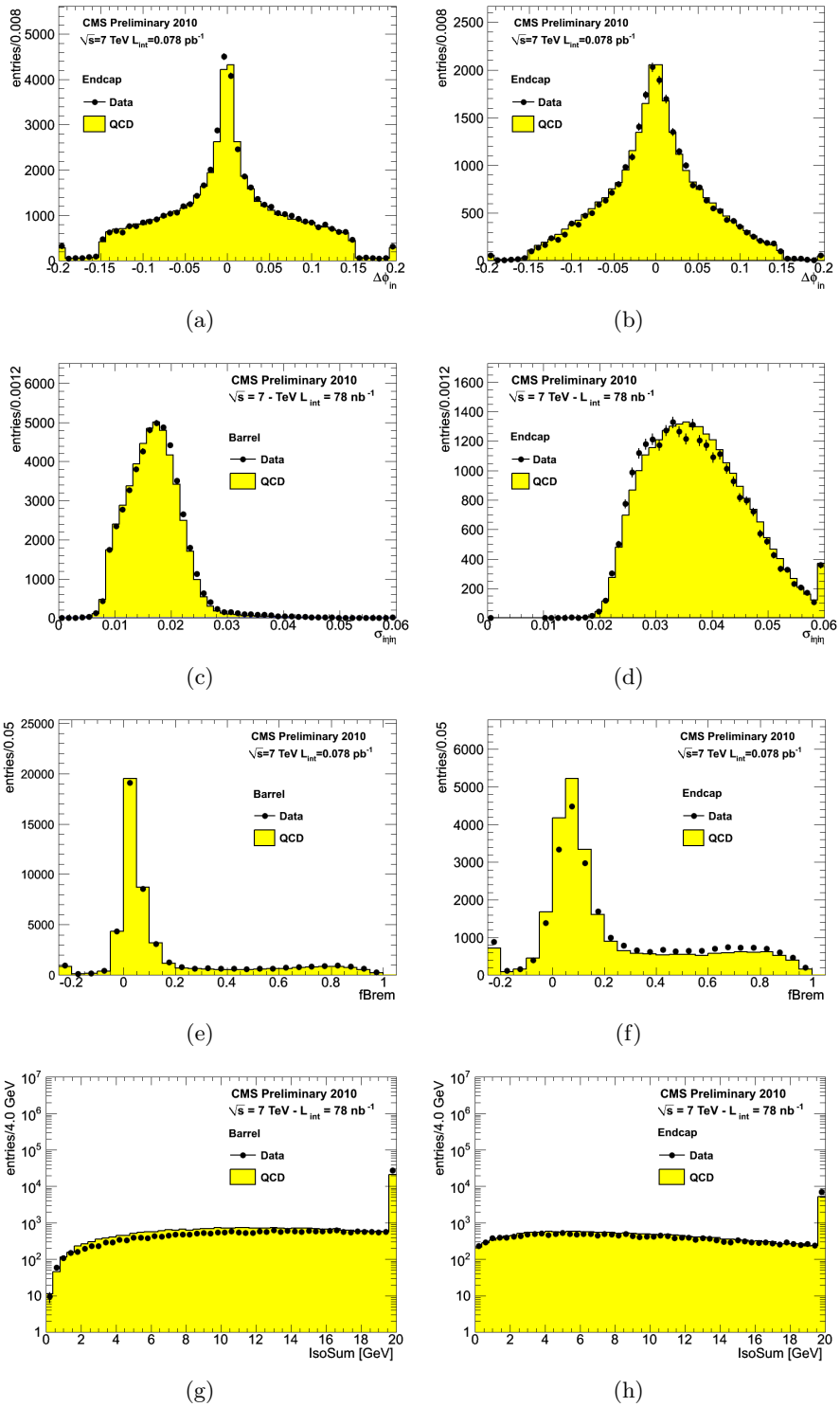

Figure 2.29: Distribution of electron ID variables for background electron candidates from di-jet events in data compared with the MC simulation: (a,b) $\Delta\phi_{in}$, (c,d) $\sigma_{i\eta i\eta}$, (e,f) fraction of energy lost for brehmsstrahlung and (g,h) isolation sum, separately for barrel and endcap. [25]

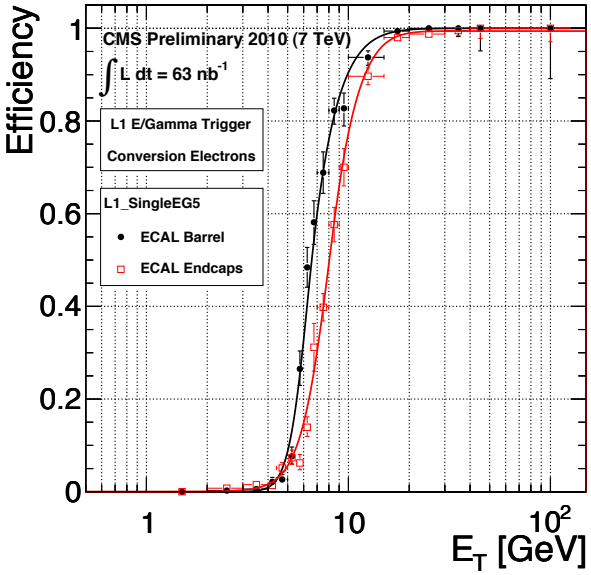

Figure 2.30: Level-1 EG5 trigger efficiency for electron candidates from minimum bias data as a function of the supercluster E_T for barrel and endcap. [25]

2.3.3 Trigger

The electron HLT software uses the information of L1 triggers, which are based on local deposits of energy in the electromagnetic calorimeter, and therefore are a suitable choice for both electron and photon candidates.

Basically, the transverse energy deposit in a 3x3 window of ECAL towers, centered on the most energetic hit, is passed, together with isolation information, to the HLT, that makes the final decision, discriminating between electron and photons: for electrons both a reconstructed supercluster, matching with the L1 candidate and above a certain E_T threshold, and a compatible pixel hit are required.

In other words, at the HLT level the electron selection takes place among the photon candidates. Further details can be found in [18].

The efficiency of both L1 and HLT relevant triggers (L1_SingleEG and HLT_Ele) has been measured from minimum bias data samples, with respect to offline reconstructed electrons (Fig. 2.30 and 2.31).

The L1 efficiency is very close to 1 at energies interesting for electroweak analyses; the HLT photon path is also very efficient, because it doesn't actually require much more than the L1 (except that the energy of the supercluster is used as a threshold). The electron HLT step high efficiency, in any case, indicates a very effective pixel matching, even in online conditions.

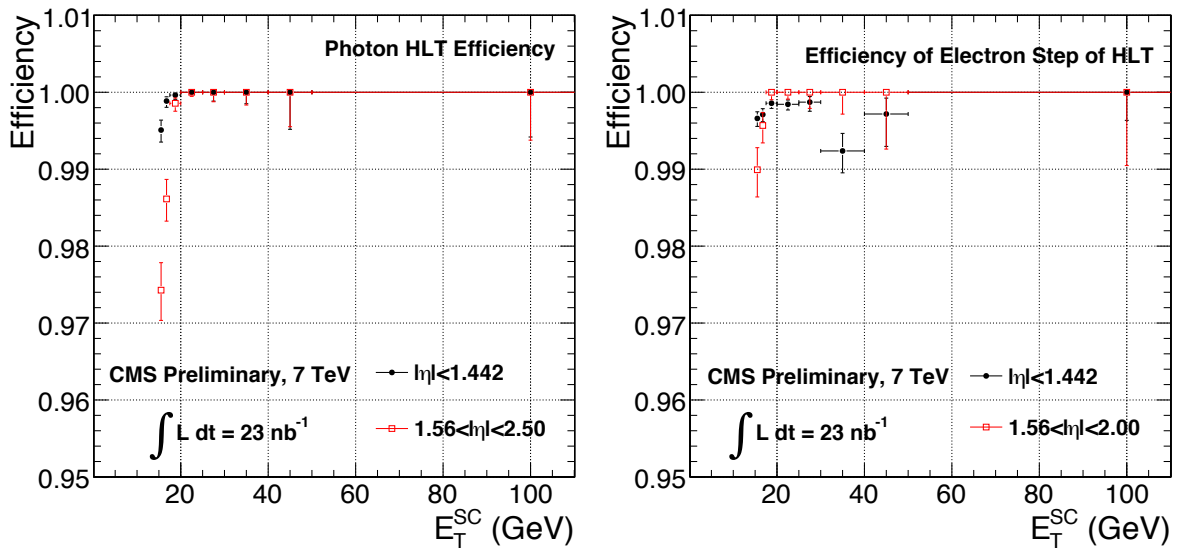

(a) (b)

Figure 2.31: Efficiencies of HLT photon/electron triggers: (a) HLT_Photon15 efficiency for an offline reconstructed electron matched to a L1_SingleEG5 candidate as a function of E_T , and (b) the HLT_Ele15LW efficiency for an offline reconstructed electron which passes HLT_Photon15. [25]

2.4 Missing transverse energy

Missing transverse energy (MET, $\not\!\!E_T$) is defined as the opposite of the vector sum of transverse momenta of all the final-state particles reconstructed in the event:

$$\not\!\!E_T = -\sum p_T$$

Its presence can be due not only to neutral weakly interacting particles that cannot be detected (such as neutrinos, or BSM objects like SUSY or quasi-stable particles), but also to mis-measurements and mis-identification of observable particles, as well as instrumental effects like malfunctions and imperfect coverage of the whole acceptance region.

Details of physics objects definitions do affect the MET performance; they can be found in [18, 19, 26].

In the interest of this analysis, understanding the MET scale and resolution is crucial, because this is the dominant source of uncertainty on the W p_T , on a event-by-event basis.

Let's now focus on the concepts useful for understanding MET performance, and on the results that have been observed in 2010 data.

2.4.1 Reconstruction

There are three different MET reconstruction algorithms at CMS:

- Calo $\not\!\!E_T$: based only on energies measured by the calorimeters, and their geometry; all calorimeter towers above a certain noise-suppression threshold are examined; each of these towers is considered a massless pseudo-particle, and included in the calculation. Muon deposits in the calorimeter are subtracted and replaced by the global p_T measurement.

- TC $\not\!\!E_T$: Calo $\not\!\!E_T$ corrected using additional information from the inner silicon tracker, and taking into account the expected energy release in the calorimeters, according to simulations (in bins of p_T and η) of single hadron deposits. Very high-p_T tracks (above 100 GeV) are not considered because they're already well measured by the calorimeters; other compensations are applied for very low-p_T tracks (under 2 GeV).

- Particle-Flow (PF) $\not\!\!E_T$: simply calculated from final-state particles reconstructed with the Particle-Flow algorithm [21]. This is a peculiar approach to event reconstruction: the information of all subdetectors is combined - with optimized routines - to identify and reconstruct every final-state particle in the event, and then build up complex objects like jets and missing E_T .

The $\not\!\!E_T$ can be mismeasured for different reasons: for instance, non-linearity in calorimeter response for hadrons, effect of thresholds, noise-suppressions and inefficiencies in both tracking and calorimetry.

Moreover, the Calo $\not\!\!E_T$ is sensitive to the uncorrect assignment of direction to particles hitting the calorimeter far from their initial line of flight, because of the bending induced by the strong magnetic field.

Corrections exist to limit some of these effects: first of all, the contribution from jets and unclustered energy is separated from the deposits of isolated electrons, muons and photons, which are assumed not to require any correction. Then, jets are corrected ("type-I" correction, applied to Calo $\not\!\!E_T$ and PF $\not\!\!E_T$) using the jet energy correction method [27]. The impact is larger for Calo $\not\!\!E_T$ than for PF $\not\!\!E_T$.

In the end, soft jets and unclustered energy deposits are corrected ("type-II correction") with dedicated factors [28].

2.4.2 Instrumental effects degrading $\not\!\!E_T$ performance

Several instrumental effects can affect negatively the performance of $\not\!\!E_T$ reconstruction, causing tails of events with large $\not\!\!E_T$. Since many important BSM theories predict excesses of events with such large $\not\!\!E_T$, it's crucial to keep these machine-induced backgrounds under control.

For instance, it can happen that protons of the beam undergo collisions in the tunnel upstream the detector; this results in muons ("beam halo") crossing the detector in coincidence with the beam crossing along the beam direction, without coming from the central interaction region. These muons are unlikely to fire the muon triggers, but can lead to an increased $\not\!\!E_T$ measurement if they release their energy in the calorimeters.

The CSC subdetector can be used to identify and reject these events. Actually, its geometry allows it to effectively reconstruct also non-collision muons interacting in the calorimeters (a particle flying along the beam must hit the endcaps CSC to reach the calorimeters). This allows to quantify the probability of finding a beam-halo event in a standard muon-triggered sample, and to observe the contribution of such events to the $\not\!\!E_T$ distribution, for different triggers (Fig. 2.32a). As expected, triggers that depend on the amount of energy released in the detector (like jets, E_T or $\not\!\!E_T$ triggers) are most affected (Fig. 2.32b).

Another important source of large $\not\!\!E_T$ tails are anomalous signals from the ECAL and HCAL readout electronics.

Several diferent effects have been observed [29, 30]; they range from direct ionization of avalanche photodiodes installed in the ECAL barrel, to scintillation and Cherenkov light in the quartz fibers and photomultipliers in the HF, to electronic noise affecting multiple channels at once in the HCAL.

In most cases, these signals exhibit a very unusual distribution of signal among neighbouring channels or in the depth direction, or peculiar pulse shape and timing. These behaviours are used, in each case, to reduce their contribution (Fig. 2.33), by excluding them from the

$\not\!\!E_T$ sum or by passing the information to higher-level software routines.

Finally, one has to remember that also non-instrumented (e.g. the "cracks" between different sections of the calorimeter) or non-functioning regions of the detector can lead to $\not\!\!E_T$ mis-measurement. Their contribution has been studied in [26].

2.4.3 MET scale and resolution

Calibration and resolution

The performance of $\not\!\!E_T$ at CMS has been studied [26] in events where an identified Z boson or an isolated photon are present.

Even if there is no genuine $\not\!\!E_T$ in such events, the vector boson can be artificially removed from the final-state particles, and then its $\vec{p}_T$ be compared to the reconstructed $\not\!\!E_T$, to measure both $\not\!\!E_T$ scale and resolution. Being the recoil activity of hadronic type mainly, the impact of jet energy scale and correction will be the most important.

The direction of flight of the γ/Z boson defines an axis $\hat{q}_T$ for each event; the hadronic recoil (that's the opposite of $\not\!\!E_T$) transverse momentum can be decomposed in two components, parallel ($u_\parallel$) and perpendicular ($u_\perp$) with respect to this axis (Fig. 2.34).

The mean value of the quantity $< u_\parallel > /q_t$ ("response") determines the correction factor needed for $\not\!\!E_T$ in events like these (Fig. 2.35); the resolution is measured from the RMS of $u_\parallel$ and $u_\perp$, after the scale correction (Fig. 2.36).

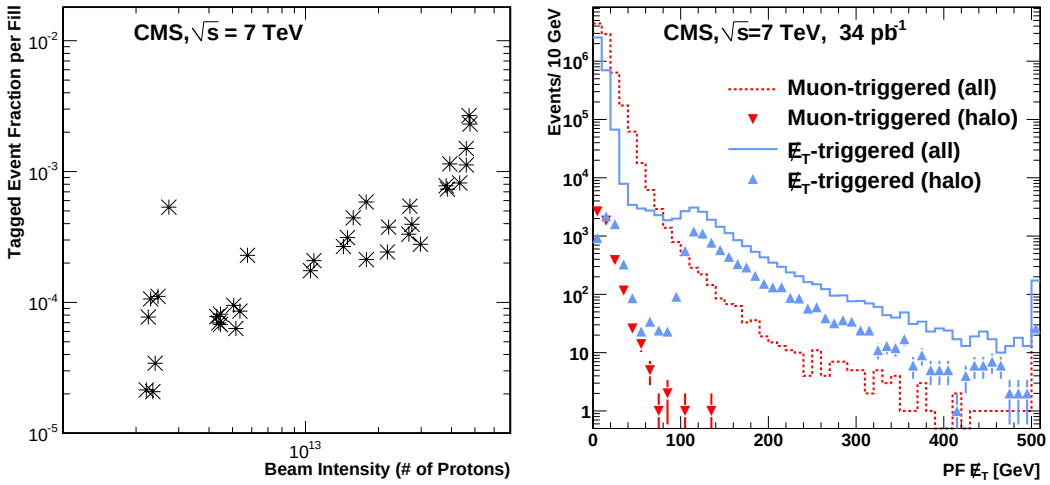

(a) (b)

Figure 2.32: (a) Probability of finding a beam-halo tagged event in muon-triggered events, as a function of the beam intensity. (b) PF$\not\!\!E_T$ distribution for all the events from muon and Calo $\not\!\!E_T$ triggers (not renormalized). Shapes are affected by trigger thresholds. [26]

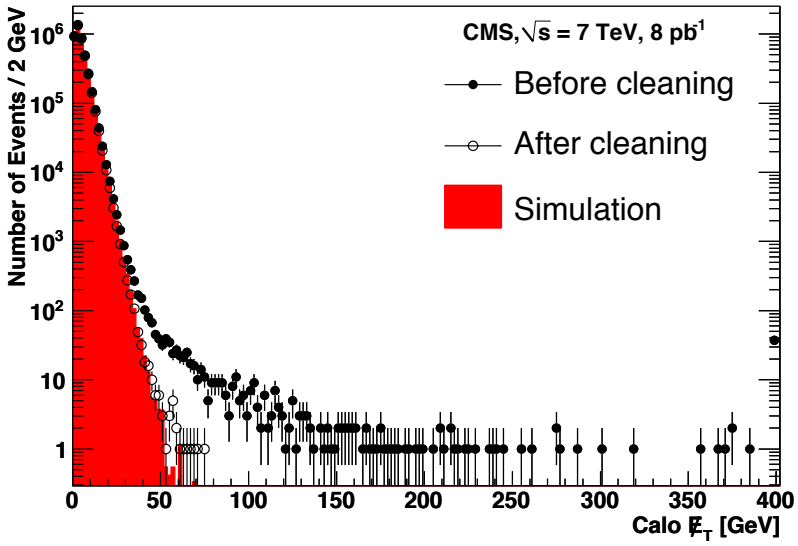

Figure 2.33: Calo $\not\!\!E_T$ distributions in a minimum bias data sample, without (black dots) and with (open circles) removal of anomalous energies. [26]

The response is larger than 1 for Calo $\not\!\!E_T$, because the type-I corrections are calculated on a sample with different quark to gluon jets ratio; smaller than 1 for TC $\not\!\!E_T$, that misses both type-I and type-II corrections; approximately 1 for PF $\not\!\!E_T$, excluding the low-q_T region that is affected by the missing type-II corrections.

The data/MC comparison indicates slightly worse resolution in data than expected.

Another method uses multijet events to measure the $\not\!\!E_T$ resolution, because in such events the expected value of $\not\!\!E_T$ is zero, and therefore the observed $\not\!\!E_T$ is due only to resolution effects.

As already observed, the PFMET gives the lowest resolution, which is still around 10% worse than in the simulation (Fig. 2.37). For this reason, this algorithm has been chosen to evaluate MET in the vector boson polarization analysis. Let's now evaluate the performance in a situation with a true missing energy, like a $W \to l\nu$ event.

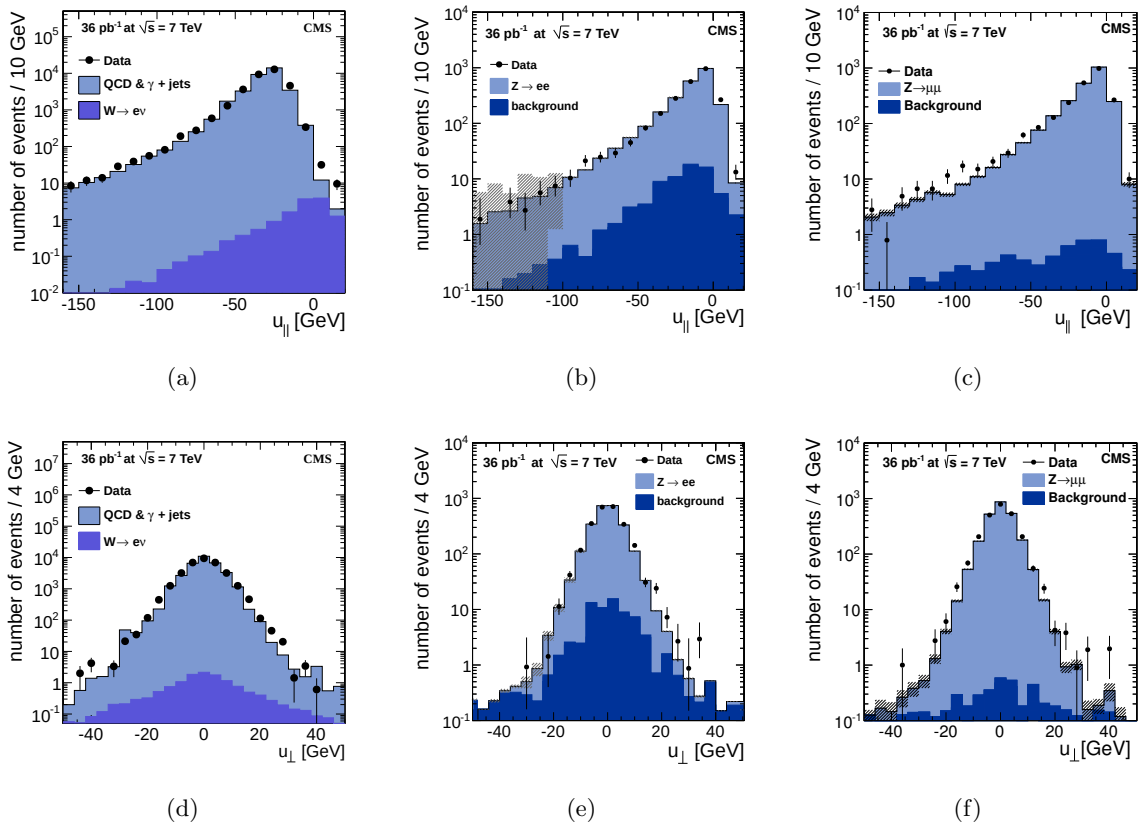

Figure 2.34: $u_{\parallel}$ and $u_{\perp}$ distributions for γ, $Z \to ee$, and $Z \to \mu\mu$ events with one reconstructed primary vertex. [26]

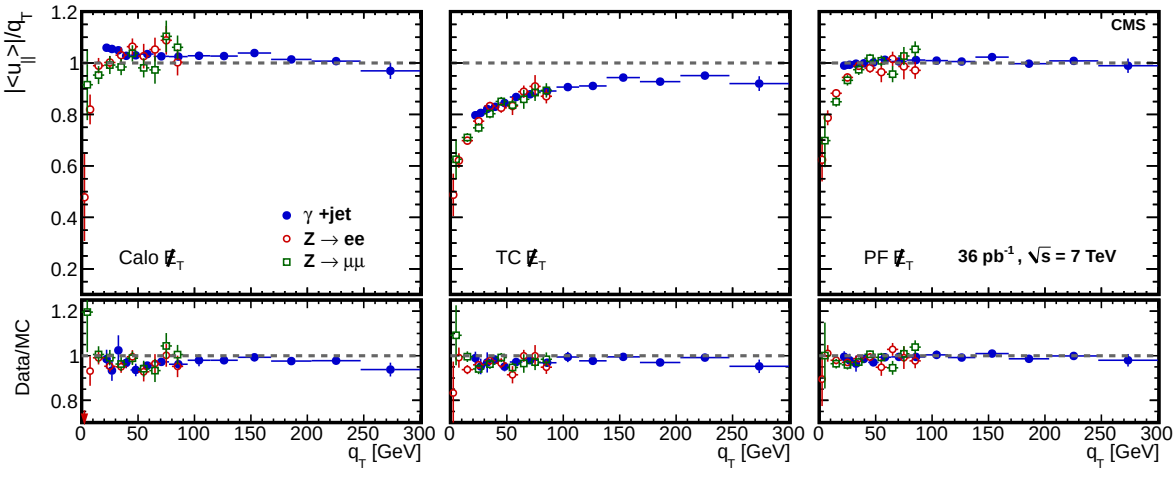

Figure 2.35: Response curves for events with one primary vertex, for (a) Calo $\not\!\!E_T$, (b) TC $\not\!\!E_T$, and (c) PF $\not\!\!E_T$, in different samples. [26]

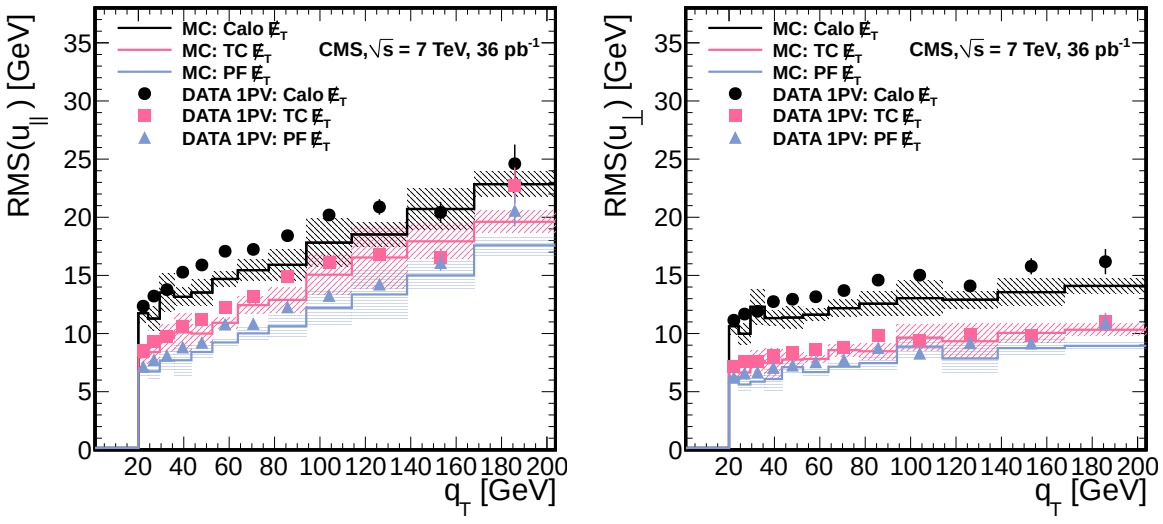

(a) (b)

Figure 2.36: Resolution curves for components of hadronic recoil, measured in photon events with one primary vertex. [26]

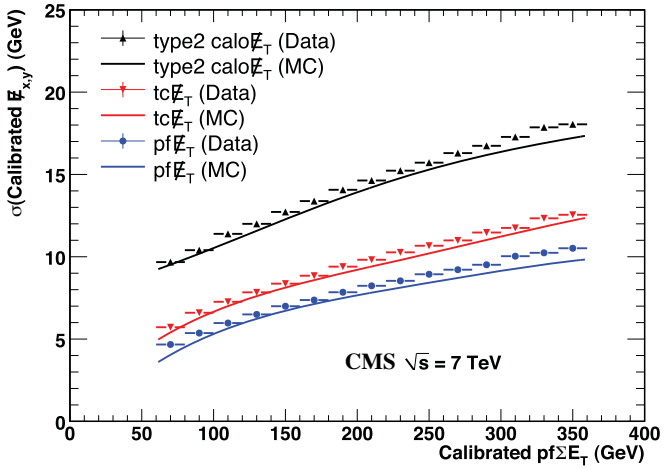

Figure 2.37: Calibrated $\not\!\!E_{x,y}$ resolution versus calibrated PF $\sum E_T$ for Calo $\not\!\!E_T$, TC $\not\!\!E_T$ and PF $\not\!\!E_T$ in a multijet data sample and in simulation. [26]

Events with genuine $\not\!\!E_T$

The performance of $\not\!\!E_T$ reconstruction has also been studied in events with true $\not\!\!E_T$, such as the $W \to (e, \mu)\nu$ decays. The lepton is measured with good resolution, so the $\not\!\!E_T$ resolution is - once again - dominated by the hadronic recoil.

A W-enriched sample has been selected requiring a muon (resp. electron) with $p_T > 25$ (resp. 20) GeV/c , applying a Z mass veto on other leptons in the event, and requiring $M_T > 50$ GeV and $\not\!\!E_T > 25$ GeV to reject the QCD background (Fig. 2.38).

The PFMET distribution is reported in Fig. 2.39 and is correctly described by the MC simulation.

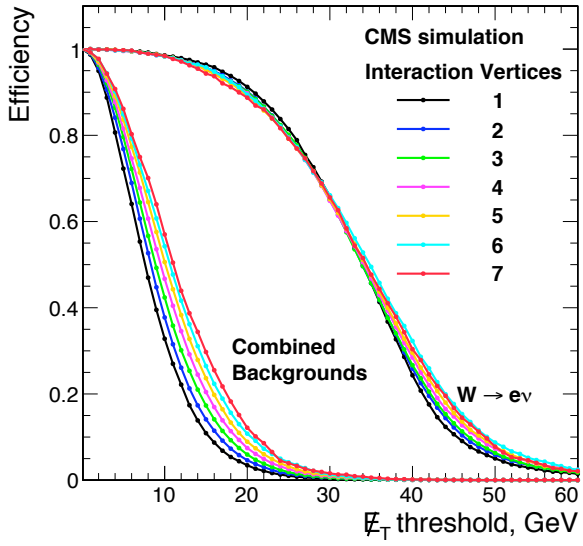

Figure 2.38: Efficiency of $W \to e\nu$ event selection versus $\not\!\!E_T$ threshold on signal and background. [26]

Effect of pile-up

Finally, the effect of pile-up on MET performance is studied.

Pile-up affects considerably only the resolution of $\not\!\!E_T$, because the expected value of $\not\!\!E_T$ is minimum bias events is zero.

This is an important effect in the analysis: if the MET has a worse resolution, the W p_T smearing caused by this can alter the shape of angular distributions significantly.

Resolution as a function of the number of reconstructed primary vertices has been studied in data with the methods already discussed for calibration.

As a general rule, the resolution gets worse as the number of PV increases (Fig. 2.40). Especially at low q_T, the resolution is negatively affected by the underlying event and the noise,

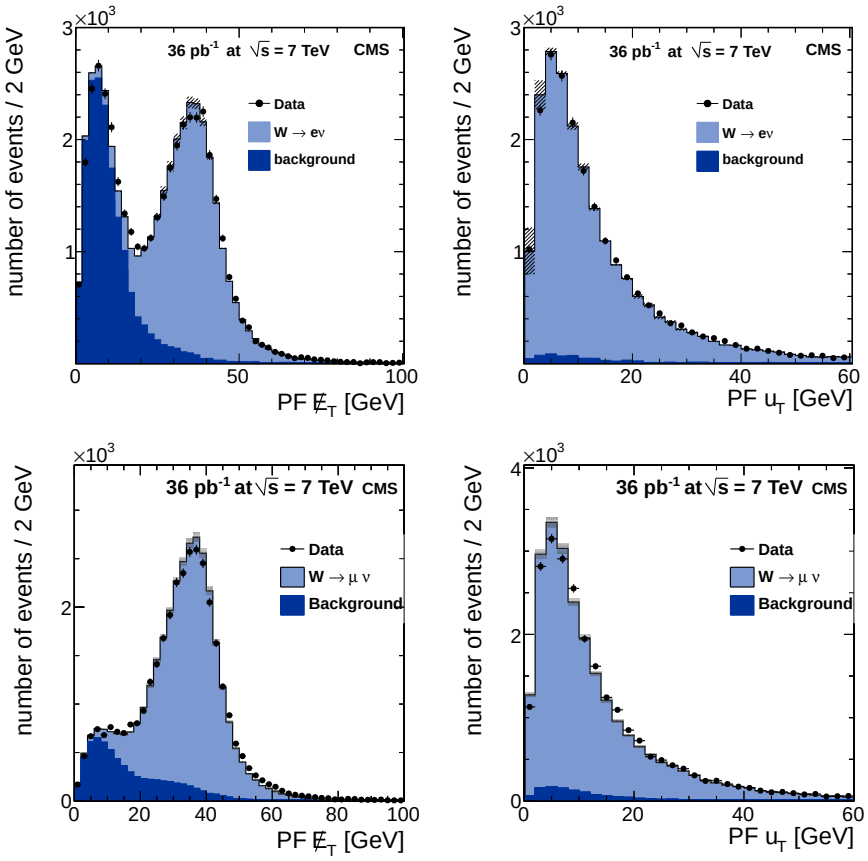

Figure 2.39: PF $\not\!\!E_T$ and u_T distributions in $W \rightarrow l\nu$ candidate events. The main contributions to the background come from jet events (with a jet faking a lepton), and Z dilepton decays where one lepton is not detected. [26]

that become difficult to distinguish from the hadronic recoil, making energy scale corrections difficult.

The PFMET has - once again - the best resolution, and is correctly described by the simulation.

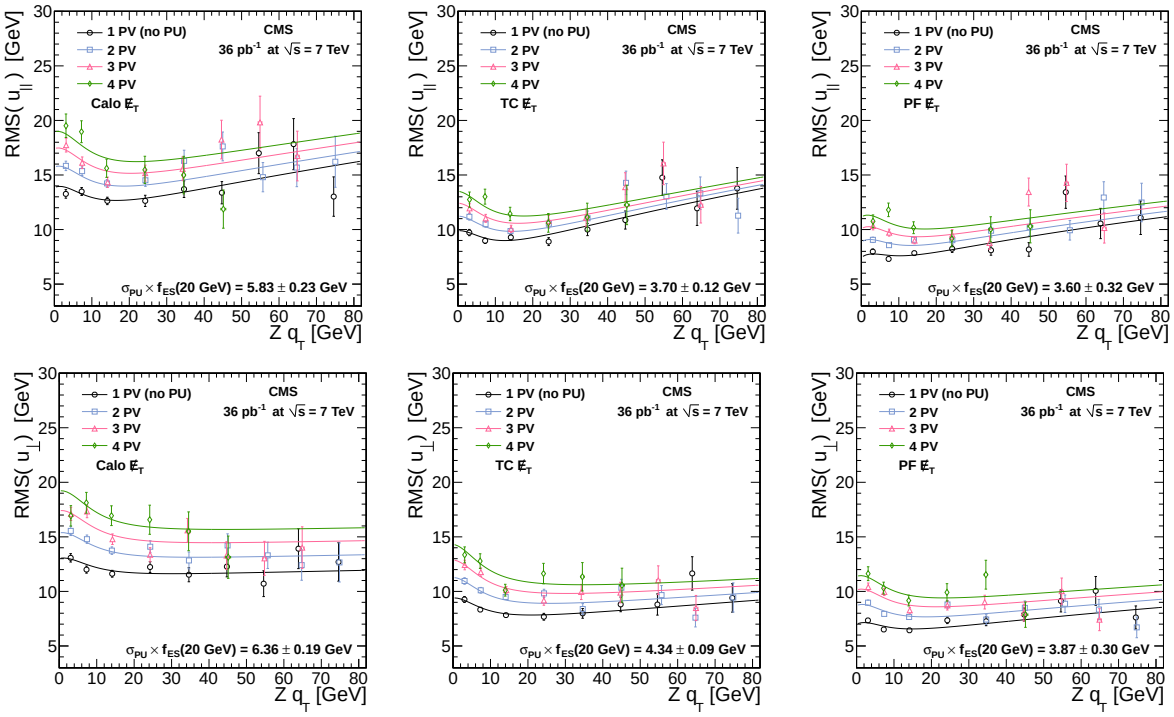

Figure 2.40: Resolution versus the q_T of the Z for the parallel component (top) and perpendicular component (bottom) for (left to right) Calo $\not\!\!E_T$, TC $\not\!\!E_T$, and PF $\not\!\!E_T$, as a function of the number of reconstructed primary vertices. [26]

Chapter 3

Measurement of W polarization

The CMS Collaboration has recently published the first measurement of the polarization that W bosons exhibit at large p_T in W+jets events at a pp collider [6, 31, 32], in both muon and electron channels. The work shown in this thesis contributed to this measurement.

When not explicitly mentioned, all angular quantities are expressed in the helicity frame. This frame has been chosen because of the limited statistics available at the time of the publication: with this choice, actually, the dominant left handed polarization of the W along its direction of flight emerges clearly.

As already discussed in Chapter 1, there is the problem of reconstructing the decay lepton's momentum in such frame; in order to do this, the $\cos\theta^*$ variable will be replaced by the Lepton Projection (LP) variable described in Section 3.3, which can be calculated from tranverse quantities only and exhibits, at high p_T , a remarkable degree of correlation with $\cos\theta^*$.

After having demonstrated the efficiency of such a method on simulated events, the results of the measurement of W boson polarization using the first 36 pb^{-1} of data collected by the CMS experiment are presented, and compared to a NLO MC simulation.

In the next chapter, the same technique will be applied to the most recent data sample of Z bosons produced in association with jets and decaying in the muon channel, recorded by CMS until June 2011 and corresponding to an integrated luminosity of 642 pb^{-1}.

3.1 Generator-level expectations

The MADGRAPH [33] Monte Carlo generator, interfaced to PYTHIA [34], has been used to produce approx. 15 million W+Jets and 1.2 Z+Jets events at a center-of-mass energy of $\sqrt{s}$ = 7 TeV. The CTEQ6L1 set from the LHAPDF [35] package of parton distribution functions has been adopted.

The generator-level expectations for the $\cos\theta^*$ distributions and the polarization parameters f_L, f_R, f_0 are shown for W bosons in Fig. 3.1 and 3.2.

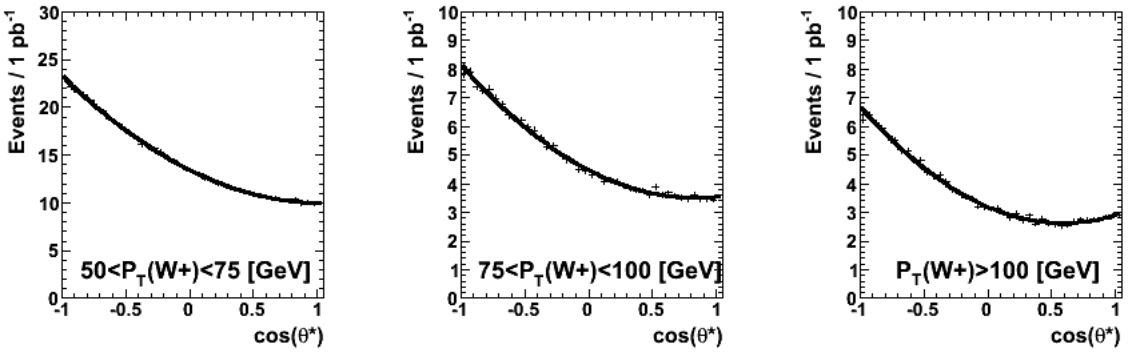

Figure 3.1: The $\cos\theta^*$ distribution for the positively charged lepton, shown in bins of $p_T(W)$ for the W^+ . The expected yield for 1pb^{-1} is shown together with the analytical fit. Bin width: 0.05. [6]

The features predicted by SM calculations [2] and described in Section 1.4 are correctly reproduced by the MC simulation. Table 3.1 summarizes their expected polarization in three different p_T bins.

Table 3.1: Helicity parameters of W bosons for three different p_T bins, at the generator level. [6]

	boson:lepton charge	$50 < p_T(V) < 75$ GeV	$75 < p_T(V) < 100$ GeV	$p_T(V) > 100$ GeV
f_L	$W:+$	0.536 ± 0.002	0.552 ± 0.003	0.599 ± 0.004
f_R	$W:+$	0.229 ± 0.002	0.239 ± 0.003	0.258 ± 0.003
f_L	$W:-$	0.507 ± 0.002	0.537 ± 0.004	0.571 ± 0.005
f_R	$W:-$	0.259 ± 0.002	0.276 ± 0.004	0.289 ± 0.004

In a similar way, the A_i asymmetry coefficients predictions are reported in Fig. 3.3.

The lower cut of 50 GeV for vector boson p_T is an optimized compromise between the amount of statistics and the polarization effects emerging at high p_T .

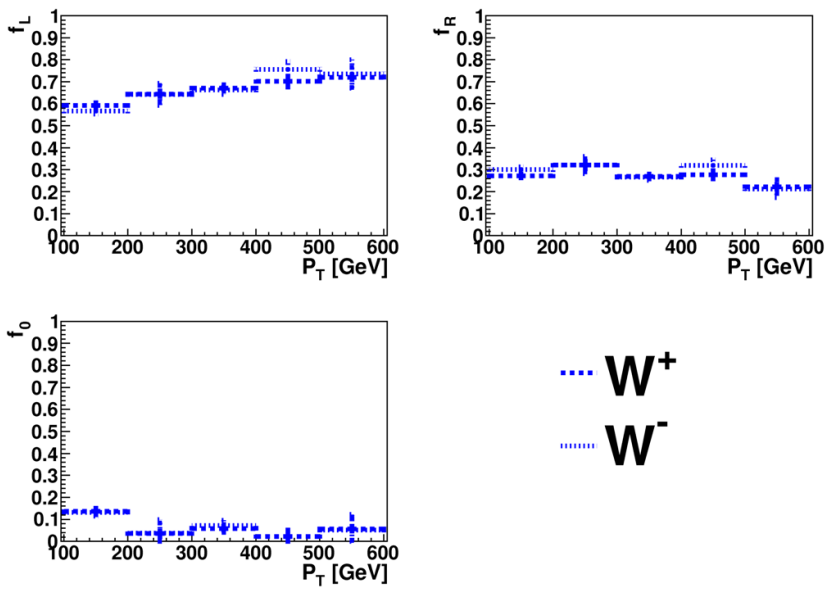

Figure 3.2: The p_T dependence of the W boson helicity parameters f_L, f_R and f_0, at the generator level. [6]

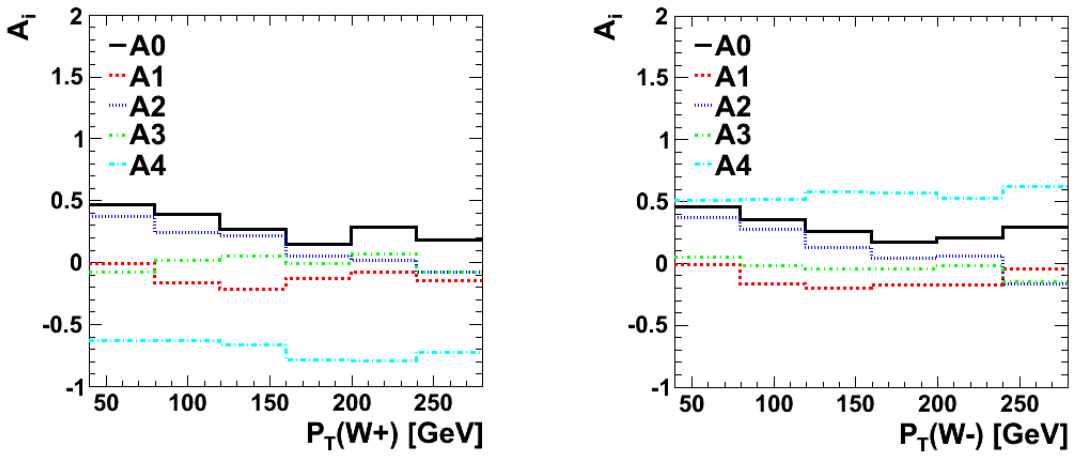

Figure 3.3: Asymmetry coefficients A_i in the helicity frame for both charges as a function of $p_T(W)$. [6]

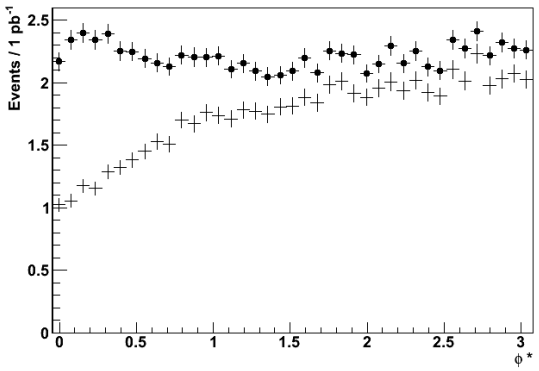

Figure 3.4: The lepton ϕ^* distribution at generator level before (solid dots), and after an acceptance cut of $p_T(e) > 10$GeV and $|\eta(e)| < 2.1$ for $p_T(W) > 100$GeV. Bin width: 0.08. [6]

3.2 Template fit method

3.2.1 Motivations at generator level

Angular distributions for $\cos\theta^*$ are distorted, already at the generator level, by the limited acceptance for leptons.

In this case, actually, the $\cos\theta^*$ distribution, that should be nominally dependent only on the A_0 and A_4 asymmetry coefficients, acquires a contribution also from other terms of the differential cross section; this is due to the fact that detector acceptance α, once convoluted with the differential cross section, prevents terms dependent on ϕ^* from vanishing:

$$\int_0^{2\pi} \alpha(\phi^*) \cos\phi^* \; d\phi^* \neq 0$$

Fig. 3.4 shows such distortion of the ϕ^* distribution at the generator level, with an acceptance cut on the decay lepton, for W $p_T > 100$ GeV/c .

The most affected region is the $\phi^* \approx 0$ one; this is easily understood taking into account the definition of the helicity frame: leptons with $\phi^* \approx 0$ are directed (in both cases of W produced with positive or negative rapidity in the experiment) close to the beam (Fig. 1.2).

In conclusion, already at the generator level, the $\cos\theta^*$ distribution is distorted by an amount which depends not only the acceptance region itself, but also on W p_T and polarization (because both affect the angular distribution of the lepton in the laboratory frame).

It's therefore difficult to pursue a strategy based on a fit with analytical functions, because an analytical description of these effects would be needed: a fit with templates is better suited.

The situation, however, becomes even more complex when detector effects (such as finite resolution and imperfect reconstruction) come into play.

3.2.2 Motivations at RECO level

The impact of finite resolution of physics objects at reconstruction level can be taken into account by means of the GEANT4 [36] simulation of the CMS detector, eventually complemented by data-driven techniques as already discussed in Chapter 2. In other words, MC templates can be built up from physics objects reconstructed from fully simulated events (RECO-level).

However we shall not use the $\cos\theta^*$ variable introduced in the previous section, due to the impossibility to reconstruct, at a hadron collider, the neutrino p_T , and therefore the $\cos\theta^*$ of the decay lepton in the helicity frame.

3.3 Lepton Projection variable

Instead of trying to fit the unaccessible $\cos\theta^*$ distribution in data, the following variable is defined from transverse quantities only:

$$\mathrm{LP} = \frac{\vec{p}_T(l) \cdot \vec{p}_T(W)}{|\vec{p}_T(W)|^2} \tag{3.1}$$

The LP is the projection of the lepton's tranverse momentum along the W direction of flight in the transverse plane, normalized to the energy scale of the event (i.e. the W p_T).

Other methods could have been used to recover some information on the $\cos\theta^*$ distribution from measured quantities; for example, the W mass constraint could have been introduced to restrict the p_z of the W to two possible values, and then:

- choose one of them (for instance, the smallest one) and correct for the presence of wrongly selected solutions, or
- use both possible values, weighting them according to the MC simulation.

The LP method, instead, is more robust and simple, because it's based on the transverse measured quantities only, and fits also better to searches for new physics, where no mass hypothesis is available and distinctive signatures are expected on the transverse plane.

The use of Collins-Soper frame would have required much larger statistics than available at the time of this analysis.

Correlation with $\cos\theta^*$

The crucial feature of the LP variable is its high degree of correlation, at high p_T , with $\cos\theta^*$ (Fig. 3.5).

This can been investigated through the $\cos_{col}\theta^* = 2(\mathrm{LP} - \frac{1}{2})$ variable (Fig. 3.6).

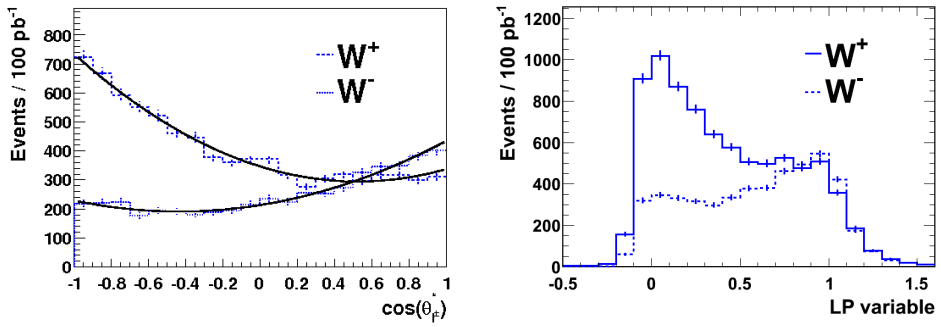

(a) (b)

Figure 3.5: The $\cos\theta^*$ and LP distributions for both lepton charges from W boson decays $p_T > 100$ GeV. [6]

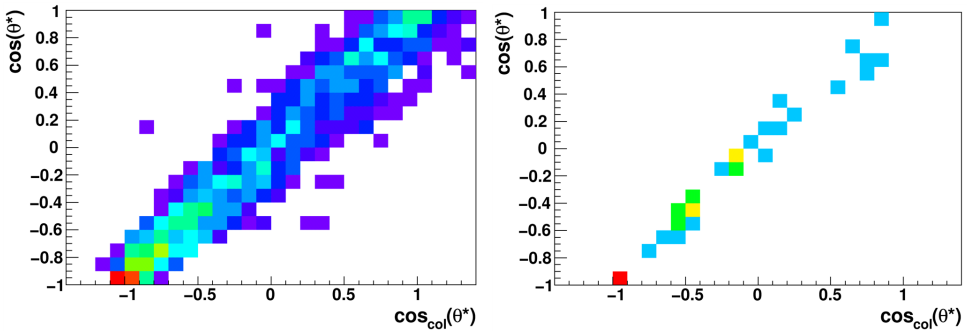

(a) (b)

Figure 3.6: Correlation plot between $\cos(\theta^*)$ and $\cos_{col}(\theta^*)$, for W bosons with a transverse momentum above a) 200, b) 400 GeV. [6]

Let's consider the components of lepton momentum along and orthogonal to the flight direction of the W in the laboratory frame:

$$p^l_{||} = \gamma \frac{M_W}{2}(\beta + \cos\theta^*)$$

$$p^l_{\perp} = \frac{M_W}{2}\sin\theta^*$$

For high-p_T W, the approximations $\beta \approx 1$, $\gamma \approx p^W/M_W$, $p^l_{||} \gg p^l_{\perp}$ hold.

Therefore one obtains:

$$p^l \approx \frac{p^W}{M_W}\frac{M_W}{2}(1 + \cos\theta^*)$$

$$\cos\theta^* \approx 2\left(\frac{p^l}{p^W} - \frac{1}{2}\right)$$

In these conditions LP $\approx p^l/p^W$, so $\cos\theta^* \approx 2(\mathrm{LP} - \frac{1}{2}) = \cos_{col}\theta^*$.

Values of LP ≈ 1 correspond to forward ($\cos\theta^* \approx 1$) emission, while LP ≈ 0 means backward ($\cos\theta^* \approx -1$) emission of the decay lepton.

Correlation with ϕ^*

It is important to study the correlation between LP and ϕ^* because a LP-based measurement of f_L, f_R, f_0, that nominally depend only on the A_0 and A_4 asymmetry coefficients, will implicitly assume values for the other A_i.

The LP variable, actually, is not correlated with ϕ^* only in the massless limit for the W, i.e. at very high p_T . In this limit, the lepton has to fly essentially collinear to the W, and the ϕ^* has therefore no role in the event topology.

At low momentum, on the other hand, the ϕ^* influences significantly the projection of the lepton $\vec{p_T}$ along the W $\vec{p_T}$ in the laboratory frame, because their flight directions can be very different (Fig. 3.7).

Interestingly, the specific $\phi^* = \pi/2$ value has no impact: that topology, actually, corresponds in the helicity frame to the lepton p_T getting a contribution from the non-zero mass of the W in a direction orthogonal to the W p_T in the laboratory frame, thus not affecting the LP variable.

Another striking effect, in this low-p_T situation, is that the LP distribution extends the interval of $\cos_{col}\theta^*$ also beyond $[0, 1]$.

In order to study the sensitivity of the LP templates with respect to the A_i, the difference in shape of the LP distribution after a change of 10% (in each bin of W (p_T, η)) of A_i coefficients has been determined (Fig. 3.8).

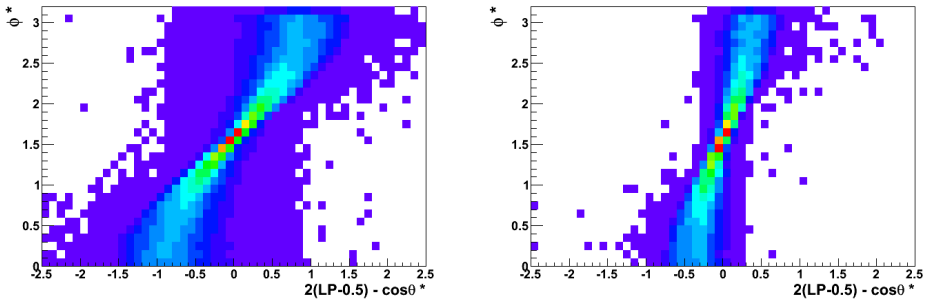

(a) (b)

Figure 3.7: Correlation plot between [$\cos_{\text{col}}(\theta^*)$ - $\cos(\theta^*)$] and ϕ^*, for a) $50 < p_T(W) < 100$GeV, b) $p_T(W) > 100$GeV. [6]

All A_i contributions decrease with the W p_T ; moreover, an increase of A_0 enhances the longitudinal polarization, affecting the LP ≈ 0 and the LP ≈ 1 regions in the same direction, and the LP ≈ 0.5 region with a different sign; an increase of A_4, on the other hand, strongly affects the left and right handed components with different sign. This indicates that the analysis is very sensitive to the $A_4 \propto (f_L - f_R)$ quantity.

This effect will be also studied at RECO-level in the MC simulation, and included as a systematic uncertainty on the final results.

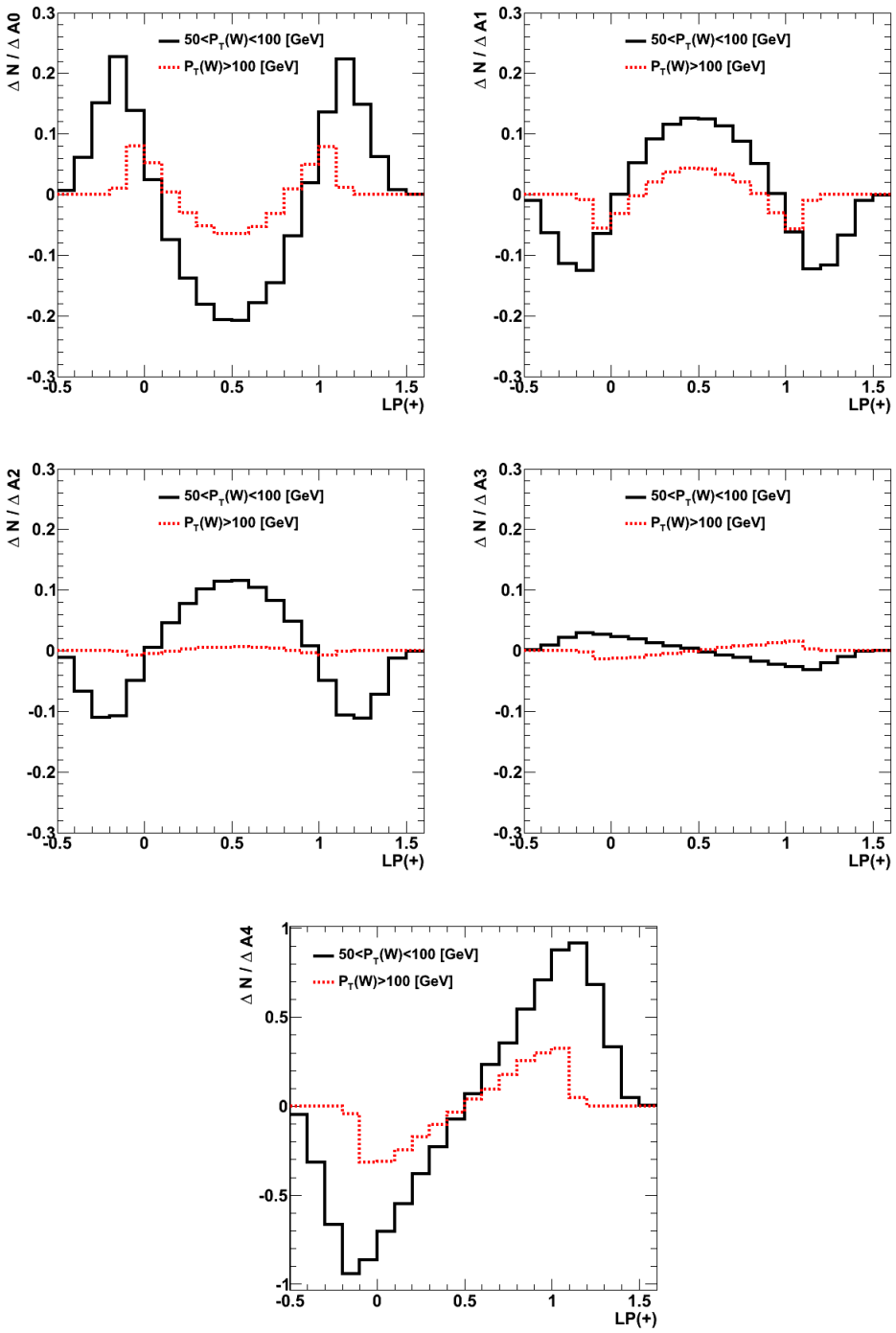

Figure 3.8: Derivative LP(+) with respect to A_i shown for $50 < p_T(W) < 100$GeV (black) and $p_T(W) > 100$GeV (red). [6]

3.4 Template generation procedure

Three different templates are needed in the fit; for given event selection and reconstruction conditions, three distinct simulations should be done to generate them, each with a 100% left-handed, right-handed or longitudinal vector boson.

Since our MC samples were generated with no polarization, we have adopted a reweighting technique; this also has the advantage of reducing the computational overhead.

The reweighting takes place, on a event-by-event basis, in three steps that involve specific multiplicative factors.

The first one (k_1) will change the angular distribution of the lepton in the helicity frame to the 100% polarized shape, bin by bin in W (p_T, η); the second one (k_2) will set the relative weight of W (p_T, η) bins to match the one that would be observed at reco-level from a MC where a definite polarization exists; the third one (k_3) will adjust the global normalization of each template.

Let's discuss each of them separately.

3.4.1 Angular reweighting

The first step reweights each event, changing at the generator level the shape of the $\cos\theta^*$ distribution to the one expected for $f_L = 1$, $f_R = 1$, $f_0 = 1$ separately.

In order to do this, the W (p_T, η) phase-space is binned, indipendently for each charge, in 21 bins: 3 bins in W p_T (0-50 GeV/c , 50-100 GeV/c , >100 GeV/c) and 7 bins in $|\eta|$ (6 0.5-wide bins up to $|\eta|$=3, and one bin for $|\eta|$ >3).

In each of them, the gen-level $\cos\theta^*$ distribution is analytically fitted, and a $(f_L, f_R, f_0)^{old}$ set is extracted; afterwards, the $\cos\theta^*$ is segmented in 200 bins (0.01-wide).

The reweighting factor is then calculated, for a given event with $\cos\theta^*$ falling in the bin b, as follows:

$$k_1^{\pm}(p_T^W, |\eta^W|) = \frac{\int_b F^{new}(\cos\theta^*) d\cos\theta^*}{\int_{-1}^{1} F^{new}(\cos\theta^*) d\cos\theta^*} \div \frac{\int_b F^{old}(\cos\theta^*) d\cos\theta^*}{\int_{-1}^{1} F^{old}(\cos\theta^*) d\cos\theta^*} \tag{3.2}$$

where

$$F^{new,old}(\cos\theta^*) = f_L^{new,old} \frac{(1 \mp \cos\theta^*)^2}{4} + f_0^{new,old} \frac{\sin^2\theta^*}{2} + f_R^{new,old} \frac{(1 \pm \cos\theta^*)^2}{4}$$

The $\mp$ signs refer to different charges of the W, and $f_{L,R,0}^{new}$ represents the 100% polarized configuration (i.e. is a set among (1,0,0), (0,1,0), (0,0,1)).

The dependence of this correction on the W (p_T, η) is important, and generates a subtle effect that is addressed by the second step of the reweighting procedure.

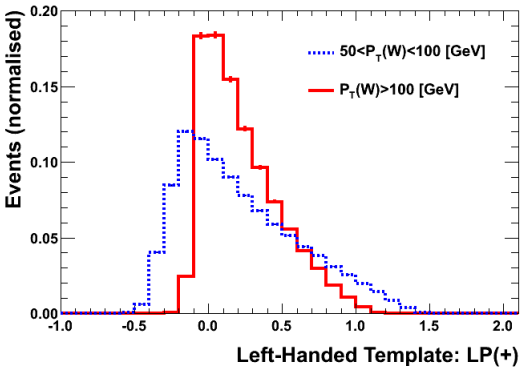

Figure 3.9: The 100% left-handed normalized template shown for the LP(+) variable in two bins of $p_T(W)$ at generator level. [6]

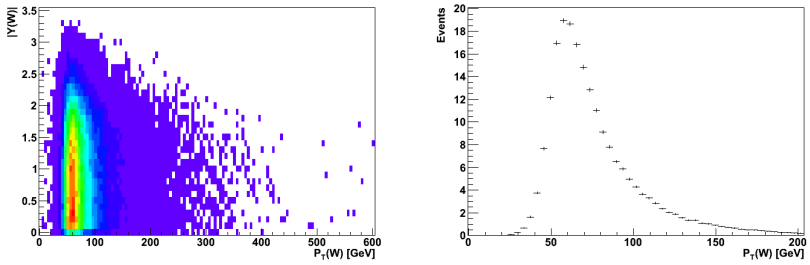

(a) (b)

Figure 3.10: a) The generator-level absolute W rapidity $|Y(W)|$ vs. $p_T(W)$ distribution for a reconstruction level $p_T(W) > 50$ GeV cut. b) The generator-level $p_T(W)$ distribution for a reconstruction level $p_T(W) > 50$ GeV cut. [6]

3.4.2 Unfolding of RECO W p_T smearing

Since the LP variable is sensitive to the W (p_T, η) (Fig. 3.9), the bins introduced in the previous paragraph have to be weighted according to their population for 100% left, right and longitudinal polarization respectively.

Each bin, actually, has to contribute to the template with a weight proportional to its population for the definite polarization case, which is in general different from the one observed in the MC simulation, where no definite polarization exists.

The first correction factor k_1 has been calculated using generator-level information; now, on the other hand, one has to consider that the aim of the analysis is to extract polarization information from a data sample selected in terms of reconstruction-level quantities, and consequently from a region of the W (p_T, η) space that corresponds to reconstruction-level selection.

The bin population, therefore, has to be determined taking into account only those W bosons whose reco-level kinematic quantities pass the event selection cutflow (i.e. with a RECO $p_T >$ 50 GeV/c). The result is, in general, different from the generator-level populations (Fig. 3.10,

for instance, shows that a W with gen-level $p_T < 50$ GeV/c can pass the cut at the reco-level).

The second correction factor is defined as follows:

$$k_2^{\pm}(p_T^W, |\eta^W|)_{L,R,0} = \frac{N^{\pm}_{L,R,0}}{\sum N^{\pm}_{L,R,0}} \div \frac{N^{\pm}_{TOT}}{\sum N^{\pm}_{TOT}} \tag{3.3}$$

where

$$N_{L,R,0} = \int_{(p_T,\eta)\ \text{bin}} \sigma^{'}_{W}(p_T,\eta)\ f^{'}_{L,R,0}(p_T,\eta)\ dp_T\ d\eta$$

is the population of a bin in the 100% polarized vector boson case, $N_{TOT} = N_L + N_R + N_0$ is the total population of that bin, and the sum runs on all 21 (p_T, η) bins.

The prime in the notation of equation above indicates that the reco-level phase space has to be considered, not the generator-level one.

After this correction, events in each bin have been reweighted proportionally to the bin population in the case of definite W/Z polarization. It should also be noted that the global normalization of the templates is, at this stage, the same for left, right and longitudinal ones.

3.4.3 Acceptance correction

In the end, the effect of lepton acceptance and reconstruction efficiency on the templates has to be introduced.

Templates are built from simulated events, selected with the same cutflow used on data, and using reco-level quantities.

Remember now that the k_1,k_2 correction factors, applied on a event-by-event basis, yield three templates with the same normalization (by construction), each of them with the shape that would be observed in data if W bosons had a definite polarization.

But the relative normalization of the L,R,0 templates could be influenced by the fact that different polarizations can result in different global efficiencies for passing the analysis cuts.

This argument should make clear that an additional correction is required on the fit results (i.e. on the normalization of each template, not on its shape); it takes the following form:

$$C^{\pm}_{L,R,0} = \frac{\int \sigma^{'}_{W}(p_T,\eta)\ f^{'}_{L,R,0}(p_T,\eta)\ \epsilon_{CMS}(p_T,\eta) dp_T\ d\eta}{\int \sigma^{'}_{W}(p_T,\eta)\ f^{'}_{L,R,0}(p_T,\eta)\ dp_T\ d\eta} \tag{3.4}$$

where ϵ_{CMS} is the efficiency due to lepton acceptance and reconstruction of the CMS detector.

3.5 Event selection

3.5.1 Muon channel

The following selection has been used to obtain a sample enriched in W bosons (produced in association with jets) decaying in the muon channel. The definitions of these physics objects have already been presented in Chapter 2.

- HLT_Mu9 or HLT_Mu15 trigger requirement (non-isolated muon triggers with 9-15 GeV/c p_T threshold).
- Exactly one tight muon, with $p_T > 20$ GeV/c and $|\eta| < 2.1$.
- No electron passing the LooseID 95% efficiency point with $p_T > 20$ GeV/c and $|\eta| < 2.5$.
- Less than four jets reconstructed by the Particle Flow algorithm (anti-k_T with $\Delta R = 0.5$ cone) with $p_T > 20$ GeV/c and $|\eta| < 5$.
- A ΔR between the muon and each jet of at least 0.5.
- A transverse mass of the muon-PFMET system of at least 30 GeV/c .
- A veto on events with a second global muon with $p_T > 10$ GeV/c .
- A $p_T(\mathrm{W}) > 50$ GeV/c cut (where $p_T(\mathrm{W})$ means $|\mathrm{PF}\not{E}_T + \vec{p}_T(\mu)|$).

The trigger is the lowest unprescaled muonic one (and therefore varies with increasing instantaneous luminosity of the machine), and a sufficiently high offline muon p_T cut has to be used, in order to obtain a homogeneus sample along the whole period of data taking.

The main backgrounds for the $W \to \mu\nu$ channel are QCD, Z+Jets, and $t\bar{t}$.

This selection has been optimized to reject them as much as possible; in particular, the tight muon ID and the ΔR muon-jet matching reduce QCD contribution, while the less-than-four-jets cut is against the $t\bar{t}$.

Event yields are shown in Table 3.2.

Data/MC comparison

Data/MC comparisons of important quantities of the event ($p_T(\mu)$, $|\eta(\mu)|$, $p_T(W)$, M_T and LP) are shown in Fig. 3.11-3.15.

In these plots, the MC is normalised to the integrated luminosity. The agreement is good, within the uncertainty associated to the integrated luminosity; only the MT distribution (which is determined by MET performance) is slightly broader in data than in MC, as already observed.

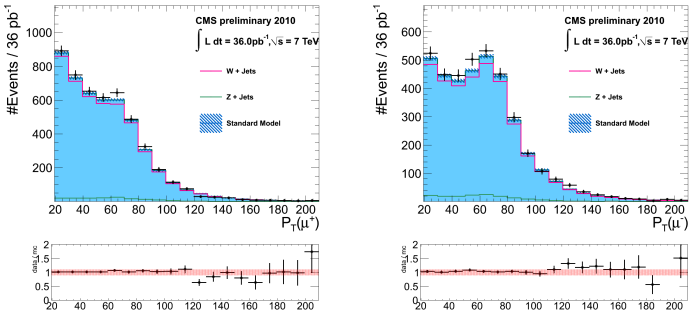

(a) (b)

Figure 3.11: The $p_T(\mu)$ distribution from 36 pb^{-1} of 7 TeV collision data, a) for μ^+ b) for μ^-. [31]

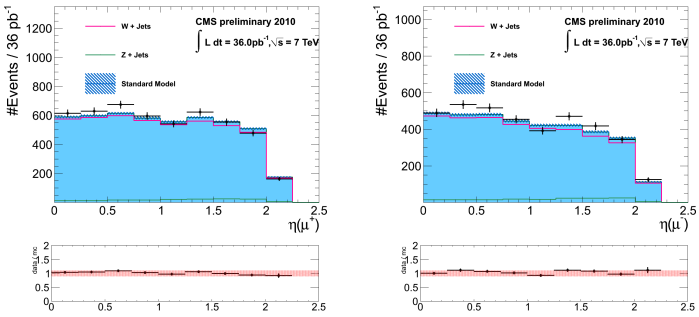

(a) (b)

Figure 3.12: The $|\eta(\mu)|$ distribution from 36 pb^{-1} of 7 TeV collision data, a) for μ^+ b) for μ^-. [31]

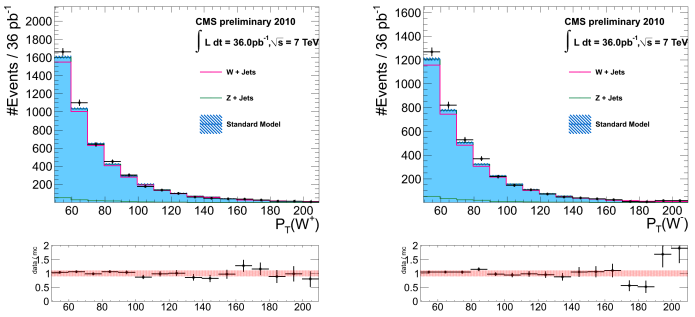

(a) (b)

Figure 3.13: The $p_T^{\mathrm{RECO}}(W)$ distribution from 36 pb^{-1} of 7 TeV collision data, a) for μ^+ b) for μ^-. [31]

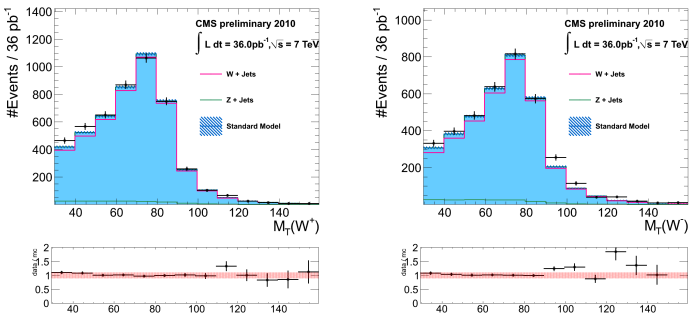

(a) (b)

Figure 3.14: The M_T distribution from 36 pb^{-1} of 7 TeV collision data, a) for μ^+ b) for μ^-. [31]

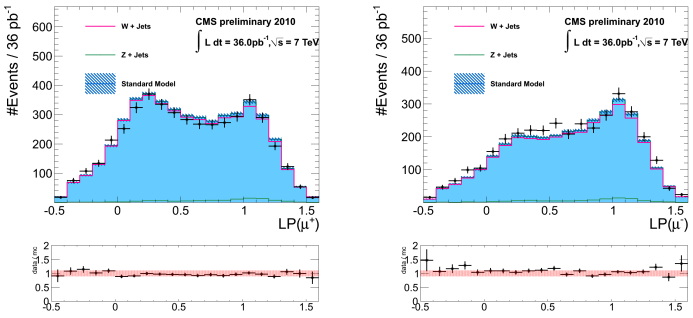

(a) (b)

Figure 3.15: The LP variable distribution from 36 pb^{-1} of 7 TeV collision data, a) for μ^+ b) for μ^-. [31]

Table 3.2: Muon channel event-yields for signal (W) and SM backgrounds, expected for an integrated luminosity of 1 pb^{-1} following the selection requirements. [6]

	W+Jets	QCD	Z+Jets	$t\bar{t}$	S/B
Trigger	7033	493887	909	28.1	0.01
$N_\mu = 1$, $N_e = 0$	5086	27792	376	11.4	0.18
< 4 jets	5067	27740	368	5.5	0.18
$\Delta R_{\min}(\mu, \text{jet}) < 0.5$	4979	26762	358	5.3	0.18
Second Muon Veto	4973	26762	232	4.3	0.19
$p_T(W) > 50$GeV	264	21.3	14.6	3.1	6.8
$M_T > 30$GeV	218	0.0	5.4	2.0	26.0

3.5.2 Electron channel

The selection in the electron channel is also optimized against the relevant backgrounds, that are in general larger than for the muon channel:

- HLT lowest unprescaled electron trigger
- Exactly one tightly-identified electron (70% efficiency point) with $p_T > 15$ GeV/c and $|\eta| < 2.4$.
- No other loose (95% eff. point) electron with $p_T > 15$ GeV/c and $|\eta| < 2.4$.
- No global muons with with $p_T > 15$ GeV/c and $|\eta| < 2.1$.
- Less than four jets reconstructed by the Particle Flow algorithm (anti-k_T with $\Delta R = 0.5$ cone) with $p_T > 30$ GeV/c and $|\eta| < 5$.
- A transverse mass of the electron-PFMET system of at least 50 GeV/c .
- A p_T(W) > 50 GeV/c cut (where p_T(W) means $|\text{PF}\not{E}_T + \vec{p}_T(e)|$).

The event yields for signal and backgrounds are in Table 3.3.

The main background, in this case, is from QCD events where a misidentification of jets has occurred (for instance, an electromagnetic deposit from a π^0 overlapping with a track from a charged hadron); moreover, electrons can be the result of photon conversions, or decays of heavy-flavour objects; finally, mismeasured (missed-leg Z decays) or misreconstructed (fake electrons) Z events can also contribute.

The dominant QCD background can be studied inverting one or more electron identification cuts; the $\Delta\eta_{in}$ and $\Delta\phi_{in}$ variables have been chosen for this procedure.

The LP shape is found to depend on these variables in a neglible way (Fig. 3.16); therefore, the anti-selected sample can be used as a model for QCD background in the final fit. The systematic uncertainty associated with this method will be evaluated later.

Table 3.3: Electron channel event-yields for signal (W) and full list of SM backgrounds, expected for an integrated luminosity of 1 pb^{-1}. [6]

Cut	W+Jets	QCD	Z+Jets	γ+jets	$t\bar{t}$	S/B
Trigger	6887.0	621013	804.4	1664.1	85.7	0.0
$N_e == 1$	2819.7	214.6	170.7	64.4	14.0	6.1
$N_\mu == 0$	2819.6	214.5	169.9	64.4	12.1	6.1
< 4 jets	2816.2	213.5	169.2	64.4	6.7	6.2
W boson $p_T > 50$ GeV	182.2	17.2	28.4	15.9	5.0	2.7
$M_T > 50$ GeV	122.8	2.7	3.7	3.1	3.3	9.6

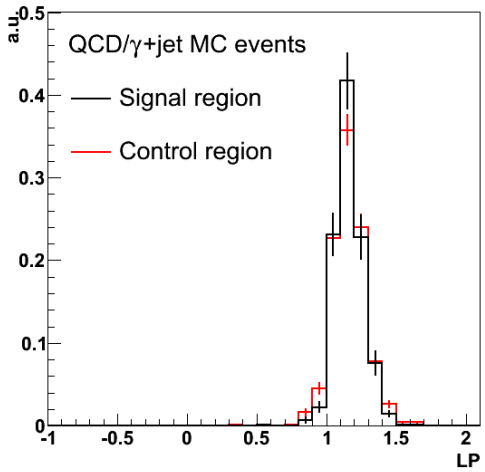

Figure 3.16: The LP variable plotted for selected and anti-selected QCD and γ + jets MC events, for W $p_T > 50$ GeV and $M_T > 50$ GeV. The anti-selected sample is taken by inverting the $\Delta\eta_{\text{in}}$ and $\Delta\phi_{\text{in}}$ cuts on the leading electron. [6]

Data/MC comparison

The same distributions already examined in the muon channel have been compared to MC expectations for the electron channel (Fig. 3.17-3.19).

Thanks to the data-driven technique (anti-selection) for estimating the QCD contribution, the agreement is remarkable.

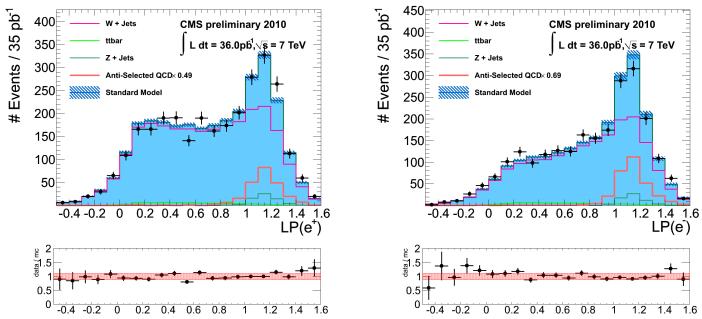

(a) (b)

Figure 3.17: LP(e) plot shown after the $M_T > 50$ GeV cut for both 7 TeV data (black points) and relevant Monte-Carlo samples, a) for e^+ b) for e^-. The total MC expectation is shown in blue. [31]

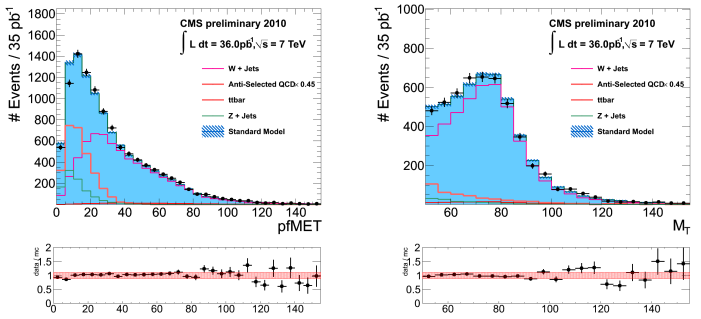

(a) (b)

Figure 3.18: a) E_T^{miss}, b) M_T plot shown after the $p_T(W) > 50$ GeV cut for 7 TeV data and Monte-Carlo. QCD taken from anti-selected data. [31]

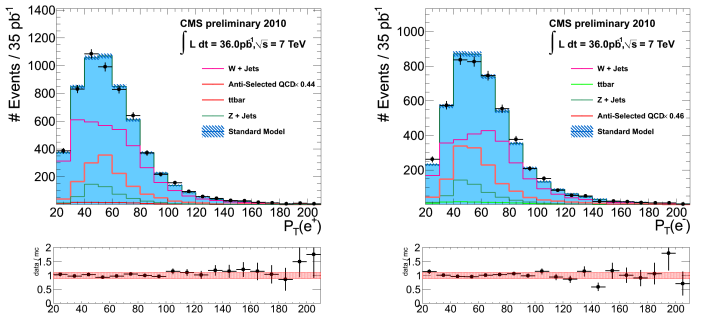

(a) (b)

Figure 3.19: Electron p_T plot shown after the $p_T(W) > 50$ GeV cut for 7 TeV data and Monte-Carlo, a) for e^+ b) for e^-. QCD taken from anti-selected data. [31]

3.6 Fit results

The measurements of the $\vec{f} = (f_L, f_R, f_0)$ parameters have been obtained by a binned maximum likelihood fit to the LP variable distribution, separately for W^+ and W^- , using the RooFit package [37].

Given the three template histograms h_L, h_R and h_0, the expected number of signal events in the j LP bin is:

$$S^j(\vec{f}) = f_L \cdot h_L^j + f_R \cdot h_R^j + (1 - f_L - f_R) \cdot h_0^j$$

so the fit has two effective degrees of freedom.

Moreover, the constraint $f_L + f_R \leq 1$ has to be introduced to avoid unphysical negative solutions for f_0. In terms of the $f_L - f_R$ and f_0 variables, the allowed area is a triangle with vertices in (1,0), (0,1) and (-1,0).

The observed data will contain both signal (S) and background (B), so the model for bin population becomes:

$$LP^j(\vec{f}) = f_{sig} \cdot S^j(\vec{f}) + (1 - f_{sig}) \cdot B^j$$

and the likelihood function to be maximized involves this model through the probability distribution $F^j(\vec{x}_j, \vec{f})$ of bin population:

$$L(\vec{x}_j, \vec{f}) = \prod_j F^j(\vec{x}_j, \vec{f})$$

3.6.1 MC toy

The fit performance has been tested on a MC toy dataset, built up from the model described above.

The distributions of the pull (i.e. the difference between the nominal quantity and the fitted one, divided by the statistical error returned by the fit) mean and sigma are consistent with a $N(0, 1)$ distribution (Fig. 3.20), so the fit procedure does not introduce any bias in the f_i extraction.

3.6.2 Closure test with MC templates

The efficiency of the template fit method has been tested comparing the results of an analytical fit to generator-level distributions to the result of the fit with templates (Fig. 3.21) built from a MC simulation to the MC simulated events themselves.

The results are shown in Table 3.4; it is seen that the template fit method (even if it makes use of correction factors in bins of W (p_T, η), and obtained by multiple fits to distributions with limited statistics) reproduces the gen-level information within the statistical uncertainty associated with the fit results.

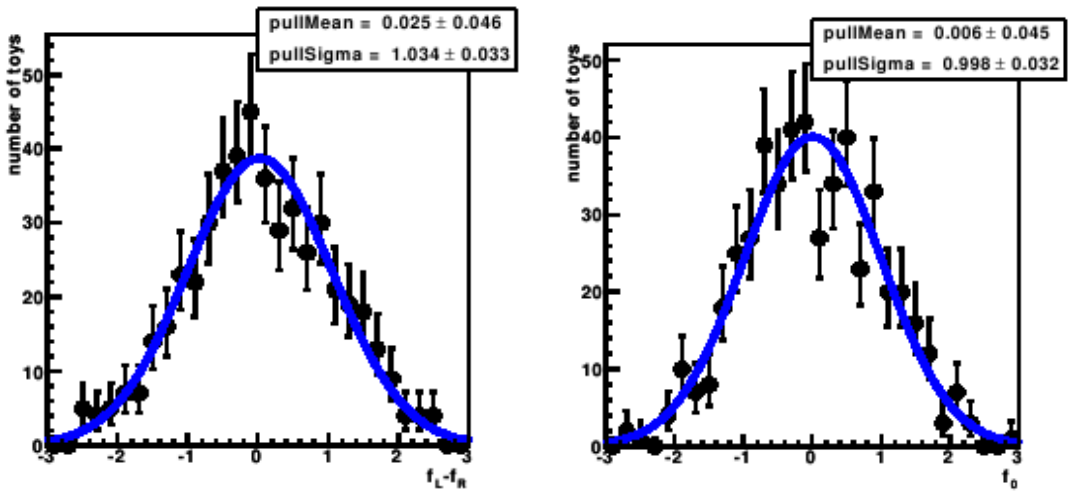

(a) (b)

Figure 3.20: Pull distributions of the $f_L - f_R$ and f_0 parameters, generated with a toy MC of 500 pseudo-experiments. [6]

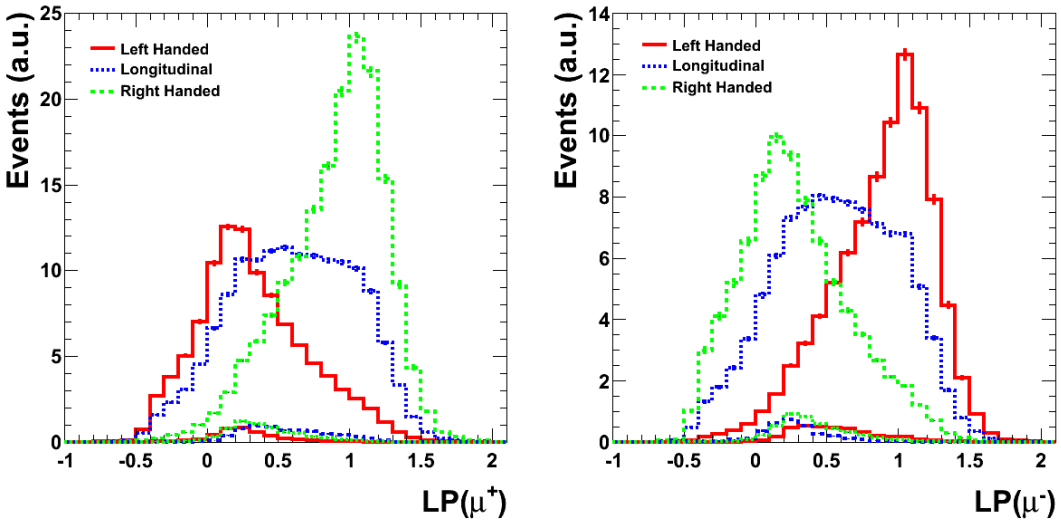

(a) (b)

Figure 3.21: The left-handed, right-handed and longitudinal LP templates as generated by the Monte Carlo, with the contribution to each template from $\tau \to \mu$ decays shown. [6]

Table 3.4: A closure test of the method described for template generation. The errors on the analytical fit results stem from the number of events in the Monte Carlo sample. [6]

	(a) Analytical Fit	(b) Template Fit: Gen-Level	(c) Template Fit: Reco-Level
f_L^-	0.5138 ± 0.0032	0.5149	0.5169
f_R^-	0.2714 ± 0.0027	0.2708	0.2690
f_L^+	0.5485 ± 0.0026	0.5506	0.5507
f_R^+	0.2270 ± 0.0021	0.2286	0.2291

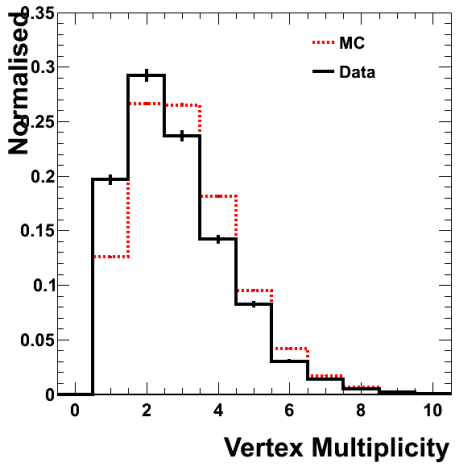

Figure 3.22: The vertex multiplicity distributions from the data (black) and Monte Carlo (red) in the muon channel after all selection criteria are applied. [6]

3.6.3 Data

The W polarization measurement has been performed, for the W, on data collected between March and November 2010, corresponding to an integrated luminosity of (36 ± 4) pb^{-1}, at a centre-of-mass energy of $\sqrt{s} = 7$ TeV.

In this sample, the average vertex multiplicity per event is 2.8.

Simulated events have been reweighted to have the same vertex multiplicity distribution observed in data (Fig. 3.22).

The fitted LP distributions are shown for positive and negative charge separately, in Fig. 3.23 and 3.24.

The fraction and shape of EWK background has been taken from the simulation. For the electron channel, the QCD background fraction has been fitted. The number of observed QCD events is found to be consistent with the MC.

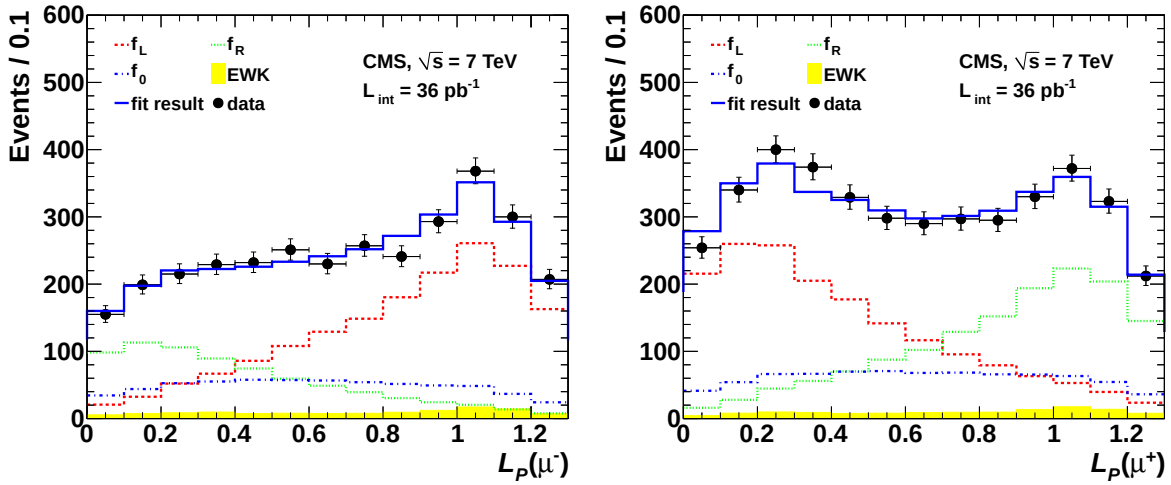

Figure 3.23: Fit results using 36 pb^{-1} of collision data for the $LP(\mu^+)$ and $LP(\mu^-)$ distributions. The left-handed, right-handed and longitudinal polarization components, with normalization as determined by the fit, are represented by the dashed, dotted, and dash-dotted lines respectively. The shaded distribution shows the EWK backgrounds. The solid line represents the sum of all individual components, and can be directly compared with the data distribution (circles). [31, 32]

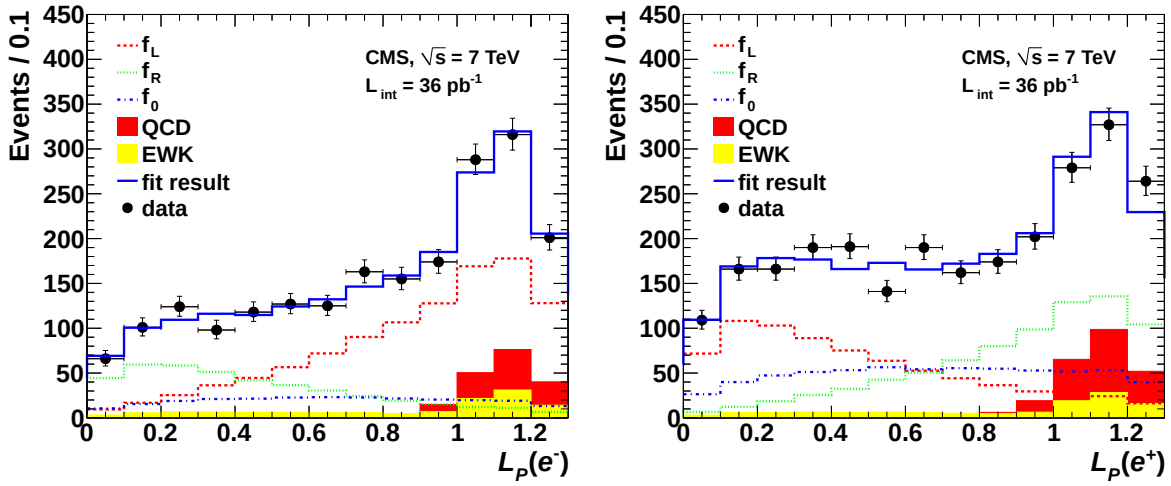

Figure 3.24: Fit results using 36 pb^{-1} of collision data for the $LP(e^+)$ and $LP(e^-)$ distributions. The left-handed, right-handed and longitudinal polarization components, with normalization as determined by the fit, are represented by the dashed, dotted, and dash-dotted lines respectively. The shaded distributions show the QCD and EWK backgrounds. The solid line represents the sum of all individual components, and can be directly compared with the data distribution (circles). [31, 32]

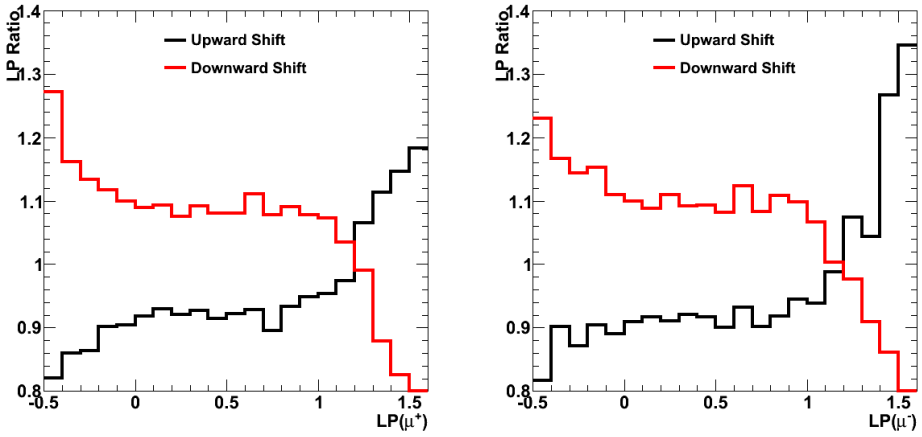

(a) (b)

Figure 3.25: The ratio of both upward shifted (black) and downward shifted (red) LP variables to the original distribution. [6]

3.7 Systematic uncertainties

Systematic uncertainties arising from both reconstruction (Tables 3.5-3.6) effects and theoretical (Table 3.7) predictions - which, however, give a minor contribution - have been considered.

3.7.1 MET scale

The p_T of the W is calculated using the missing transverse energy from the Particle Flow algorithm; therefore, an uncertainty on the absolute MET scale affects the LP variable directly, and the polarization fractions extracted by the fit.

This uncertainty has been estimated as recommended [38] by the JetMET group of the Collaboration:

- Sum back into the MET the lepton and the PF jets reconstructed with $p_T > 10$ GeV/c .
- Shift the remaining unclustered energy up/down by 5%.
- Shift each jet up/down according to the jet energy correction uncertainty.
- Recover the corrected MET subtracting the lepton and the jets.

The effect on the LP distribution is shown in Fig. 3.25.

The edges of the shape suffer significantly from this uncertainty, and including them in the fit can worsen the final statistical + systematic uncertainty on the polarization fractions extracted; therefore, an optimization study has been done to select the best LP range to include in the fit (Fig. 3.26). The fit range chosen for both charges and channels is (0.0,1.3).

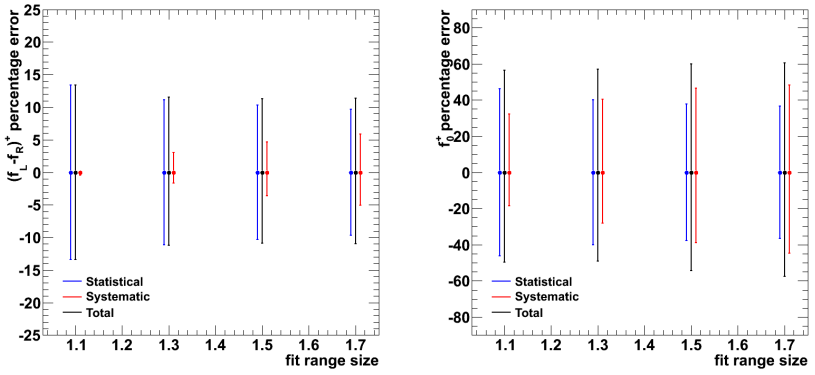

(a) (b)

Figure 3.26: Results of the fit range optimisation study for the $(f_L - f_R)^+$ and f_0^+ variables in the muon channel. For different charge and channel, similar results are obtained. [6]

Table 3.5: The relative effects on the values of f_0 and $(f_L - f_R)$ in the muon channel for the non-theoretical systematic uncertainties. The absolute values are shown in brackets. [31, 32]

Uncertainty	$(f_L - f_R)^-$	f_0^-	$(f_L - f_R)^+$	f_0^+
PF recoil scale	$\pm$11% (0.029)	$\pm$56% (0.123)	$\pm$3% (0.011)	$\pm$42% (0.092)
PF recoil resolution	$\pm$4% (0.012)	$\pm$3% (0.006)	$\pm$4% (0.012)	$\pm$2% (0.004)
$p_T(\mu)$ bias: $\pm$1%/100 GeV	$\mp$0.8% (0.002)	$\mp$ 11% (0.004)	$\pm$1.2% (0.004)	$\mp$16.0% (0.036)
Quadratic sum	$\pm$12% (0.031)	$\pm$56% (0.123)	$\pm$5% (0.017)	$\pm$45% (0.099)

3.7.2 MET resolution

The limited MET resolution determines a smearing of the reconstructed W p_T (Fig. 3.27).

Following the advice of the experts, the PFMET resolution has been broadened by 10%, and the fit procedure repeated on the smeared LP distribution.

3.7.3 Muon pt scale

The limited amount of statistics available for this analysis is barely sufficient to apply the MuScleFit method to correct for misalignment of the elements of the silicon tracker, and associate to this effect a systematic uncertainty.

Therefore, a simpler (with respect to Section 2.2.4) way of estimating the effect of changing the muon p_T scale on the polarization measurement has been used, that does not separate the data sample in many bins.

The reconstructed Z mass gets correction contributions with different signs for μ^+ and μ^- from misalignment effects. Given that the correction from the harder muon will be the dominant one (because the effect grows with p_T), events have been separated in two samples, according to the charge of the leading muon; moreover, a muon p_T cut > 75 GeV/c has been

Table 3.6: The relative effects on the values of f_0 and $(f_L - f_R)$ in the electron channel for the non-theoretical systematic uncertainties. The absolute values are shown in brackets. [31, 32]

	$(f_L - f_R)^-$	f_0^-	$(f_L - f_R)^+$	f_0^+
PF Recoil Scale	±16% (0.042)	±68% (0.150)	±9% (0.027)	±37% (0.078)
PF Recoil Resolution	±18% (0.046)	±21% (0.047)	±12% (0.037)	±18% (0.039)
Electron Scale Corrections ±50%	±6.7% (0.017)	±6.4% (0.014)	±6.1% (0.019)	±7.6% (0.016)
BG Estimation	±5.5% (0.014)	±31.3% (0.066)	±0.6% (0.002)	±1.4% (0.003)
BG Estimation (Stat)	±2.8% (0.007)	±17.1% (0.036)	±0.6% (0.002)	±6.4% (0.014)
Quadratic Sum	±26% (0.066)	±79% (0.174)	±16% (0.050)	±43% (0.090)

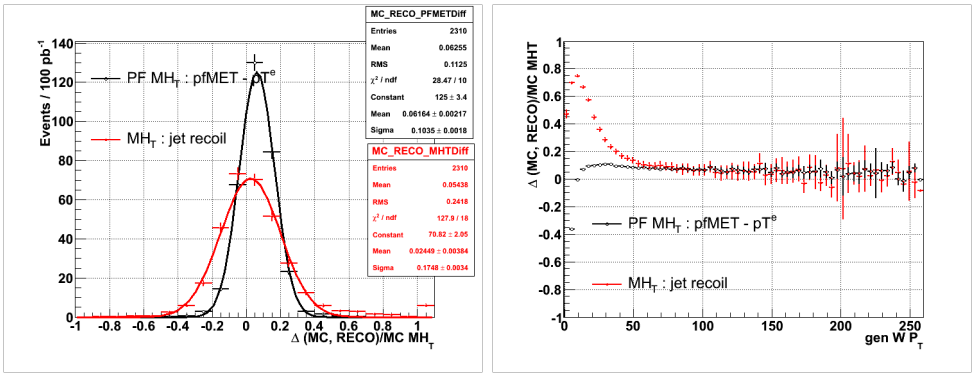

(a) (b)

Figure 3.27: a) The RECO $p_T(W)$ resolution, $(p_T^{\text{gen}}(W) - p_T^{\text{RECO}}(W))\ /\ p_T^{\text{gen}(W)}$, in the electron channel, using $|\vec{E}_T^{\text{miss}} + \vec{P}_T(e)|$ (black) and $|\sum_j \vec{P}_T^{j}(\text{jets})|$ (red) in the reconstruction. b) The RECO $p_T(W)$ resolution as a function of the generator $p_T(W)$. [6]

introduced (after an optimization study) to select events where the effect is more pronounced.

Then, the reconstructed Z mass has been obtained with a voigtian fit (Fig. 3.28) for each sample separately. The difference between the two values (note that the samples are uncorrelated, because they do not overlap) is compatible with 0 (Fig. 3.29, black) within the statistical uncertainty, which means that the assumption of no misalignment correction needed in the analysis is justified.

In order to estimate the systematic uncertainty associated to this choice, muon p_T scale in the MC simulation has been rescaled linearly with p_T (i.e. $\Delta p/p \propto p$), and then the same procedure applied to data has been performed; the results are in Fig. 3.29 (blue) as a function of the correction applied.

It can be inferred from the plot that a 1% muon p_T scale uncertainty at 100 GeV/c is a reasonable choice for uncertainty; therefore, the fit has been repeated after applying this correction, and the difference in results interpreted as a systematic uncertainty on them.

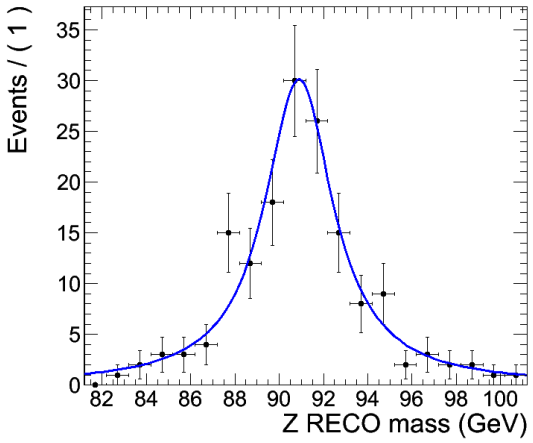

Figure 3.28: Shape of Z mass resonance observed in data for events with leading μ^+. [6]

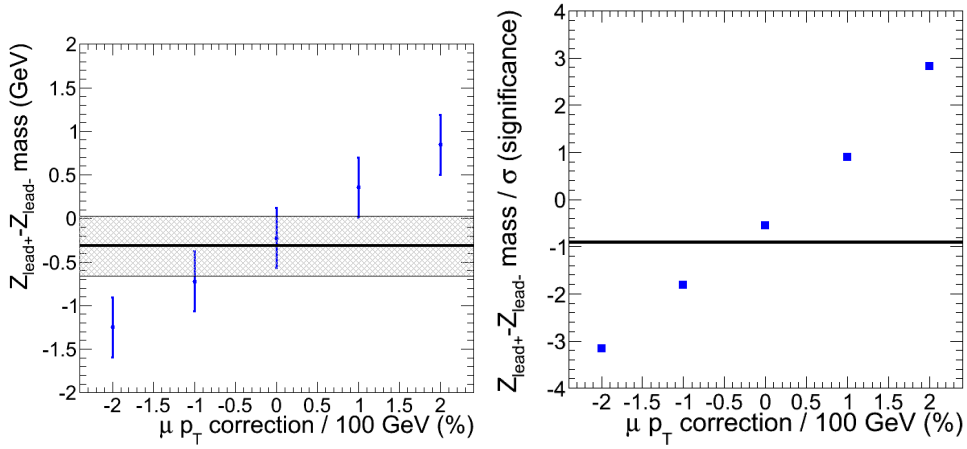

(a) (b)

Figure 3.29: a) In black, difference between fitted Z mass in events with leading μ^+ and μ^-. In blue, same measurement in MC simulation, with artificial charge asymmetric bias on muon p_T scale. b) Significance of previous values. [6]

3.7.4 Vertex multiplicity reweighting

The uncertainty associated to the reweighting of the vertex multiplicity distribution in the MC simulation to match the one observed in data has been evaluated by allowing the reweighting factors to vary within their statistical uncertainty.

The effect on the polarization results was found to be negligible.

3.7.5 Charge misID

A mismeasurement of the lepton charge will cause a cross-contamination between the W^+ and W^- samples, thus affecting the polarization fractions (that are different in the two cases).

For muons, this effect is negligible; for electrons, on the other hand, it is estimated to be smaller than 1%, which has a negligible impact on the final results, compared to other sources of systematic uncertainty.

3.7.6 Electron scale

An important effect on the electron energy scale is due to detailed description of transparency of ECAL crystals.

Correction factors have been obtained, in bins of electron p_T and η, from the Z mass resonance. These corrections affect the polarization measurement in a significant way; the systematic uncertainty has been evaluated repeating the fit with 50% larger correction factors.

3.7.7 Electron background estimation

The uncertainty due to electron QCD background estimation from anti-selected templates has been evaluated by comparing the fit results with the anti-selected sample and a MC QCD/γ simulation, and taking the difference between them.

Moreover, the statistical uncertainty on the number of events in the QCD template has been considered.

3.7.8 A_i correlation effects

As already discussed, the measurement of the A_0 and A_4 coefficients implicitly assumes values for the other A_i coefficients, whose effect on the LP distribution has been shown.

In order to evaluate the systematic uncertainty due to these correlations, the fit has been repeated after having increased/decreased each A_i coefficient by 10%, which is a reasonable value for their theoretical prediction uncertainty [2].

3.7.9 PDF uncertainties

The effect of uncertainties of the CTEQ6L1 PDF set on the measurement has been studied; after varying the parameters of the PDF set in the MC, the fit has been repeated, and the

impact has been found to be negligible ($< 0.01\%$).

3.7.10 Z and $t\bar{t}$ background estimation

The effect of varying the yield of Z+jets and $t\bar{t}$ events passing the event selection of 25% and 50% respectively is found to be negligible ($< 0.5\%$).

Table 3.7: The relative effects on the values of f_0 and $(f_L - f_R)$ from theoretical uncertainties. The absolute values are shown in brackets. [31, 32]

	$(f_L - f_R)^-$	f_0^-	$(f_L - f_R)^+$	f_0^+
$A_1 \pm (A_1 \times 10\%)$	$\pm$0.2% (0.0005)	$\mp$4.4% (0.0094)	$\pm$0.2% (0.0006)	$\mp$4.9% (0.0105)
$A_2 \pm (A_2 \times 10\%)$	$\pm$1.3% (0.0033)	$\mp$3.8% (0.0081)	$\mp$0.5% (0.0016)	$\mp$3.9% (0.0084)
$A_3 \pm (A_3 \times 10\%)$	$\mp$0.4% (0.0010)	$\pm$ <0.1% (0.0002)	$\pm$ <0.1% (0.0003)	$\pm$ <0.1% (0.0002)
$A_0 + (A_0 \times 10\%)$	<0.1%	+10.6%	<0.1%	+10.5%
$A_4 + (A_4 \times 10\%)$	+9.7%	<0.1%	+10.2%	<0.1%
Z changed by 25% (muon)	<0.5% (0.0013)	<0.5% (0.0011)	<0.5% (0.0016)	<0.5% (0.0011)
$t\bar{t}$ changed by 50% (muon)	<0.1% (0.0003)	<0.1% (0.0002)	<0.1% (0.0003)	<0.1% (0.0002)
Quadratic sum (muon)	$\pm$1.47% (0.0037)	$\pm$5.84% (0.0125)	$\pm$0.75% (0.0024)	$\pm$6.28% (0.0135)
Z changed 25% (electron)	<1% (0.0022)	<1% (0.0020)	<0.2% (0.0006)	<0.5% (0.0010)
$t\bar{t}$ changed by 50% (electron)	1.6% (0.0041)	2.1% (0.0045)	<0.2% (0.0005)	0.9% (0.0019)
Quadratic sum (electron)	$\pm$2.3% (0.0058)	$\pm$6.1% (0.013)	$\pm$0.61% (0.0019)	$\pm$6.2% (0.0136)

3.8 Results

Final results, including both statistical and systematic uncertainties, are shown in Table 3.8 and in Fig. 3.30-3.31.

The results are in agreement, within the sensitivity obtained by this sample, with both SM theoretical calculations [2] and the MC simulation.

Table 3.8: A summary of the fit results for positively charged and negatively charged muons and electrons respectively. [31, 32]

	Data Fit Result
$\mu : (f_L - f_R)^-$	0.240 ± 0.036 (stat.) ± 0.031 (syst.)
$\mu : f_0^-$	$0.183 \pm 0.087 \pm 0.123$
Correlation	0.395 (stat.)
χ^2/ndof (stat)	0.767
$\mu : (f_L - f_R)^+$	$0.310 \pm 0.036 \pm 0.017$
$\mu : f_0^+$	$0.171 \pm 0.085 \pm 0.099$
Correlation	-0.721 (stat.)
χ^2/ndof (stat)	0.967
$e : (f_L - f_R)^-$	0.187 ± 0.069 (stat.) ± 0.066 (syst.)
$e : f_0^-$	0.130 ± 0.200 ± 0.174
Correlation (stat)	-0.204 (stat.)
χ^2/ndof (stat)	0.872
$e : (f_L - f_R)^+$	0.277 ± 0.060 ± 0.050
$e : f_0^+$	0.24 ± 0.190 ± 0.090
Correlation (stat)	-0.295 (stat.)
χ^2/ndof (stat)	2.239

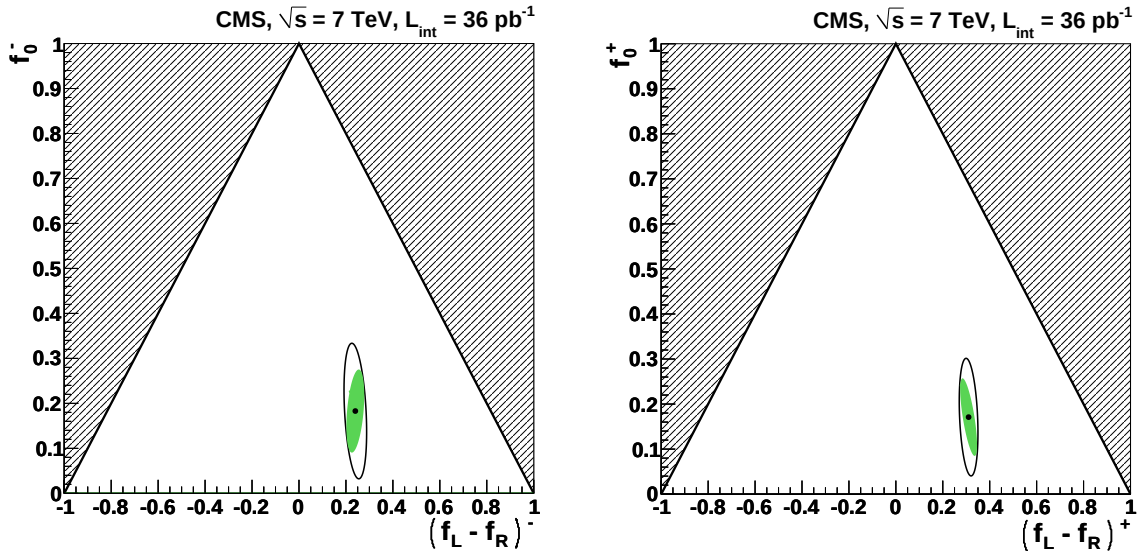

Figure 3.30: The muon fit result (black dot) in the $((f_L - f_R), f_0)$ plane. The 68% confidence level contours for the statistical and total uncertainties are shown by the green shaded region and the black contour respectively. The disallowed region is hatched. [31, 32]

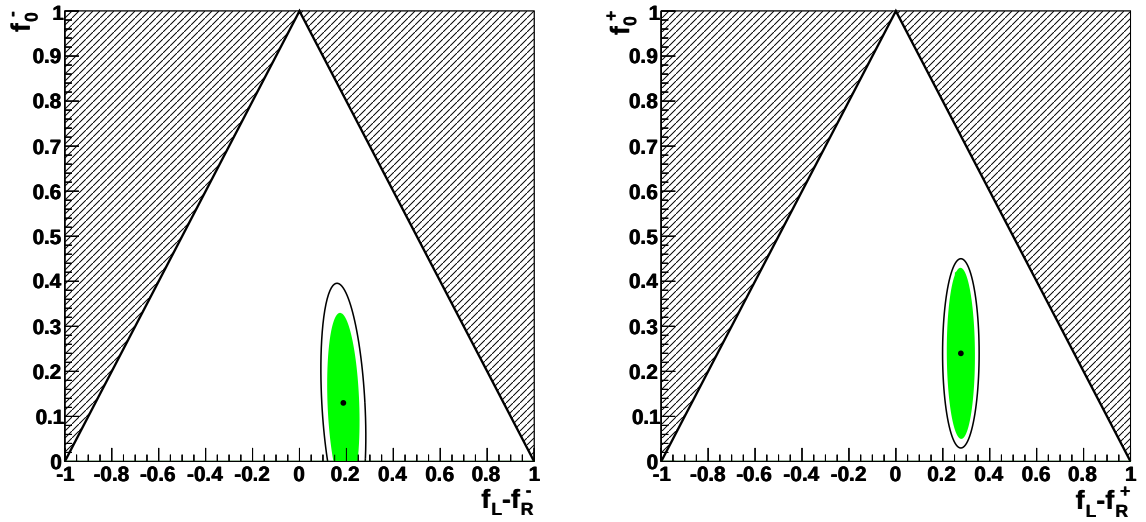

Figure 3.31: The electron fit result (black dot) in the $((f_L - f_R), f_0)$ plane. The 68% confidence level contours for the statistical and total uncertainties are shown by the green shaded region and the black contour respectively. The disallowed region is hatched. [31, 32]

Chapter 4

Measurement of Z polarization

The same technique used for W polarization measurement (described in the previous chapter) has been used on a sample of Z bosons produced in association with jets and decaying into two muons.

In this case it's possible to fully reconstruct the Z momentum in the laboratory frame, because all final state particles can be detected, and so there is no motivation to introduce the LP variable. Therefore, the variable chosen for fitting is $\cos\theta^*$ measured in the helicity frame.

Note that, also for the Z, the limited detector acceptance and resolution affect at reconstruction level the shapes of the angular distributions for bosons with definite polarization along their direction of flight.

This forces us to use once again templates instead of the analytical shapes. These templates are obtained in exactly the same way as already discussed for the W.

Moreover, the event selection will be simpler and will not involve complex objects like $\not{E}_T$. This avoids sources of important systematic uncertainties.

On the other hand, the cross section for production of Z bosons is lower (approximately by a factor 10) than for the W, and the weaker polarization analyzing power of Z leptonic decay does also affect the precision of the measurement.

In the following, the direction of the positive-charge muon has been chosen for the analysis (the direction of the μ^- is fully correlated with it, see Section 1.2.1).

4.1 Generator-level expectations

The same MC simulation (MADGRAPH+PYTHIA) has been used to produce 2.3 million Z/γ^*+Jets events at LHC conditions.

Generator-level polarization information is summarized in Table 4.1, in terms of (f_L, f_R, f_0) and the polarization fractions.

As discussed in Section 1.5.3, the angular distribution parameters f_i do not represent the boson polarization fractions V_i, because the Z also couples to the right-handed component of leptons. The polarization fractions are linear combination of the angular distribution parameters (Eq. 1.21).

Table 4.1: Angular parameters and polarization fractions of Z bosons with $p_T > 50$ GeV/c , at generator level.

$f_L - f_R$	0.033 ± 0.006
$f_0 = V_0$	0.217 ± 0.008
V_L	0.50 ± 0.02
V_R	0.28 ± 0.02

4.2 Event selection

A sample of muon-triggered events collected by CMS at $\sqrt{s}$ =7 TeV and corresponding to a nominal integrated luminosity of 642 pb^{-1} has been used for this analysis.

The following selection has been introduced to obtain a sample of Z bosons decaying into two muons:

- HLT_IsoMu17 isolated muon trigger requirement.
- Exactly two tight muons, with $p_T > 10$ GeV/c and $|\eta| < 2.1$.
- Leading muon $p_T > 20$ GeV/c .
- Invariant mass of the two muons in a 20 GeV - wide window centered on M_Z.
- No electron passing the LooseID 95% efficiency point with $p_T > 20$ GeV/c and $|\eta| < 2.5$.
- Less than four jets reconstructed by the Particle Flow algorithm (anti-k_T with $\Delta R = 0.5$ cone) with $p_T > 20$ GeV/c and $|\eta| < 5$.
- A ΔR between the muons and each jet of at least 0.5.
- A p_T(Z) > 50 GeV/c cut (where p_T(Z) means $|\vec{p}_T(\mu_1) + \vec{p}_T(\mu_2)|$).

The chosen trigger is isolated because non-isolated triggers (at the same p_T) were prescaled during the high-luminosity data taking used for this sample, and a higher offline muon p_T threshold would have reduced the statistics.

The mass window requirement and the tight muon isolation provide a highly pure sample of $Z \to \mu\mu$ events. The background from QCD is found to be negligible, while the $t\bar{t}$ contributes for less than 1%. [39]

4.3 Fit

4.3.1 Closure test

The template fit method efficiency has been verified fitting the reconstruction-level MC events with the templates (Fig. 4.1) generated from the same simulation.

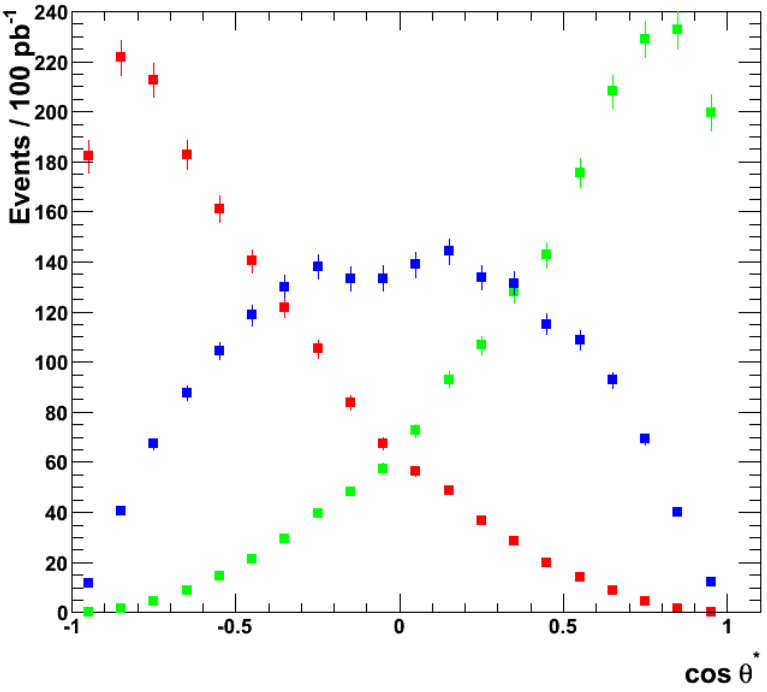

Figure 4.1: MC reconstruction level templates for left-handed (red), right-handed (green) and longitudinal (blue) polarization of the Z boson.

Results are reported in Table 4.2 and are consistent with values obtained at generator level (Table 4.1).

This test is important because of the fact that the MC simulation for the Z consists of a smaller number of events; this could, in principle, stress the mechanism used for template generation, that uses multiple fits to determine the polarization fraction bin by bin in Z (p_T, η).

Table 4.2: Angular distribution parameters of Z bosons with $p_T > 50$ GeV/c , at RECO-level in the MC simulation. The statistical uncertainties refer to the full statistics available in the simulation, corresponding to 1/fb at LO cross section.

$f_L - f_R$	0.034 ± 0.011
f_0	0.208 ± 0.017

4.3.2 Data

The $\cos\theta^*$ distribution in the helicity frame has been fitted with the same tools already used for the W analysis. The optimal fit range in this case is $(-0.8, 0.8)$.

Results are shown in Fig. 4.2 and in Table 4.3. The agreement with the MC is remarkable.

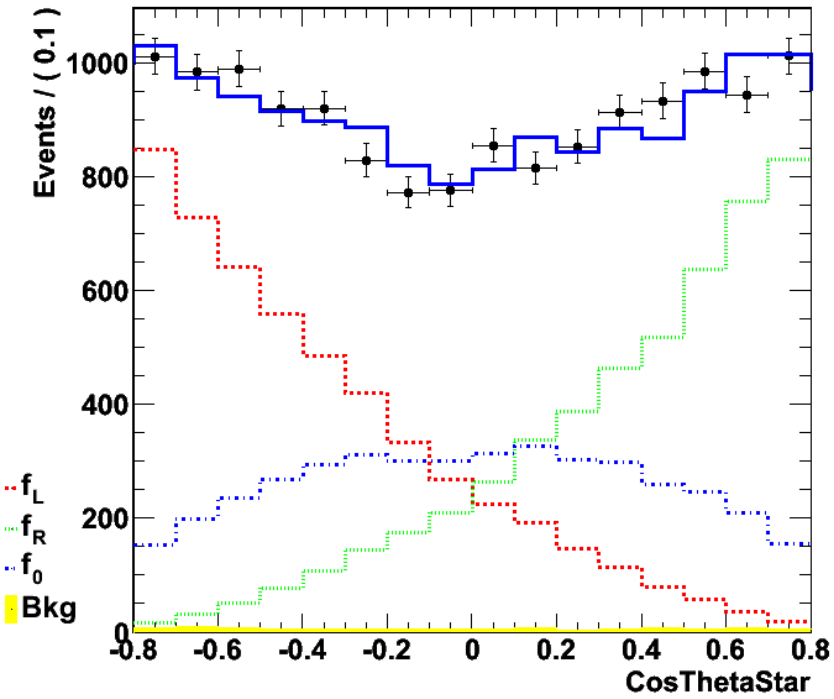

Figure 4.2: Fit with MC templates (in red, green and blue) to data (642 pb^{-1} integrated luminosity, in black). The blue line shows the fit result.

4.4 Systematic uncertainties

Systematic uncertainties due to MET scale and resolution, that are the dominant ones for the W, do not affect the Z polarization measurement.

Table 4.3: Angular distribution parameters of Z bosons with $p_T > 50$ GeV/c , in data. Uncertainties are statistical only, from the fit.

$f_L - f_R$	0.036 ± 0.012
f_0	0.229 ± 0.018

4.4.1 Muon p_T scale

The technique used to correct for muon p_T scale bias due to misalignment is the MuScleFit method, already presented in Section 2.2.4.

The latest reconstruction software features an improved description of alignment in the silicon tracker, that decreases significantly (by a factor ~ 2 for the ϕ dependence, and a factor ~ 5 for η, with respect to results from earlier datasets, like those used by the W analysis) the impact of corrections needed, and therefore also the systematic uncertainty (Table 4.4) introduced in the final results.

Table 4.4: The relative effects on the values of f_0 and $(f_L - f_R)$ from systematic uncertainties. The absolute values are shown in brackets.

	$f_L - f_R$	f_0
Mu pt scale correction	$\pm$ 4% (0.0014)	$\mp$ 0.6% (0.001)
$A_1 \pm (A_1 \times 10\%)$	$\mp$ 0.5% (0.0002)	$\mp$ 0.2% (0.0004)
$A_2 \pm (A_2 \times 10\%)$	$\mp$ 0.2% (0.0001)	$\mp$ 1.0% (0.002)
$A_3 \pm (A_3 \times 10\%)$	$\mp$ 1.0% (0.0003)	$\mp$ 0.1% (0.0001)
Background normalization	$\pm$ 1.6% (0.0006)	$\pm$ 0.4% (0.001)

4.4.2 Other sources

- The impact of implicit assumption of values for A_1, A_2, A_3 (defined in Section 1.3) has been studied repeating the fit after a 10% shift of their values, like for the W analysis. The corresponding changes in the final results are shown in Table 4.4.
- The background template normalization has been varied by a factor 2 to account for a potential background yield different from the simulated one. Results of the fit are reported in Table 4.4.
- Charge mis-identification of muons, the uncertainty introduced by the vertex multiplicity distribution correction and uncertainties on the PDF set used for the analysis have also been studied, and verified to have a negligible effect on the fit results.

4.5 Results

The final results of the Z polarization measurement are reported in Table 4.5. Statistical uncertainties dominate over systematic ones.

As expected from the mechanism of production for W and Z in pp collisions (Section 1.4), they exhibit similar polarization fractions (cfr. Table 3.1).

Table 4.5: Angular distribution parameters and polarization fractions of Z bosons with $p_T >$ 50 GeV/c , in data. Uncertainties are statistical+systematic.

$f_L - f_R$	0.036 ± 0.012
$f_0 = V_0$	0.229 ± 0.019
Correlation	-0.046
V_L	0.51 ± 0.04
V_R	0.26 ± 0.04

The fitted value is approximately 1 σ away from the value expected in the Standard Model. A plot of the 1-σ region of the $(f_L - f_R, f_0)$ plane extracted from the measurement is shown in Fig. 4.3.

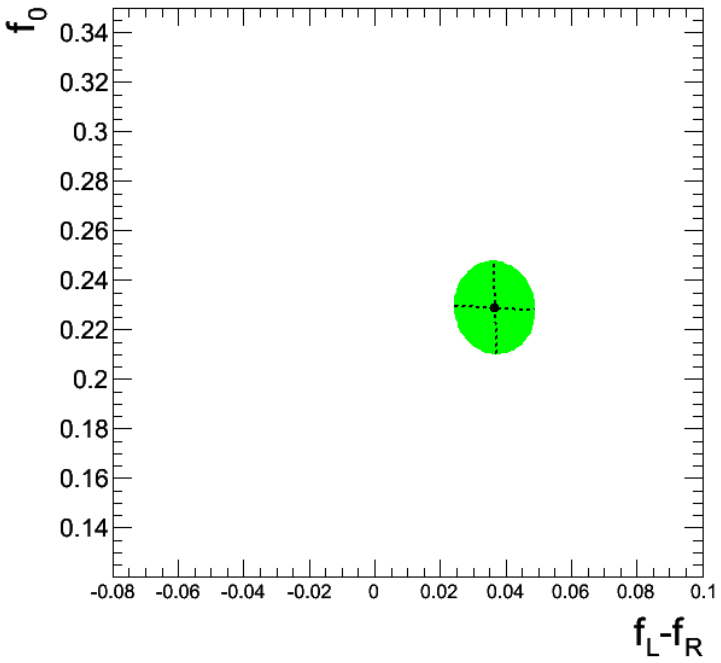

Figure 4.3: Result of the Z polarization measurement. The colored area represents the 1-σ contour region in the parameters space.

Conclusions

In this thesis, the first measurement of polarization that vector bosons produced in proton-proton collisions at the LHC exhibit at large transverse momenta has been presented.

After a discussion of relevant theoretical predictions and physics objects, the technique used for the analysis, based on fits to angular distributions of decay leptons in the helicity frame, has been reported in detail.

Results have been presented separately for W and Z bosons, and found to be consistent with Standard Model predictions.

Acknowledgements

I would like to thank the WPol group of the CMS Collaboration, that I have joined for the last year in preparation of this analysis: Oliver Buchmueller, Georgia Karapostoli, Jad Marrouche, Alex Sparrow, Paris Sphicas and Markus Stoye; the Scuola Normale Superiore di Pisa and the Istituto Nazionale di Fisica Nucleare (INFN), for their support; the Imperial College London for computing resources.

Bibliography

[1] R. Ellis, W. J. Stirling, B. R. Webber, *QCD and collider physics*, Cambridge University Press, 1996

[2] Z. Bern et al., *Left-handed W bosons at the LHC*, arXiv:1103.5445 [hep-ph], 2011

[3] C. F. Berger et al., *Precise predictions for W + 3 jet production at hadron colliders*, Phys. Rev. Lett. 102:222001, 2009

[4] C. F. Berger et al., *Next-to-Leading order QCD predictions for W+3-jet distributions at hadron colliders*, Phys. Rev. D 80:074036, 2009

[5] C. F. Berger et al., *Precise predictions for W + 4 jet production at the Large Hadron Collider*, Phys. Rev. Lett. 106:092001, 2011

[6] O. Buchmueller, G. Karapostoli, J. Marrouche, M. Peruzzi, A. Sparrow, P. Sphicas, M. Stoye, *Measuring the polarization of W bosons in W + jets events at the LHC using the CMS experiment*, CMS AN-2010/309, 2011

[7] J. C. Collins, D. E. Soper, *Angular distribution of dileptons in high-energy hadron collisions*, Phys. Rew. D 16, 2219, 1977

[8] E. Mirkes, *Angular decay distribution of leptons from W-bosons at NLO in hadronic collisions*, Nuclear Physics B, 387 (1), 1992

[9] C. F. Berger et al., *An automated implementation of on-Shell methods for one-loop amplitudes*, Phys. Rev. D, 78, 2008

[10] T. Gleisberg et al., *Event generation with SHERPA 1.1*, JHEP 0902:007, 2009

[11] C. F. Berger et al., *Next-to-Leading order QCD predictions for Z, gamma*+3-jet distributions at the Tevatron*, CERN-PH-TH/2010-029, 2010

[12] C. F. Berger et al., *Next-to-Leading order jet physics with BlackHat*, arXiv:0912.4927v2 [hep-ph], 2009

[13] The CMS Collaboration, *Measurement of the lepton charge asymmetry in inclusive W production in pp collisions at* $\sqrt{s} = 7$ *TeV*, CMS PAS EWK-10-006, 2011

[14] A. D. Martin, *Proton structure, Partons, QCD, DGLAP and beyond*, Acta Phys.Polon.B, 39, 2008

[15] K. Nakamura et al. (Particle Data Group), *Review of particle physics*, J. Phys. G 37, 075021, 2010.

[16] J. M. Cornwall, D. N. Levin, G. Tiktopoulos, *Derivation of gauge invariance from high-energy unitarity bounds on the S matrix*, Phys. Rev. D 10, 1145, 1974

[17] The CDF Collaboration, *Direct measurement of the W production charge asymmetry in $p\bar{p}$ collisions at $\sqrt{s} = 1.96$ TeV*, Phys. Rev. Lett. 102, 181801, 2009

[18] D. Acosta, M. Della Negra, L. Foà, A. Hervé, and A. Petrilli, *CMS physics: Technical Design Report vol. 1 : Detector performance and software*, CERN, 2006.

[19] A. de Roeck, A. Ball, M. Della Negra, L. Foà, and A. Petrilli, *CMS physics: Technical Design Report vol. 2 : Physics performance*, CERN, 2006.

[20] The CMS Collaboration, *Performance of muon reconstruction and identification in pp collisions at $\sqrt{s}$ = 7 TeV*, CMS PAS MUO-10-004, 2011

[21] The CMS Collaboration, *Commissioning of the Particle-Flow event reconstruction with the first LHC collisions recorded in the CMS detector*, CMS PAS PFT-10-001, 2010

[22] The CMS Collaboration, *Performance of muon identification in pp collisions at $\sqrt{s}$ = 7 TeV*, CMS PAS MUO-10-002, 2010

[23] *Proceedings of the first LHC Detector Alignment Workshop, CERN, Geneva, Switzerland, 4-6 September 2006*, CERN (series) 2007-004, 2007

[24] H. Enderle, *Search for momentum changing weak modes in the current tracker alignment*, http://www.desy.de/ enderle/, 2011

[25] The CMS Collaboration, *Electron reconstruction and identification at $\sqrt{s}$ = 7 TeV*, CMS PAS EGM-10-004, 2010

[26] The CMS Collaboration, *Missing transverse energy performance of the CMS detector*, CMS PAPER JME-10-009, 2011

[27] The CMS Collaboration, *CMS jet performance in pp collisions at $\sqrt{s}$ = 7 TeV*, CMS PAS JME-10-003, 2010

[28] The CMS Collaboration, *Jet calibration and resolution*, CMS PAS JME-10-011, 2010

[29] The CMS Collaboration, *Electromagnetic calorimeter commissioning and performance with 7 TeV data*, CMS PAS EGM-10-002, 2010

[30] The CMS Collaboration, *Identification and filtering of uncharacteristic noise in the CMS hadron calorimeter*, JINST 5 T03014, 2010

[31] The CMS Collaboration, *First measurement of the polarization of W bosons with a large transverse momentum in W+jets events at a pp collider*, CMS PAS EWK-10-014, 2011

[32] The CMS Collaboration, *Measurement of the polarization of W bosons with large transverse momenta in W+jets events at the LHC*, arXiv:1104.3829v1 [hep-ex], 2011

[33] J. Alwall et al., *MadGraph/MadEvent v4: the new web generation*, JHEP 09 028, 2007

[34] T. Sjöstrand et al., *PYTHIA 6.4 Physics and Manual*, JHEP 05 026, 2006

[35] M. R. Whalley et al., *The Les Houches accord PDFs (LHAPDF) and LHAGLUE*, arXiv:hep-ph/0508110, 2007

[36] S. Agostinelli et al., *G4 - a simulation toolkit*, Nucl. Inst. and Meth. A506 250, 2003

[37] *"The RooFit toolkit for data modeling"*, http://roofit.sourceforge.net

[38] The CMS Collaboration, *Jet energy corrections determination at 7 TeV*, CMS PAS JME-10-010, 2010

[39] The CMS Collaboration, *Measurements of inclusive W and Z cross sections in pp collisions at* $\sqrt{s}$ *= 7 TeV*, CMS PAS EWK-10-005, 2011